

UNIVERSITY OF THE WESTERN CAPE

MASTER THESIS

The Nature of the MicroJy Source Population

Author:

Emmanuel Francis Ocran

Supervisor:

Prof. Russ TAYLOR

Dr. Mattia VACCARI



UNIVERSITY of the
WESTERN CAPE

*A thesis submitted in fulfilment of the requirements
for the degree of Master of Science*

in the

Astronomy Research Group
Department of Physics

November 2015

Declaration of Authorship

I, Emmanuel Francis OCRAN, declare that this thesis titled, 'The Nature of the MicroJy Source Population' and the work presented in it are my own. I confirm that:

- This work was done wholly or mainly while in candidature for a research degree at this University.
- Where any part of this thesis has previously been submitted for a degree or any other qualification at this University or any other institution, this has been clearly stated.
- Where I have consulted the published work of others, this is always clearly attributed.
- Where I have quoted from the work of others, the source is always given. With the exception of such quotations, this thesis is entirely my own work.
- I have acknowledged all main sources of help.
- Where the thesis is based on work done by myself jointly with others, I have made clear exactly what was done by others and what I have contributed myself.

Signed:

Date:

“Thanks to my solid academic training, today I can write hundreds of words on virtually any topic without possessing a shred of information, which is how I got a good job in journalism.”

Dave Barry





UNIVERSITY OF THE WESTERN CAPE

Abstract

Faculty of Natural Sciences

Department of Physics

Master of Science

The Nature of the MicroJy Source Population

by Emmanuel Francis OCRAN

The study of the faint radio universe and of its properties has recently become a very active field of research not only because of the much improved capabilities of the SKA pathfinders but also because of the need to better plan for SKA surveys. These new facilities will map large areas of the sky to unprecedented depths and transform radio astronomy into the leading technique for investigating the complex processes which govern the formation and evolution of galaxies. This thesis combines multi-wavelength techniques, highly relevant to future deep radio surveys, to study the properties of faint radio sources.

The nature of the faint radio sources is presented, over a large GMRT survey area of an area of 1.2 deg^2 comprising 2800 sources. Utilising multi-wavelength data we have matched 85% of the radio population to Spitzer/IRAC and obtained a redshift estimate for 63%. The redshift associations are a combination of photometric and spectroscopic redshift estimates. This study investigates several multi-wavelength diagnostics used to identify AGN, using radio, infrared, optical and x-ray data. This analysis shows that various diagnostics (from the radio through the X-ray ones) select fairly different types of AGNs, with an evidence of a disagreement in the number of AGNs selected by each individual diagnostics.

For the sources with redshift we use a classification scheme based on radio luminosity, x-ray emission, BOSS/SDSS spectroscopy, IRAC colors satisfying the Donley criterion, and MIPS $24\mu\text{m}$ radio-loud AGN criteria to separate them into AGNs and SFGs. On the basis of this classification, we find that at least 12.5% of the sources with redshifts are AGNs while the remaining 87.5% are adopted as SFGs. We explore the nature of the classified sources through the far-infrared radio correlation. We measure a median q_{IR} value of 2.45 ± 0.01 for the SFGs and q_{IR} value of 2.27 ± 0.05 for the AGNs. The decrease in the median value of q_{IR} for the AGNs is a result of the additional AGN component to radio emission for the AGN-powered sources and find tentative evidence of an evolution of the q_{IR} with redshift.

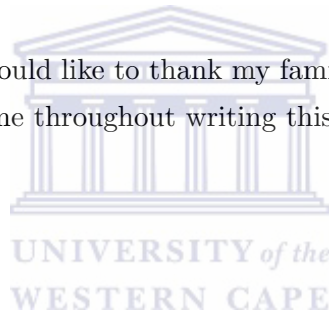
Acknowledgements

I would first like to thank my advisors, Prof. Russell Taylor and Dr. Mattia Vaccari, for being excellent instructors and a wonderful source of support over the years. They were always available to answer questions and offer advice, sometimes responding to emails at times when most people would be in their 3rd dream and far from being able to discuss and explain scientific matters effectively and intelligently.

I take this opportunity to record my sincere thanks to all faculty members of the Department of Physics, especially the Astronomy group for their help and encouragement.

The graduate students in this department deserve a huge thanks! There is a real community here that makes going through the trials and tribulations of a Masters program not only bearable, but fun. I have had such a great time my past 2 years here and I realize I am fortunate to have this experience. A huge thanks to all the friends I have made here along the way.

Last but not the least, I would like to thank my family: my mother and to my brothers and sister for supporting me throughout writing this thesis and my my life in general.



Contents

Declaration of Authorship	i
Abstract	iii
Acknowledgements	v
Contents	vi
List of Figures	ix
List of Tables	xiii
Abbreviations	xiv
Physical Constants	xv
Symbols	xvi
1 Introduction	1
1.1 Introduction	1
1.1.1 Active galactic nuclei (AGN)	1
1.1.2 Star forming galaxies	2
1.2 The star-formation AGN connection	3
1.2.1 Radio source number counts	5
1.3 Scope of Thesis	7
1.4 Thesis Outline	8
2 Source Catalog and Radio Observations	10
2.1 Introduction	10
2.2 Radio data at 610 MHz	11
2.3 The SERVS Data Fusion and the Ancillary Data	13
2.3.1 X-ray data	15
2.3.2 Optical data	16
2.4 Radio and multi-wavelength data cross-matching	17
2.4.1 Sources without SERVS 1 OR 2 catalog identifications	23



2.5	Redshifts of identified sources	24
2.5.1	Spectroscopic redshift	24
2.5.2	Photometric redshift	26
2.5.3	Comparison of spectroscopic and photometric redshift	27
2.5.4	Redshift distribution	32
2.6	Summary	33
3	AGN Diagnostic Techniques	35
3.1	Introduction	35
3.2	AGN selection	36
3.2.1	Radio selection of AGNs	36
3.2.2	X-ray selection of AGNs (X-ray Luminosities)	39
3.3	BOSS/SDSS classification	40
3.4	MIPS 24 micron flux	42
3.5	AGN classification	46
3.6	MIR color evolution of galaxies	47
3.7	Mid-Infrared diagnostics (IRAC colors)	49
3.7.1	Lacy Wedge	51
3.7.2	Stern Wedge	53
3.7.3	Donley Wedge (The Revised IRAC Selection Criteria)	54
3.7.4	Radio-quiet AGN selection	57
3.7.5	IRAC1234 & MIPS-24 detected sample	60
3.8	AGN optical line diagnostics	61
3.8.1	Four-line diagnostics	61
3.8.2	Comparison between the emission line diagnostic and other AGN diagnostics	69
3.8.3	Two-line diagnostics	72
3.9	Summary	80
4	Nature of the faint radio sources	81
4.1	AGN or SFG ?	81
4.1.1	Classification criteria and results	82
4.2	The far-infrared radio correlation	84
4.3	Luminosity dependence	90
4.3.1	Binning in radio luminosity	90
4.3.2	Binning in infrared luminosity	92
4.4	Summary	93
5	Summary and future work	95
A	Source Catalog and Radio Observations	98
B	AGN Diagnostic Techniques	100
B.0.1	Signal to noise cuts	101
C	Nature of the faint radio sources	105
C.0.2	Binning in radio luminosity	105

C.0.3 Binning in infrared luminosity 108

Bibliography **110**



UNIVERSITY *of the*
WESTERN CAPE

List of Figures

1.1	Optical U-R color vs. stellar mass for SDSS galaxies.	4
1.2	Total intensity differential source count at 612 MHz modified from Taylor <i>et al.</i> (2014)	6
2.1	The 1.2 deg ² of the GMRT ELAIS N1 mosaic at 612 MHz.	12
2.2	Histogram of $S_{\text{int}}/S_{\text{peak}}$ at the positions of sources in the mosaic image. .	13
2.3	The overlapping area between the GMRT 7 mosaic pointings on the SERVS ELAIS N1 image.	15
2.4	Histogram of the distribution of our X-ray Deep and X-ray Shallow data. .	16
2.5	Histogram of the positional errors (astrometric errors) of the GMRT sources	18
2.6	σ_{astro} [arcsec], the astrometric errors in the radio positions vs the flux density	19
2.7	GMRT ELAIS N1 mosaic at 610 MHz showing regions of the matched 85%	20
2.8	Positional Differences between the GMRT and multi-wavelength ancillary data (SERVS Data Fusion) from the cross correlation of the two catalogs. .	22
2.9	Classification of the unmatched radio sources to SERVS 1 OR 2 positions into their various categories.	23
2.10	Histogram of the distribution of spectroscopic redshift for objects with secure spectroscopic redshift detections.	25
2.11	Histogram of the distribution of photometric redshift for objects with secure photometric redshift detections.	27
2.12	Comparison between photometric and spectroscopic redshift for the GMRT sources with redshift detection.	28
2.13	Comparison of the photometric and spectroscopic redshifts for the GMRT radio sources which spectroscopy is available.	29
2.14	The $\Delta z = z_{\text{spec}} - z_{\text{phot}}$ as a function of $\log_{10}(1 + z_{\text{spec}})$ (left panel) and $\log_{10}(1 + z_{\text{phot}})$ (right panel) for objects with secure spectroscopic and photometric redshifts.	30
2.15	Same as Figure 2.13, where we have plotted only $\log_{10}(1 + z_{\text{phot}})$ is < 0.3 ,	31
2.16	Redshift distribution for the radio sources with an	33
3.1	The local luminosity function at 1.4 GHz derived separately for the radio- loud AGNs (circles) and SF galaxies (crosses	37
3.2	1.4 GHz luminosity versus redshift plot for the GMRT sample with red- shift detections.	38
3.3	X-ray luminosity as a function of redshift for the GMRT sources with X-ray detections.	40
3.4	The distribution of the MIPS 24 micron IDs with redshift detections for our GMRT sample	43

3.5	$q_{24\mu\text{m}}$, the logarithm of the ratio between the MIR and radio flux for the GMRT sources	44
3.6	$q_{24\mu\text{m}}$ vs $\log_{10}(1+z)$ for the GMRT sources with MIPS $24\mu\text{m}$ with redshift detections.	45
3.7	A schematic of AGN selection from the radio, x-ray, BOSS/SDSS spectroscopy and the MIPS 24 micron	46
3.8	Color evolution of Mid Infrared (MIR) bands. [5.8] – [8.0] (Vega) (top panel) and [3.6] – [4.5] (Vega)	49
3.9	RAC color-color plot using the main-field FLS data.	51
3.10	IRAC color-color diagram for our GMRT sample with four IRAC band detection in Lacy <i>et al.</i> (2004) color space.	52
3.11	IRAC colors of spectroscopically identified objects from the AGES survey.	53
3.12	Left panel: IRAC color-color diagram for our GMRT sample with four IRAC band detection in Stern <i>et al.</i> (2005) color space.	54
3.13	New AGN selection criteria (thick solid lines).	55
3.14	IRAC color-color diagram for our GMRT sample with four IRAC band detection in Donley <i>et al.</i> (2012) color space.	56
3.15	$q_{24\mu\text{m}}$ vs $\log_{10}(1+z)$ for the GMRT sources with MIPS $24\mu\text{m}$ with redshift detections.	58
3.16	Distribution of the $q_{24\mu\text{m}}$ parameter for RL AGN (1st panel), RQ AGN (2nd panel)	59
3.17	$q_{24\mu\text{m}}$ as a function of redshift for RL AGN (open red circles), RQ AGN (open red squares), and SFG (black stars)	60
3.18	Diagnostic diagram showing the galaxies in the sample studied by Kewley <i>et al.</i> (2001)	62
3.19	The BPT diagram, the dotted line represents the theoretical division between AGN and star-forming galaxies (SFGs) (Kewley <i>et al.</i> , 2001)	63
3.20	(a) The BPT [NII]/ $H\alpha$ versus [O III]/ $H\beta$ diagnostic diagram for SDSS galaxies with $S/N > 3$	64
3.21	BPT diagram (color coded according to their spectroscopic redshifts) - $\log_{10}([\text{NII}]/H\alpha)$ vs $\log_{10}([\text{OIII}]/H\beta)$	65
3.22	BPT diagram $\log([\text{N II}]/H\alpha)$ vs. $\log([\text{O III}]/H\beta)$ for the SDSS galaxies that have [O III], $H\beta$, [N II], and $H\alpha$ with $\text{SNR} > 5$	67
3.23	BPT diagram for the GMRT sources that have [OIII] , $H\beta$, [NII] , $H\alpha$ detections.	68
3.24	BPT diagram for the GMRT sources that have [OIII] , $H\beta$, [NII] , $H\alpha$ detections.	69
3.25	Histogram of the signal-to-noise ($\text{SNR}) = \text{EW}/\text{EW}_{\text{error}}$, the equivalent width of the spectral line divided by the error	71
3.26	BPT-NII diagram for GMRT sources with [OIII] , $H\beta$, [NII] , $H\alpha$ detections for an SNR cut of 3.	72
3.27	Illustration of the 2-line diagnostic which shows that galaxies with either a high [N II]/ $H\beta$ or a high ([O III]/ $H\alpha$)line ratio	73
3.28	EW of the [N II] emission line vs the ratio [N II]/ $H\alpha$ for galaxies in our GMRT sample with these line detections shown as grey white circles.	74
3.29	The ratio of [O III]/ $H\beta$ vs EW of the [O III] emission line for galaxies in our GMRT sample with these line detections shown as grey circles.	75

3.30	EW of the [N II] emission line vs the ratio [NII]/H α for galaxies in our GMRT sample with these line detections shown as grey circles.	76
3.31	Same as Figure 3.30 with an SNR cut of 3.	77
3.32	The ratio [O III]/H β vs EW of the [O III] emission line for galaxies in our GMRT sample with these line detections shown as grey circles.	78
3.33	Same as Figure 3.32. This plot indicates an SNR cut of 3.	79
4.1	A schematic of AGN selection combining the selection described in Figure 3.7 of Section 3.4 with the MIR selection satisfying Donley <i>et al.</i> (2012).	83
4.2	Histogram of the Integrated 8 - 1000 micron luminosity from MRR13 catalog for our GMRT sample.	86
4.3	Total IR luminosity (L_{IR}) as a function of redshift for GMRT sources.	87
4.4	Histogram of the 1.4 GHz radio luminosity for our GMRT sample.	88
4.5	$L_{1.4 \text{ GHz}}$ versus L_{\odot} for SFGs (top panel) and AGNs (bottom panel) according to the AGN selection described in Figure 4.1 of Section 4.1.1	89
4.6	Radio power vs redshift for all sources classified as AGNs and SFGs according to our combined multi-wavelength classification satisfying the Donley Wedge with respect to the MIR	91
4.7	Left panel: Infrared luminosity vs redshift for all sources classified as AGNs and SFGs according to our combined multi-wavelength classification satisfying the Donley Wedge with respect to the MIR.	93
A.1	Comparison between photometric and spectroscopic redshifts for the GMRT sources using the Rowan-Robinson <i>et al.</i> (2013) optical (top panel) and infrared (bottom panel)	99
B.1	BPT diagram for the GMRT sources that have [OIII] , H β , [OI] , H α detections. The Lacy wedge selected AGNs (open red circles) and SFGs (black stars) classification described in Section 3.7.1 are over-plotted on the BPT-O1.	100
B.2	BPT diagram for the GMRT sources that have [OIII] , H β , [SII] , H α detections. The Lacy wedge selected AGNs (open red circles) and SFGs (black stars) classification described in Section 3.7.1 are over-plotted on the BPT-SII.	101
B.3	BPT-NII diagram (GMRT sources with [OIII] , H β , [NII] , H α detections).	102
B.4	Same as Figure 3.28. The top left, top right and bottom plots indicates an SNR cut of 3, 5 and 10 respectively.	103
B.5	Same as Figure 3.29. The top left, top right and bottom plots indicates an SNR cut of 3, 5 and 10 respectively.	104
C.1	Considering all sources classified as AGNs and SFGs according to our combined multi-wavelength classification satisfying the Lacy Wedge with respect to the MIR.	106
C.2	Considering all sources classified as AGNs and SFGs according to our combined multi-wavelength classification satisfying the Stern Wedge with respect to the MIR.	107
C.3	Same as Figure 4.7. Considering all sources classified as AGNs and SFGs according to our combined multi-wavelength classification satisfying the Lacy Wedge with respect to the MIR	108

C.4 Same as Figure 4.7. Considering all sources classified as AGNs and SFGs according to our combined multi-wavelength classification satisfying the Stern Wedge with respect to the MIR. 109



List of Tables

2.1	GMRT cross-matching statistics. The table shows statistics from our new cross-matching.	21
2.2	Classification of the unmatched radio sources to SERVS 1 OR 2 positions into their various categories	24
3.1	Table showing the number of the CLASS and SUBCLASS for the BOSS spectroscopic classifications.	41
3.2	Table showing the breakdown of AGN selection from the radio, X-ray, BOSS/SDSS spectroscopy and the MIPS 24 micron flux density for the sources with redshift.	47
3.3	Table showing the various conversion we applied in converting to the Vega magnitude system. The zero point fluxes are in μJy	48
3.4	Total number of AGNs from various selection criteria according to the MIR classifications.	57
3.5	Table showing the breakdown of AGN selection from a subsample of IRAC1234 & MIPS-24 detected sample. Note that the fractions have been computed with respect to the redshift population of our sources. . .	61
3.6	BPT-NII comparison analyses results	70
3.7	Comparison of the Two-line diagnostics with previous results	77
4.1	Total number of AGNs and SFGs from a combination of the selection described in Figure 4.1 of Section 4.1.1 plus the various MIR classification criteria for sources with redshift.	84
4.2	q _{IR} trend in the different radio luminosity bins	92
4.3	q _{IR} trend in the different infrared luminosity bins	92

Abbreviations

AGN	A ctive G alactic N uclei
SFG	S tar F orming G alaxy
MIR	M id- I nfrared
FIR	F id- I nfrared
GMRT	G iant M etrowave R adio T elescope
SKA	S quare K ilometre A rray
ASKAP	A ustralian S quare K ilometre A rray P athfinder
IRAC	I nfrared A rray C amera
HST	H ubble S pace T elescope
ISO	I nfrared S pace O bservatory
ISOPHOT	I SO p hoto- p olarimeter
ISOCAM	I SO C amera
ELAIS	E uropean L arge A rea I SO S urvey
ACS	A dvanced C amera for S urveys
JVLA	J ansky V ery L arge A rray
LOFAR	L ow- F requency A rray for radio a stronomy
HERMES	H erschel M ulti-tiered E xtragalactic S urvey
MIPS	M ultiband I maging P hotometer
SWIRE	S IRTF W ide- A rea I nfrared E xtragalactic S urvey
SPIRE	S pectral and P hotometric I maging R eceiver
SERVS	S pitzer E xtragalactic R epresentative V olume S urvey

Physical Constants

Speed of Light $c = 2.997\,924\,58 \times 10^8 \text{ ms}^{-1}$ (exact)

Solar luminosity $L_{\odot} = 3.9 \times 10^{33} \text{ erg s}^{-1}$

Solar mass $M_{\odot} = 1.99 \times 10^{33} \text{ g}$

Solar temperature $T_{\odot} = 5.780 \times 10^3 \text{ K}$



Symbols

a	distance	m
P	power	W (Js^{-1})
ω	angular frequency	rads^{-1}



I dedicate this thesis to my family for nursing me with affections and love and their dedicated partnership for success in my life. . .



UNIVERSITY *of the*
WESTERN CAPE

Chapter 1

Introduction

1.1 Introduction

1.1.1 Active galactic nuclei (AGN)

Active Galactic Nucleus (AGN) corresponds to a class of highly luminous sources which emit from very compact regions in the centres of galaxies whose emission is powered by accretion onto a massive black hole. Depending on the characteristics of their observed spectra AGNs are divided into a number of sub-classes. However modern AGN unification schemes imply that at least some of these classes represent different orientations of an intrinsically similar set of objects (Kormendy and Ho, 2013). Understanding the role of AGNs in shaping the properties of their host galaxies is one of the critical areas in galaxies formation and evolution studies. Most galaxies contain a supermassive black hole (SMBH) in their centre (Richstone, 1998). This follows fundamental relations to their host galaxies (Ferrarese and Merritt (2000)). AGNs are known to be central unresolved point sources in galaxies emitting a non-stellar spectrum. AGNs emit radiation from a broad range of wavelengths, from radio to X-rays. Due to their brightness, they can be detected up to cosmological distances. For this reason, they offer the opportunity of studying the Universe up to ten billion years ago and of tracing their evolution across most of the Hubble time.

An active galactic nucleus (AGN) can be defined as a galaxy containing a massive ($> 10^5 M_{\odot}$) accreting black hole (BH) with Eddington ratio exceeding the (somewhat arbitrary) limit of $L_{\text{AGN}}/L_{\text{Edd}} = 10^{-5}$, where L_{AGN} is the bolometric luminosity and $L_{\text{Edd}} = 1.5 \times 10^{38} M_{\text{BH}}/M_{\odot} \text{ erg s}^{-1}$ is the Eddington luminosity for a solar composition gas Netzer (2015). From the observational point of view, AGNs are apparent stellar sources with non-thermal spectra and high bolometric luminosity ($\gtrsim 10^{42} \text{ erg s}^{-1}$) that in

some cases can exceed that of the host galaxy. These sources emit radiation from a broad range of wavelengths, i.e from radio through to X-rays. Due to their brightness, they can be detected up to cosmological distances and for this reason, they offer the opportunity of studying the Universe up to 10 billion years ago and tracing their evolution across most of the cosmic time.

AGNs display a variety of properties which explains the historical classification in several classes often without recognising the common physical origin. Different orientations with respect to the observer, explained many of the observed differences, thus leading to the so called AGNs Unification Scheme proposed by [Antonucci \(1993\)](#) and [Urry and Padovani \(1995\)](#).

AGNs can possess rich atomic emission and absorption lines spectra. Based on the differences in the near-infrared(NIR)-optical-ultraviolet (UV) regime, AGNs can be divided into two categories namely Type 1 and Type 2 AGNs. For Type 1 AGNs, the UV bump is clearly visible and some emission lines have a broad component. For Type 2 AGNs, the spectrum appears redder and these wavelengths are dominated by the host galaxy stellar light. Also the emission lines in Type 2 AGNs lack the broad component (see [Netzer \(2015\)](#)).

1.1.2 Star forming galaxies

The conversion of gas into stars is a fundamental characteristic of galaxies. Building an understanding of star formation processes involves several astrophysical areas. A star-forming galaxy is a galaxy with a high rated recent or ongoing formation of new stellar populations from the collapse of dense gas clouds. Since the most massive stars ($M > 8M_{\odot}$) of a stellar population are short lived, with typical lifetime of 3×10^7 years, they progressively disappear as the galaxy ages if they are not continuously replaced by new generations of stars. Star-forming galaxies represent a valuable tracer of cosmic history. The observation of massive stars is a direct evidence of recent activities of star formation in galaxies. [Condon \(1992b\)](#) reported that almost all the radio emission SFGs is synchrotron radiation from relativistic electrons and free-free emission from HII regions. Stars more massive than $M \sim 8M_{\odot}$ produce Type II and Type Ib supernovae whose remnants are thought to accelerate most of the relativistic electrons in SFGs (see [Condon \(1992b\)](#)).

Generally, SFGs are gas and dust rich, the materials from which stars form. Both the UV radiation and the line flux can be obscured to the observer. The appearance of a redder continuum with rest-frame optical colors similar to those of passive galaxies can be seen in the case of strong dust extinction.

SFGs have typically disk-like morphology, with rotationally supported stellar kinematics. At higher redshift (i.e. $z > 1$), the SFG disks are often characterized by a clumpy structure as, being richer in gas than in the local Universe. Gravitational instability naturally leads to large turbulence and giant star-forming clumps (see [Genzel *et al.* \(2011\)](#), and reference therein).

1.2 The star-formation AGN connection

Understanding the relationships between different classes of sources in the faint radio sky, and their cosmic evolution, is important for improving our understanding of the broad and complex relationships that exist between AGN and star-formation activity in the universe. Tight correlations found between black hole mass and both stellar bulge mass ([Kormendy *et al.* \(1998\)](#); [McLure and Dunlop \(2002\)](#)) and velocity dispersion ([Gebhardt *et al.* \(2000\)](#); [Tremaine *et al.* \(2002\)](#)) in galaxies in the local universe indicates that the formation and growth of galaxies may be closely linked to the growth of their central black holes.

Semi-analytic, hierarchical models of galaxy formation predict galaxies form in hot hydrostatic haloes where the radiative cooling time of the gas is much shorter than the age of the system. Therefore without further heating, cooling flows develop which channel gas to the centre of the galaxy triggering star formation and facilitating further accretion onto the supermassive black hole. In this scenario galaxies in the local universe should be more massive and have bluer colours and higher rates of star formation than is actually observed ([White and Frenk, 1991](#)). On the other hand, there are observational evidences of a coeval growth of the SMBH and their hosts. Amongst them is the tight correlation observed in the local Universe between the mass of the BH and the mass of its host galaxy bulge (see [Kormendy and Ho \(2013\)](#), for a review). Thus suggesting some mechanisms of AGN feedback that self-regulate the BH growth or influence the conversion of gas in stars, for example quenching or triggering the star formation.

Galaxy formation simulations also invoke AGN feedback (e.g [Springel *et al.* \(2005\)](#)). For example, the mass function (MF) of galaxies, i.e. the total number of galaxies with stellar mass in a certain mass bin as a function of mass, predicted by cosmological simulation shows an excess of galaxies at the high mass end compared to the observed distribution (e.g., [Ilbert *et al.* \(2010, 2013\)](#)). In the feedback scenario, the AGN may inject momentum and radiation in the inter-stellar medium (ISM) preventing the cold gas to further collapse and form stars therefore reconciling theoretical predictions and observations.

In addition, AGN feedback has been proposed to explain the observed strong bi-modality in the galaxy population optical colors ([Strateva *et al.* \(2001\)](#); [Hogg *et al.* \(2002\)](#);

Baldry *et al.* (2004); Oh (2010); Schawinski *et al.* (2014)). When optical colors are plotted against stellar masses as shown in Figure 1.1, galaxies divide in a so-called "red sequence" with passive and relatively more massive galaxies and a "blue cloud" populated by smaller galaxies with younger stellar population.

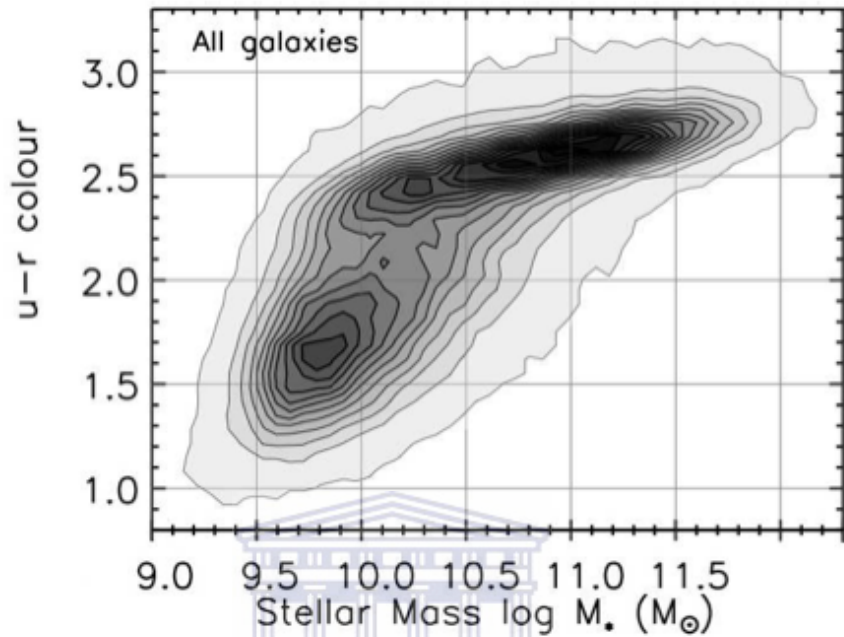


FIGURE 1.1: Optical U-R color vs. stellar mass for SDSS galaxies. A strong bimodality is observed with red massive galaxies forming the so-called "red sequence" in the upper part of the plot and less massive, bluer galaxies in the "blue cloud" on the bottom left. Adapted from Schawinski *et al.* (2010).

Last but not the least, the correlation of the AGN fraction with the IR luminosity, and consequently with the SFR, of its host, is another observational evidence supporting the idea of a connection between the AGN and SF activity. While AGNs are a small fraction of the overall galaxy population at $L_{\text{IR}} < 10^{11}$, they are more than 50% in ULIRG (e.g., Kartaltepe (2010)) suggesting that the AGN activity is linked to the strongest starburst events. A possible scenario explaining these observations has been proposed by Di Matteo *et al.* (2005) and Hopkins *et al.* (2008). Both the AGN and the intense SF are triggered by a gas rich major merger that provides fuel both to form new stars and to feed the black hole. In this phase, due to the large amount of dust present in the system, the AGN is often heavily obscured. The strong radiation from the AGN will then clean the surroundings, quenching on one hand the star formation and on the other hand removing the obscuration of the AGN itself.

The difference between star-forming galaxies (SFGs) and AGNs has become important in extragalactic astronomy. Over the years, extragalactic surveys has improved our understanding of these two processes particularly through a multi-wavelength approach.

Multi-wavelength surveys are fundamental in the study of AGNs and SFGs. AGNs and SFGs appear different depending on the wavelength range of consideration. Hard X-ray selection of AGN using deep observations is one reliable method of finding AGN (Mushotzky, 2004), although the most highly obscured objects remains undetected using this technique (Peterson, 2006). Thus it is important to characterise AGNs at different wavelength ranges, in order to be able to identify them by more than one selection technique.

1.2.1 Radio source number counts

The cumulative distribution of the number of sources (N) brighter than a given flux density limit has been used as a cosmological test. Considering a static and uniformly-filled (Euclidean) Universe, the flux (S) observed from a source (object) at distance R is:

$$S = \frac{L}{4\pi R^2} \quad (1.1)$$

where L is the luminosity. The length at which an object of luminosity L has a flux $> S$ is:

$$R(S) = (L/S)^{0.5} \quad (1.2)$$

The number of objects of luminosity L which a survey detects at flux density S from distance R to $R + dR$ is:

$$\begin{aligned} dN(L, S) &= \rho(L)dV(R), \\ &= \rho(L)4\pi R^2 dR, \\ &= -2\pi\rho(L)L^{\frac{3}{2}}S^{-\frac{5}{2}} dS \end{aligned}$$

where $\rho(L)$ is the number density of objects at distance R . This (the above equation) is the differential source counts for a given luminosity L . Thus in a flat universe with constant density of objects, the differential form in a flat universe with constant number density of objects is $dN/dS \propto S^{-5/2}$. Deviations from this form indicate evolution number density or luminosity with distance, but in practice cosmological signatures are hidden by source evolution. The radio source counts are derived from a radio survey and reflect the statistical properties of space and luminosity distribution of the radio source populations. The slope of the counts is determined essentially by the relative contribution of different types of sources at every flux, which is the result of their luminosity functions at various redshifts Prandoni *et al.* (2001).

Many studies observed a flattening in the source counts below 1 mJy (Windhorst (1984); Fomalont *et al.* (1984); Condon (1984)). This was interpreted as the signature of the

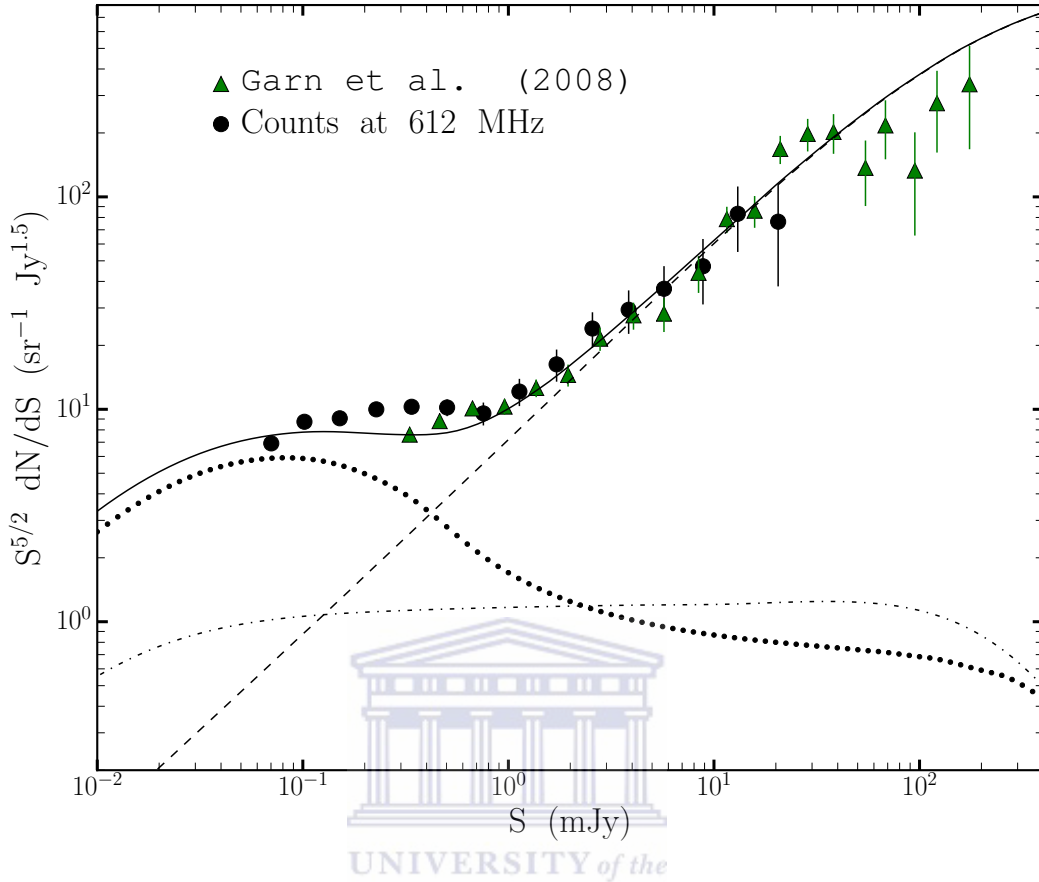


FIGURE 1.2: Total intensity differential source count at 612 MHz modified from [Taylor *et al.* \(2014\)](#). Solid black circles are counts from this work to a flux density limit of $70 \mu\text{Jy}$. Triangles show counts from [Garn and Alexander \(2008\)](#). Curves are model source counts from [Massardi *et al.* \(2010\)](#) whereby AGNs are shown as dashed curve, dotted curve represents starburst galaxies and dot-dashed curve represents normal galaxies. The solid line is the total counts from all three populations.

rise of another radio population: star forming galaxies (SFGs). However, determining the relative contribution of radio AGNs and SFGs in the sub-mJy regime remain an open issue that has not been solved. To tackle this problem, a very good understanding of the multi-wavelength properties of both SFGs and AGNs are required as well as deep radio observations.

[Taylor *et al.* \(2014\)](#) showed the differential source counts derived from the GMRT at 612 MHz in Figure 1.2. There is a flattening in the shape of the counts at about 1 mJy and continue approximately flat down to the detection limit. Simulated counts by [Massardi *et al.* \(2010\)](#) are also shown in Figure 1.2. This model includes two flat-spectrum populations with different evolutionary properties flat spectrum radio quasars (FSRQs), BL Lacertae (BL Lacs) and a single steep-spectrum population. For each population, we adopt a simple power-law spectrum, $S \propto \nu^{-\alpha}$, with $\alpha_{\text{FSRQ}} = \alpha_{\text{BLLac}} = 0.1$, and

$\alpha_{\text{steep}} = 0.8$ (see [Massardi *et al.* \(2010\)](#)). From this, it is evident that below about $450 \mu\text{Jy}$, the population is expected to be dominated by star forming galaxies. A smaller fraction of more nearby "normal" galaxies is expected to dominate over AGN at around this level.

While the bright radio sky is dominated by the emission driven by "radio-loud" AGNs, at fainter flux densities ($<1 \text{ mJy}$) the contribution from star forming galaxies (SFGs) become increasingly important (e.g., [Prandoni *et al.* \(2001\)](#); [Seymour *et al.* \(2008b\)](#); [Padovani *et al.* \(2009\)](#)). Recent work have revealed the presence of a third population of sources in the faint radio sky, the "radio-quiet" AGNs ([Smolčić \(2009\)](#)) and these sources show the presence of AGN activity in one or more bands of the electromagnetic spectrum (e.g optical, mid-infrared, X-ray) but the origin of their radio emission has been a matter of debate. [Giroletti and Panessa \(2009\)](#) proposed that they represent scaled versions of RL AGNs with mini radio jets whilst [Kimball *et al.* \(2011\)](#) proposed that their radio emission comes from star formation in the host galaxy.

1.3 Scope of Thesis

As deep radio surveys probe both AGN and SFGs, and are becoming more and more sensitive to the distant Universe, they represent a potentially very useful tool to address the role of AGNs in galaxy evolution. Several open issues remain however to be understood. Are we probing a regime where AGNs are less important? Can we learn anything about the relationship between AGNs and SFGs by studying faint radio sources? The first step must be to determine the nature of the faint radio population. Multi-wavelength studies of the radio population in recent years have already made progress in addressing long-standing research questions such as the nature of the faint radio source population and how the number counts of deep radio surveys of the extragalactic sky change as a function of flux. Do we continue to see AGN dominated radio emission?

In this work, we investigate the multi-wavelength properties of our radio sources drawn from the GMRT covering an area of 1.2 deg^2 of European Large Area ISO Survey (ELAIS) field N1 (EN1). EN1 is one of the 5 fields observed by Infrared Space Observatory (ISO) as part of the 11 square degree ISO ELAIS survey ([Lonsdale, 2005](#)). The ELAIS region contains a deep Hubble Space Telescope (HST) - Advanced Camera for Surveys (ACS) pointing. EN1 resulted in the delivery of the largest catalog on any survey on ISO [Rowan-Robinson *et al.* \(2004\)](#) from both ISOCAM instrument ([Cesarsky *et al.*, 1996](#)) and the ISOPHOT instrument ([Lemke, 1996](#)). It also contains a deep pointing of some 50 square arc minutes with the Infrared Array Camera (IRAC) and Multi-band Imaging Photometer for Spitzer (MIPS), taken as part of the extragalactic

FIRST Look Survey program (Surace *et al.*, 2005). EN1 field contains very low amounts of Galactic emission (Lonsdale *et al.*, 2003) and is ideal for observing the Extragalactic Universe because of its low level diffuse foreground (Baran *et al.*, 2010). Manners *et al.* (2003) reported Chandra observations of the central region of N1 whereas a 20 cm radio survey was carried out in this area by Ciliegi *et al.* (1999). Gonzalez-Solares *et al.* (2004) described optical associations of ELAIS sources using INT WFS survey. Also, spectroscopic follow-up have been done by Perez-Fournon *et al.* (2004) and Serjeant *et al.* (2004).

The deepest ever images of radio sources at 610 MHz have been obtained with GMRT of the EN1. At sensitivities in the μJy regime, these observations explore the radio source population at flux densities well below the regime dominated by classical radio galaxies and AGN. We aim to know whether the emission at radio is dominated by an active nucleus or by emission from the disk of the galaxy, powered by energy injection from stars. We assume a flat cold dark matter (ΛCDM) cosmology with $\Omega_\Lambda = 0.7$, $\Omega_m = 0.3$ and $H_0 = 70 \text{ kms}^{-1} \text{ Mpc}^{-1}$.

1.4 Thesis Outline

This thesis starts an exploration of the faint radio sources using the multi-wavelength information to categorize the faint sources as AGN or SFG dominated. Below is an overview of the content of the next Chapters of this Thesis.

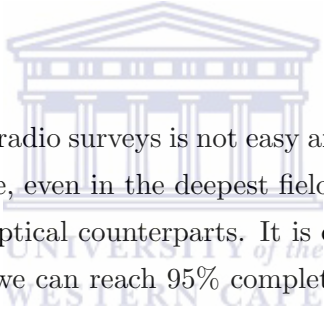
- **Chapter 2** This Chapter presents the radio and the multi-wavelength source catalog used in this Thesis. The Giant Metrewave Radio Telescope (GMRT) observations of the ELAIS N1 are described, and particular attention is dedicated to the compilation of multi-wavelength catalog from the cross-match. The radio data comprises 2800 sources down to a root mean square sensitivity of $10\mu\text{Jy}$ and therefore represents one of the deepest radio samples. Thus, these observations explore the radio source population well below the regime dominated by classical radio galaxies and Active Galactic Nuclei. A multi-wavelength approach is fundamental when dealing with deep radio images as most of the sources are unresolved and little information can be extracted from a single frequency catalog. Therefore, at the beginning of this Chapter, the wealth of multi-wavelength data available in the EN1 field, from the X-ray through to the Mid Infrared is described. Details of how the positions of the radio sources is cross-correlated with the multi-wavelength source catalogs in the same region from the Infrared, Optical and X-ray data sets, and with new optical spectroscopic observations is described.

- **Chapter 3** In this Chapter, we study various diagnostics used to separate SFGs and AGNs. First we classify a source as an AGN, if there is an indication of an AGN activity in the radio, x-ray, BOSS/SDSS optical spectroscopy and MIPS 24 micron flux (used by [Bonzini *et al.* \(2013\)](#) and combine these four selections to separate the radio sources between SFGs, radio-quiet and radio-loud AGNs). We show how these four selected AGN criteria behave using the $[5.8] - [8.0]$ (Vega) and $[3.6] - [4.5]$ (Vega) MIR color evolution of galaxies with redshift. Then we compare these four criteria to the various MIR color-color diagnostics using the Lacy, Stern and Donley wedges. We report the discrepancies between our initially selected AGNs and the MIR colors particularly, with the Lacy and Stern wedges. In the latter sections of this Chapter, we present four-line and two-line emission diagnostics. We study the BPT-NII diagnostics and also employ SNR cuts in order to compare these emission line diagnostics to other AGN diagnostics previously presented in the Chapter. Thus, we study all these different AGN diagnostics in order to disentangle the differences between the various AGN selection techniques and to further build up a secure AGN classification scheme which we use as a segue in the analyses of [Chapter 4](#)
- **Chapter 4** The main topic of this Chapter is the classification of the 63% for the sources with redshift as AGNs or SFGs. The various methods studied in [Chapter 3](#) to disentangle the different classes of sources that populate the faint radio sky is summarized in this Chapter. In more details, we classify a source as SFGs or AGN by combining radio, MIR, Optical and X-ray data. Using these data we separate the 63% of the GMRT sources with redshift into SFGs and AGNs. We then study the nature and properties of the SFGs and AGNs with the far-infrared radio correlation. We study evolutionary trends within the far-infrared radio correlation for both SFGs and AGNs with redshift, radio and infrared luminosities.
- **Chapter 5** In this last Chapter a summary and conclusions of the main results is presented. Further developments of this Thesis is proposed.

Chapter 2

Source Catalog and Radio Observations

2.1 Introduction



Classifying sources of deep radio surveys is not easy and hence requires multi-wavelength data. Optical surveys alone, even in the deepest fields, allow us to identify only $\sim 70\%$ of the radio sources with optical counterparts. It is only by combining the information from all wavelengths that we can reach 95% completeness. Combining the information obtained at different wavelengths, allows us to classify sources as star forming galaxies (SFGs), radio-loud AGN (RL AGN) and radio-quiet AGN (RQ AGN). We can further study the properties and the evolution at these different classes separately.

This Chapter focuses on the identification of the multi-wavelength counterparts of the GMRT radio sources through cross-matching. Our main goal is to assign a redshift to the radio sources. This information will be then used in the subsequent Chapters to classify the sources and study their evolutionary properties.

Data from several optical through far-infrared surveys were combined into a SERVS Data Fusion catalog, using a matching radius of $1.0''$ to match them to the SERVS dual-band catalog. Details of this catalog will be presented in Vaccari et al. (In prep). This catalog contained objects covering the full $\sim 9.5\text{deg}^2$ of the ELAIS N1 area. This Data Fusion catalog was then matched to the 2800 610 MHz detections in the GMRT catalog. The GMRT sources were matched to the SERVS Fusion catalog using a variable selection radius, which resulted in a 85% match rate. We then studied the remaining 15% unmatched objects by analysing the SERVS data manually, and categorizing these

unmatched radio sources depending on the SERVS image. We then discuss the redshift distribution (spectroscopic and photometric) of our sample.

2.2 Radio data at 610 MHz

GMRT observations of the ELAIS N1 were obtained during several sessions from 2011 to 2013. Observations were carried out for 7 positions arranged in a hexagonal pattern centred on $\alpha = 16^{\text{h}} 10^{\text{m}} 30^{\text{s}}$, $\delta = 54^{\circ} 35' 00''$, covering an area of 1.2 deg^2 . Each position was observed for ~ 30 hours in three 10-hour sessions. The total bandwidth was 32 MHz, split into 256 spectral channels in four polarization states, centred at 612 MHz. Observations 3C286 twice in each observing session was used to calibrate the flux scale, bandpass and absolute position angle. Time dependent gains and on-axis polarisation leakage corrections were measured by frequent observations of J1549+506. Because the phase calibrator is a flat spectrum and compact source, it could vary significantly over a monitoring period (Koopmans *et al.*, 2000). Figure 2.1 presents the central 1.2 deg^2 of the GMRT mosaic at 610 MHz. The root mean square (rms) noise in this mosaic is $10.3 \mu\text{Jy}/\text{beam}$ before primary beam correction. The angular resolution of the radio image is $6.1'' \times 5.1''$. The fluxes of the radio source catalogue was extracted using the AIPS SAD program and comprises of 2800 radio sources. The majority of the sources form a dense "background" of compact sources scattered throughout the image that are largely unresolved at $6.1''$ resolution and the image shows a handful of classical bright double-lobed radio galaxies (Taylor *et al.*, 2014). The synchrotron emission is assumed to follow a power-law as shown in equation Equation 2.1 below:

$$S_{\nu} = S_0 \nu^{\alpha} \quad (2.1)$$

If

$$S \propto \nu^{\alpha} \Rightarrow \frac{S_1}{S_2} = \frac{\nu_1^{\alpha}}{\nu_2^{\alpha}} \quad (2.2)$$

then,

$$S_{1.4\text{GHz}} = \left(\frac{1.4}{0.6} \right)^{\alpha} S_{0.6\text{GHz}} \quad (2.3)$$

In the absence of a measured spectral index, we assumed a spectral index of $\alpha = -0.7$ (Ibar *et al.*, 2010). Since $\alpha = -0.7$ is the spectral index based on an average steep-spectrum radio source (Condon 1992)(Condon, 1992a)

In order to most accurately reflect the true flux density of a source we adopted the integrated flux density. For unresolved sources the peak flux equals the integrated flux. In calculating the integrated flux, it is important to know the beam size and also integrate

the flux over the observed size of the source. Hence, the integrated flux is more uncertain (larger errors) since summing over many pixels adds to the noise. But using the peak flux density for resolved sources results in underestimating their flux density and all derived quantities. We used the peak flux of the radio sources that we have in our catalog since the resolution of our sources is not certain. We plot a histogram of $S_{\text{int}}/S_{\text{peak}}$ in Figure 2.2, which is based on the positions of actual sources in our mosaic image. In Figure 2.2, the mean ratio of S_{int} to S_{peak} being 1.581 and the peak in the histogram is around $S_{\text{int}}/S_{\text{peak}} \approx 1.12$.

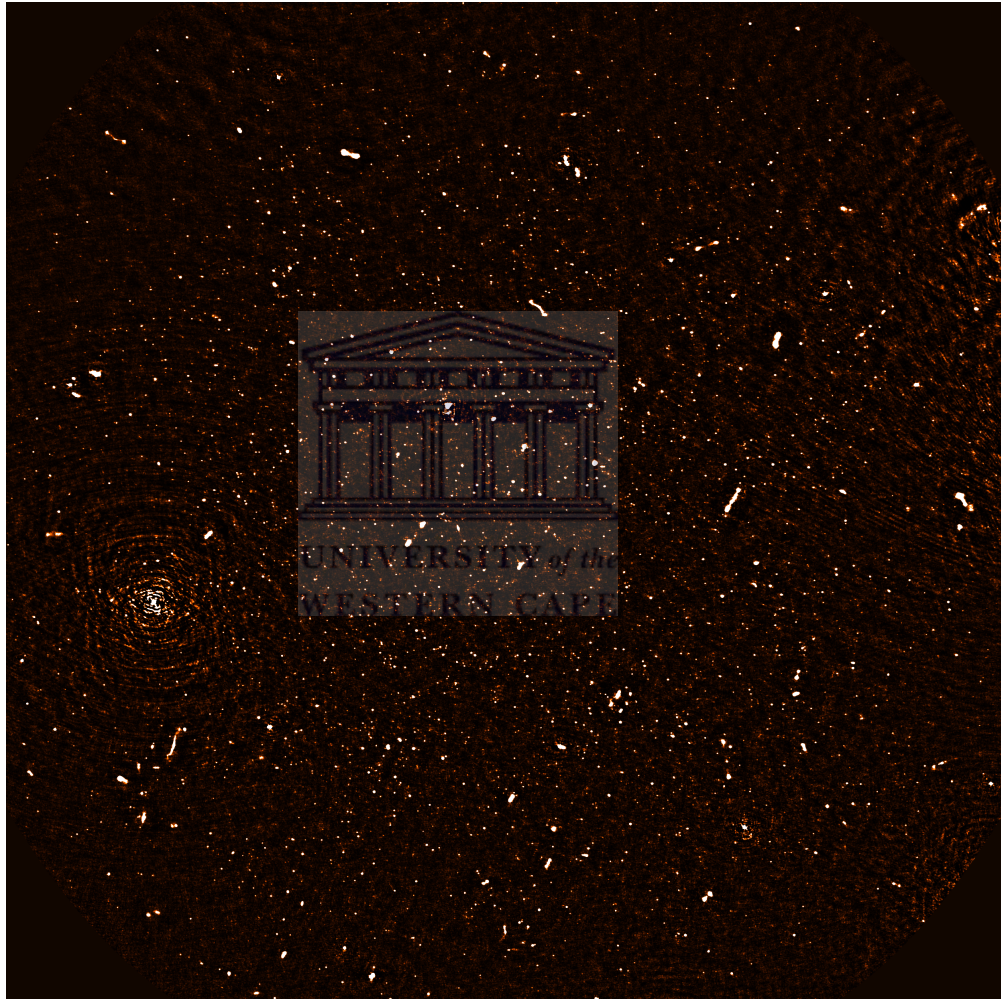


FIGURE 2.1: The 1.2 deg^2 of the GMRT ELAIS N1 mosaic at 612 MHz.

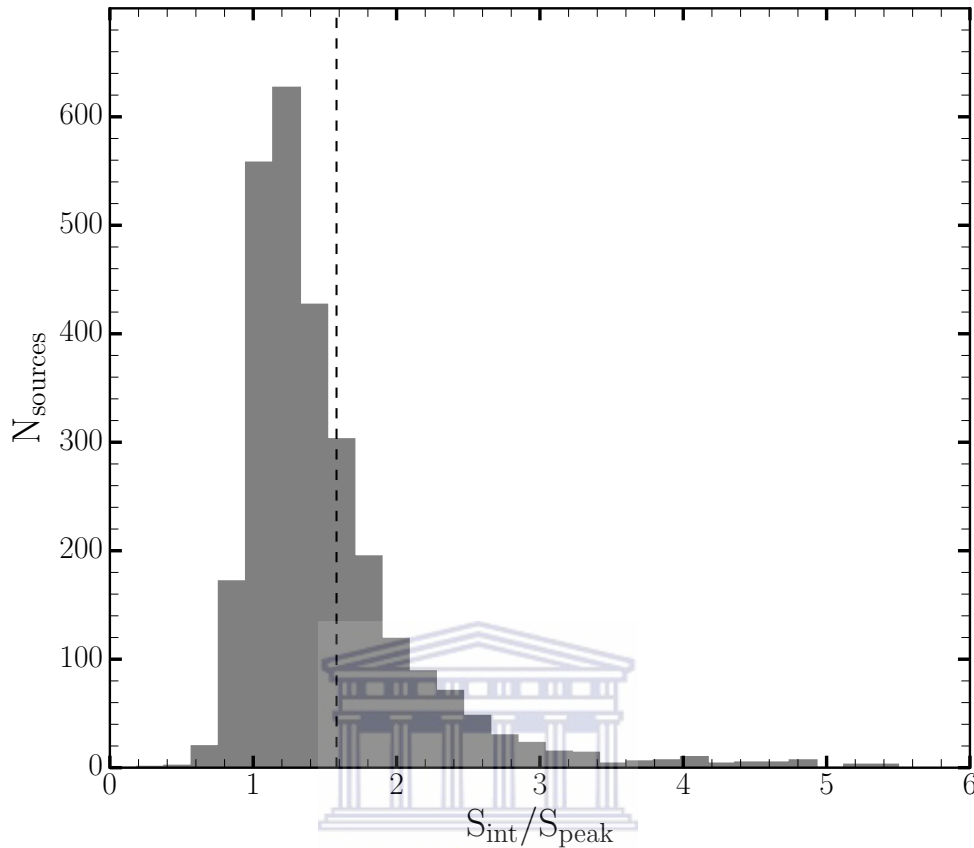


FIGURE 2.2: Histogram of $S_{\text{int}}/S_{\text{peak}}$ at the positions of sources in the mosaic image. The ratio $S_{\text{int}}/S_{\text{peak}}$ is greater than 1. The dashed vertical line marks the average, $S_{\text{int}}/S_{\text{peak}} = 1.581$. By design of the survey, most sources lie reasonably close to a pointing center and thus the histogram peaks at a value of $S_{\text{int}}/S_{\text{peak}} \sim 1.12$.

2.3 The SERVS Data Fusion and the Ancillary Data

The EN1 is one of the most studied patches of the sky and has been observed in many wavebands. As we will discuss in the following sections, this wealth of data is crucial to select the correct counterpart of a radio source. Here we describe the large amount of optical, IR and X-ray data used in this work.

The Spitzer Extragalactic Representative Volume Survey (SERVS; [Mauduit *et al.* \(2012\)](#)) is a warm Spitzer survey which imaged 18 deg^2 using the 3.6 and 4.5 μm IRAC bands down to an rms noise of $0.4 \mu\text{Jy}$. The design was to enable the study of galaxy evolution as a function of environment from $z \sim 5$ to the present day and is the first extragalactic survey that is both large enough and deep enough to put rare objects such as luminous quasars and galaxy clusters at $z \geq 1$ into their cosmological context. SERVS also overlaps with several key surveys at optical, near through far-infrared, submillimeter, and

radio wavelengths to provide an unprecedented view of the formation and evolution of massive galaxies.

The SERVS Data Fusion is a multi-wavelength infrared-selected catalogue compiled by Vaccari et al. (in preparation, www.mattiaivaccari.net/df). The Data Fusion contains most of the multi-wavelength public photometry and spectroscopy for SERVS sources within the EN1 and other SERVS fields.

For inclusion in the SERVS Data Fusion, a source must be detected at either band in the SERVS images, and ancillary datasets are matched against the SERVS position using a search radius of 1 arcsecond. This SERVS-IRAC12 "Bandmerge" is then used as input for the SERVS "Data Fusion" (i.e. a SERVS-IRAC12 - selected catalog of multi-wavelength measurements currently available from the UV to the FIR). The SERVS IRAC12 was produced using single-band IRAC1 and IRAC2 catalogs, measured aperture and integrated fluxes/magnitudes and corrected aperture fluxes/magnitudes using the correction factors adopted by SWIRE DR2/3 by (Surace et al., 2005). In the ELAIS N1, the SERVS Data Fusion includes optical photometry by González-Solares et al. (2011) (GS11), near-infrared photometry from the United Kingdom Infrared Telescope (UKIRT) Infrared Deep Sky Survey (UKIDSS; see Lawrence et al. (2007)) and mid-infrared and far-infrared photometry from the Spitzer Wide-Area Infrared Extragalactic survey (SWIRE; see Lonsdale et al. (2003)).

The Spitzer Wide-area InfraRed Extragalactic (SWIRE), is a wide-area imaging survey which traced the evolution of dusty, star-forming galaxies, evolved stellar populations, and active galactic nuclei (AGNs) as a function of environment, from redshifts $z \sim 3$ to the current epoch. The survey aimed to determine the evolution of the spatial distribution and clustering of evolved galaxies, starbursts, and AGNs in the key redshift range $0.5 < z < 3$ over which much of cosmic evolution has occurred and to determine the evolutionary relationship between "normal galaxies" and AGNs and the contribution of AGN accretion energy versus stellar nucleosynthesis to the cosmic backgrounds. SWIRE (Lonsdale et al., 2003) covered nearly 50deg^2 in six different fields, one of which is the EN1. These fields have been surveyed by the Spitzer Space Telescope using both the Infrared Array Camera (IRAC) and the Multi-Band Imaging Photometer (MIPS) far-infrared camera. The Data Fusion catalogue contains data from IRAC, which made observations at 3.6, 4.5, 5.8 and $8.0\ \mu\text{m}$ with 5σ sensitivities of 3.7, 5.4, 48 and $37.8\ \mu\text{Jy}$ respectively and the MIPS 24, 70 and $160\ \mu\text{m}$ bands.

Figure 2.3 presents the overlapping area between the GMRT 7 mosaic pointings on the SERVS ELAIS N1 image. We can see that GMRT covers much of the SERVS area. The circles are centred on the 7 pointing directions with the GMRT that are combined to

make the GMRT mosaic image. The size of the circles corresponds to the area within the region where the response function of the GMRT is greater than half the maximum.

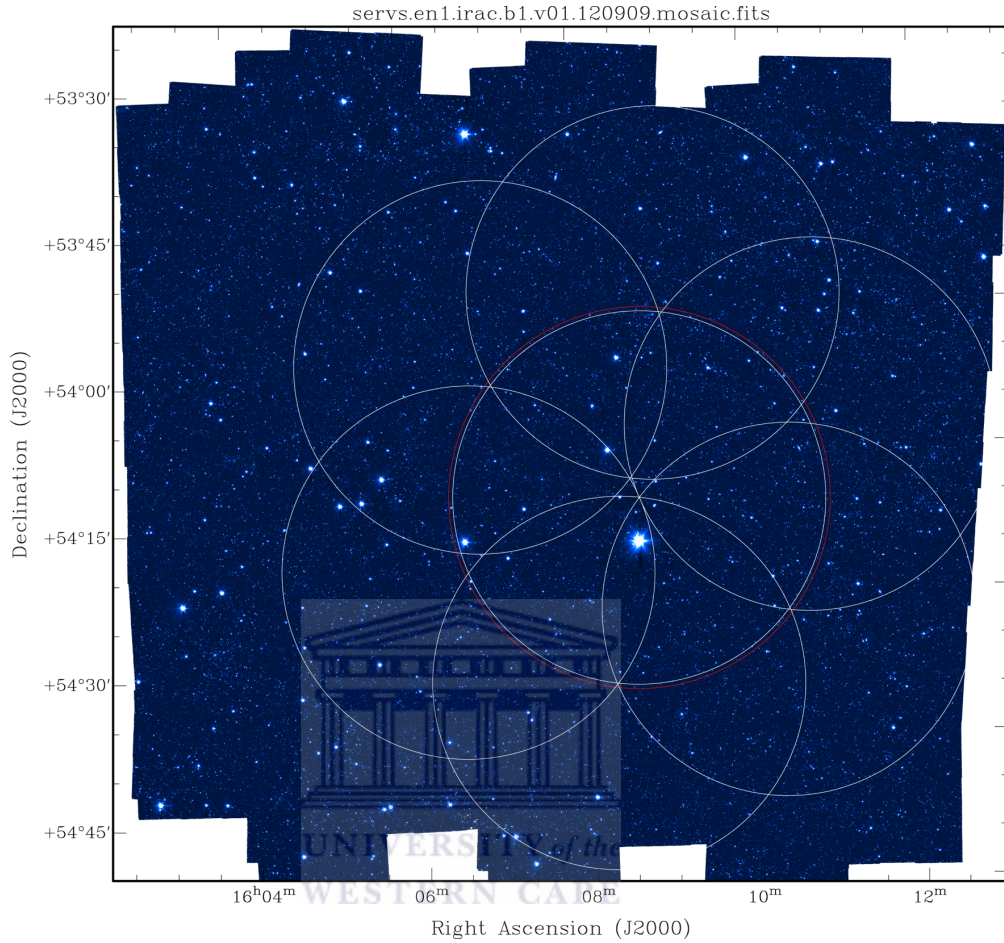


FIGURE 2.3: The overlapping area between the GMRT 7 mosaic pointings on the SERVS ELAIS N1 image. Note that GMRT covers much of the SERVS area. The circles are centred on the 7 pointing directions with the GMRT that are combined to make the GMRT mosaic image. The size of the circles is the half-power circle of the GMRT primary beam.

2.3.1 X-ray data

The only astrophysical sources that can reach very high X-ray luminosity are AGNs. Usually a cut in the unabsorbed X-ray luminosity at 10^{42} erg s^{-1} is considered as a threshold dividing AGNs and SFGs (see Szokoly *et al.* (2004)). Optically thick dust present along the line of sight, progressively suppresses the soft (0.5 - 2 keV) X-ray emission thereby increasing obscuration and the X-ray spectrum becomes harder. The major problem of selecting AGNs in the X-ray is that to reach sensitivity necessary to detect moderately luminous AGNs at high redshift ($z \approx 2.0$), very long observing time is needed.

The x-ray data we used is drawn from the Chandra Point-Source Catalogs produced by

Trichas *et al.* (2012) using the Imperial College London pipeline (maps in Georgakakis *et al.* (2008) & catalogs in (Laird *et al.*, 2009)). The data also include Chandra deep observations of EN1 (Manners *et al.*, 2003) .

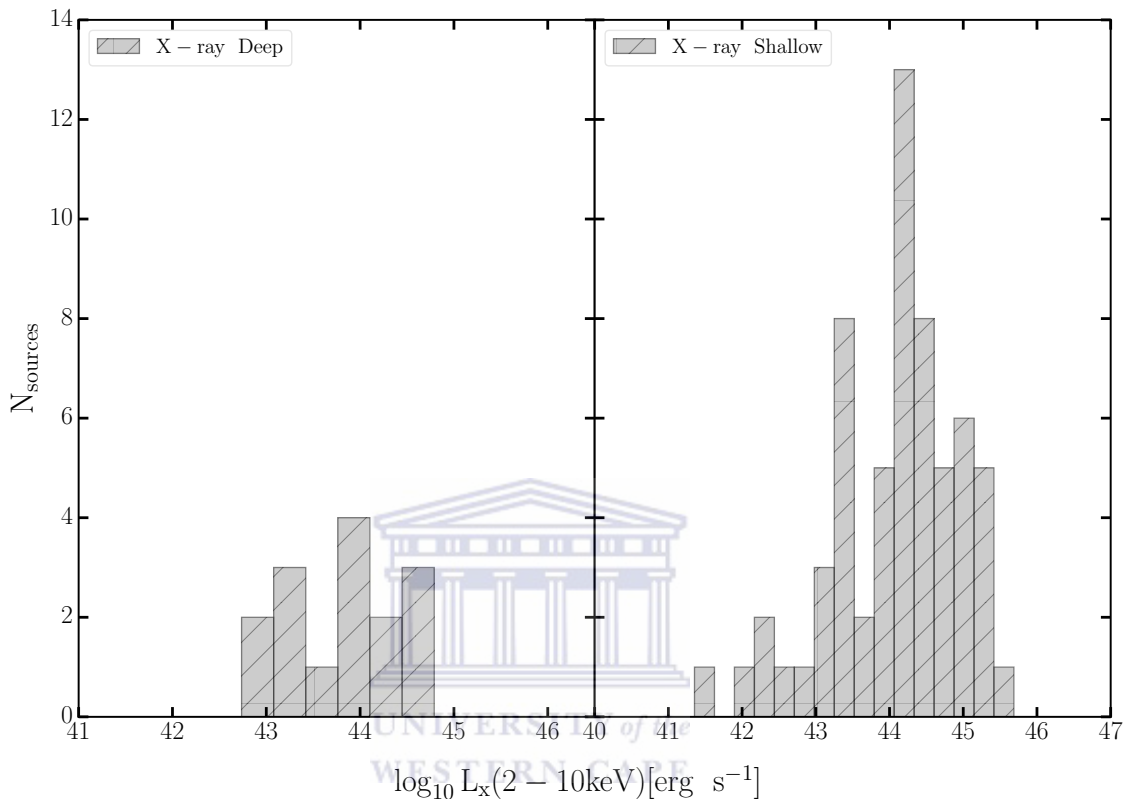


FIGURE 2.4: Histogram of the distribution of our X-ray Deep and X-ray Shallow data.

Figure 2.4 shows the distribution of the X-ray Deep and X-ray Shallow data. In the X-ray Deep panel, we see that all the sources have $L_{2-10\text{keV}} > 10^{42} L_{\odot}$ whereas in the X-ray Shallow panel, we find roughly one source below this x-ray luminosity threshold. We conclude that virtually all X-ray detected sources are consistent with being AGN.

2.3.2 Optical data

Optical data in particular are very crucial to the characterization process, including morphology classification and photometric redshifts of objects. Thus, optical data play a major role in the identification of objects detected at other wavelengths. The EN 1 has many spectroscopic campaigns conducted in the field.

The Baryon Oscillation Spectroscopic Survey (BOSS) is the primary dark-time survey of SDSS-III, the third phase of the Sloan Digital Sky Survey (SDSS; York *et al.* (2000)).

The BOSS redshift survey of 1.5 million massive galaxies aims to measure the distance-redshift relation $d_A(z)$ and the Hubble parameter $H(z)$ with percent-level precision out to $z = 0.7$, using the well-established techniques that led to the first detections of the baryon acoustic oscillations (BAO) feature (Cole *et al.* (2005); Eisenstein *et al.* (2005)). A summary of the detailed survey and scientific goals of the BOSS spectroscopic mapping of the universe is given by Eisenstein *et al.* (2011). Dawson *et al.* (2013) outlined the technical description of the BOSS survey designed to measure the scale of the BAO in the clustering of matter over a larger volume than the combined efforts of all previous spectroscopic surveys of large-scale structure. BOSS uses 1.5 million luminous galaxies as faint as $i = 19.9$ over $10,000\text{deg}^2$ to measure BAO to redshifts $z < 0.7$ (see Dawson *et al.* (2013)). Alam *et al.* (2015) reported that a series of plates were added to the SDSS-III program to observe ancillary science programs because BOSS observations were proceeding ahead of schedule in 2012. These plates have no primary BOSS galaxy and quasar targets but instead consist entirely of ancillary science targets. Further details about the programs and the completeness of each dedicated sample are outlined in Alam *et al.* (2015). In particular, we requested 5 to 10 BOSS plates (each approximately 1 hour) to obtain spectra for the radio sources detected by GMRT (Taylor *et al.*, 2014) in the EN1 field. This spectroscopic follow up of BOSS observations of the EN1 field was done because the field is well-matched to the SDSS-III field-of-view.

2.4 Radio and multi-wavelength data cross-matching

We matched the GMRT catalog against SERVS IRAC12 positions (see Section 2.3). We first used a fixed search radius of 1.5 arc seconds for the GMRT which is approximately 3σ of the astrometric error. Figure 2.5 presents a histogram of the positional errors (astrometric errors) of the GMRT sources, with the dash vertical line indicating the 1.5 arcseconds fixed search radius. From this initial crossmatch, we were able to match 2156 (77 %) radio sources to SERVS IRAC12 positions.

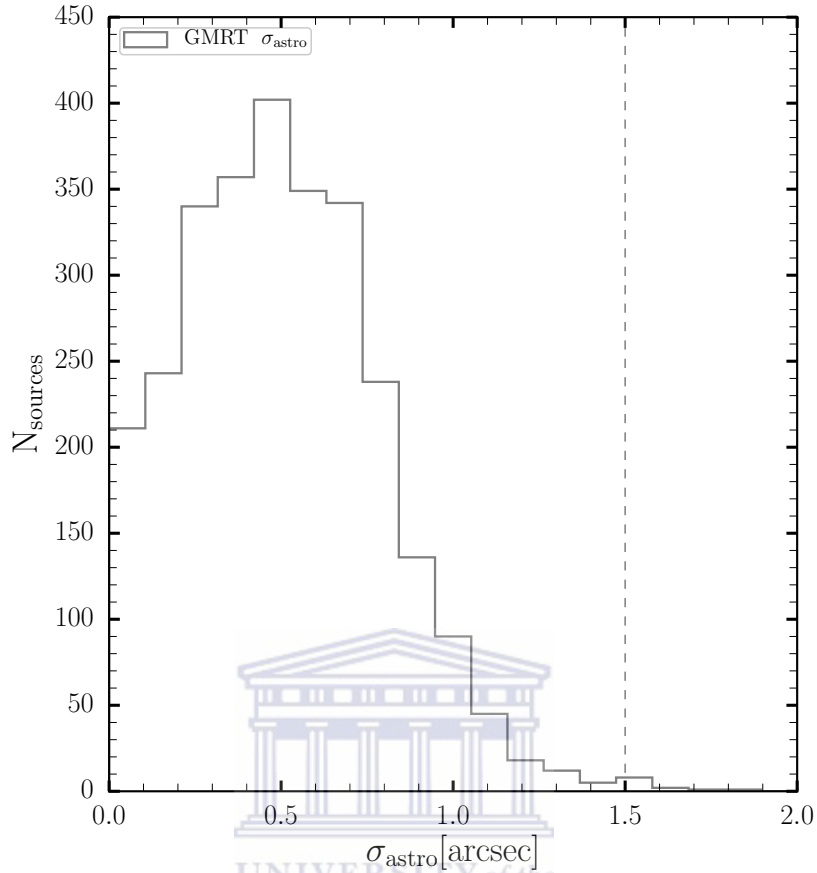


FIGURE 2.5: Histogram of the positional errors (astrometric errors) of the GMRT sources. The dashed vertical line indicates the 1.5 arcseconds which corresponds to $\sim 3\sigma$ fixed search radius

We then improved upon this method using a variable search radius equal to three times the estimated astrometric error. Radio astrometric errors for individual sources produced as part of the data reduction were adopted, and an average SERVS astrometric error of 0.15 arcseconds was assumed based on SERVS vs 2MASS cross-matching. A minimum astrometric error of 0.3 was also assumed for GMRT sources, i.e. about 6% of the 5 arcseconds average beam size, to take into account the optimistic formally very low catalog positional errors for bright radio sources. Figure 2.6 presents the $\sigma_{\text{astro}}[\text{arcsec}]$, the astrometric errors in the radio positions vs the flux density of the GMRT at 1.4 GHz where the dash horizontal line indicated the minimum astrometric error assumed. We computed the median astrometric errors and removed them from the radio positions. We repeated the process to remove any remaining astrometric offsets. Table 2.1 summarizes the results of the cross-matching after this two-step astrometric offset removal. Figure 2.7 presents the GMRT ELAIS N1 mosaic at 610 MHz showing regions of the matched 85% (green circles) and the unmatched 15% (red circles) to SERVS IRAC 12

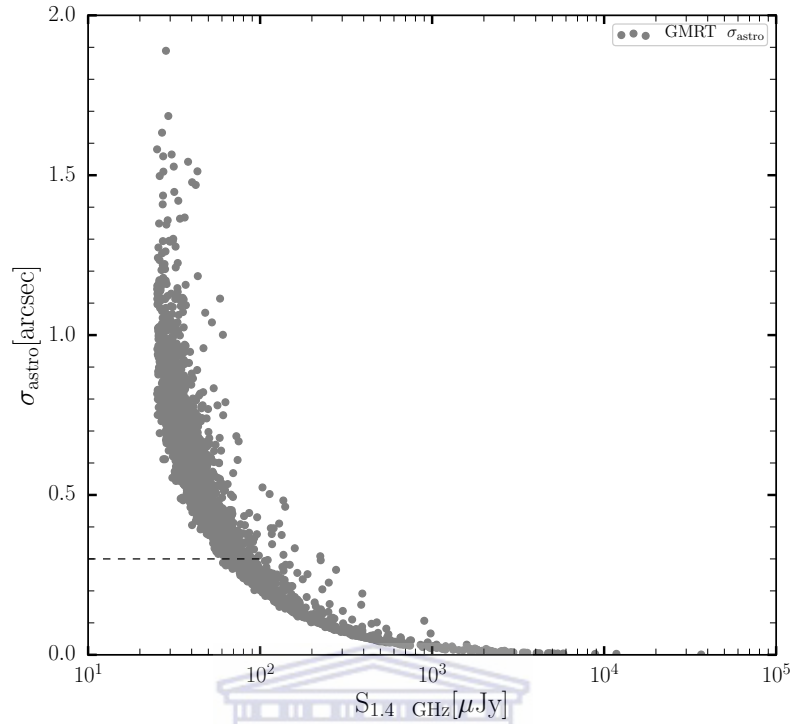


FIGURE 2.6: $\sigma_{\text{astro}} [\text{arcsec}]$, the astrometric errors in the radio positions vs the flux density of the GMRT at 1.4 GHz. The dash horizontal line shows the minimum astrometric error of 0.3 assumed for GMRT sources.

positions. Positional Differences between the GMRT and multi-wavelength ancillary data (SERVS Data Fusion) from the cross correlation of the two catalogs is presented in Figure 2.8. The top panel shows a histogram of the RA and DEC for the matched 85% sources unto SERV SIRAC 12 positions. The bottom panel shows ΔRA vs ΔDEC for the matched sources, whereas the dashed blue circle indicates the position tolerance from the identification in arc seconds.

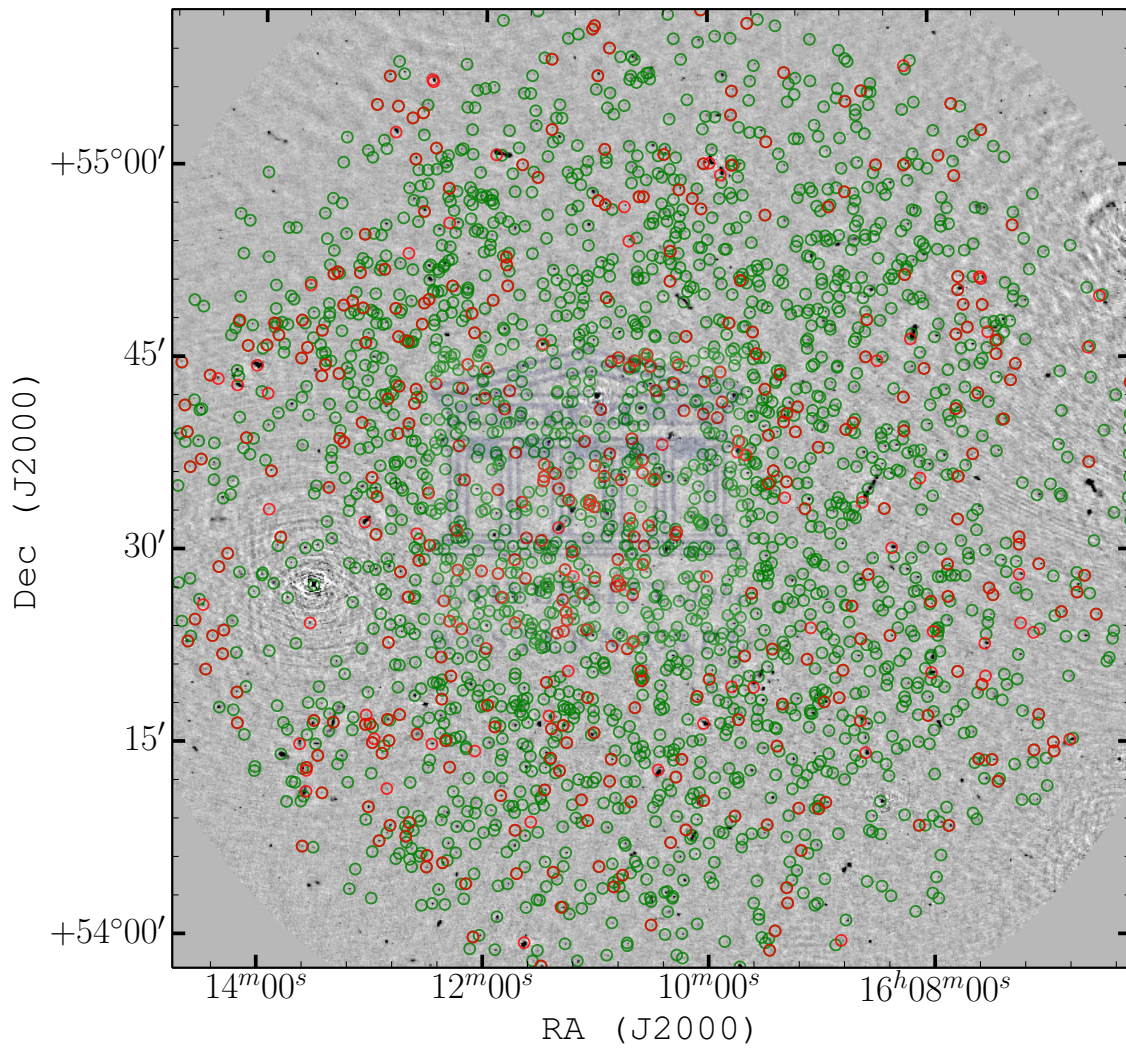


FIGURE 2.7: GMRT ELAIS N1 mosaic at 610 MHz showing positions of the matched 85% (green circles) and the unmatched 15% (red circles) GMRT-SERVS IRAC 12 positions.

TABLE 2.1: GMRT cross-matching statistics. The table shows statistics from our new cross-matching.

Catalog	Size	Fraction (%)
GMRT	2800	100%
SERVS1OR2	2369	85%
SWIRE1OR2	2165	77.3%
SWIRE1234	1091	39%
MIPS 24	1672	60%
SPIRE250	1137	41%
SPIRE350	727	26%
SPIRE500	305	11%
SPECZ-ALL	817	29%
PHOTZ-MRR13	1456	52%
PHOTZ-JWK14	1627	58%
Z-ALL	1760	63%
SPECZ-BOSS(GALAXY)	706	25%
SPECZ-BOSS(AGN)	73	2.6%
MRR13-OPT-GAL	773	27.6%
MRR13-OPT-AGN	27	1.0%
MRR13-IR-GAL	691	24.7%
MRR13-IR-AGN	109	5.9%
MRR13-FIR	1279	45.8%
X-RAY-SHALLOW	96	3%
X-RAY-DEEP	28	1.0%
X-RAY (ALL)	70	2.5%

^a GMRT - Giant Meterwave Radio Telescope.

^b SERVS - Spitzer Extragalactic Representative Volume Survey.

^c SWIRE - SIRTf Wide-Area Infrared Extragalactic Survey.

^d MIPS 24 - Multiband Imaging Photometer 24 micrometer.

^e SPIRE - Spectral and Photometric Imaging Receiver.

^f SPECZ-ALL - total spectroscopic redshifts.

^g PHOTZ-MRR13 - total photometric redshifts from [Rowan-Robinson et al. \(2013\)](#).

^h Z-ALL - total number of sources with redshifts (i.e. both spectroscopic and photometric) .

ⁱ SPECZ-BOSS(GALAXY) - BOSS/SDSS spectroscopic classification of galaxies.

^j SPECZ-BOSS(AGN) - BOSS/SDSS spectroscopic classification of AGNs.

^k MRR13-OPT-GAL - [Rowan-Robinson et al. \(2013\)](#) optical galaxy template classification.

^l MRR13-OPT-AGN - [Rowan-Robinson et al. \(2013\)](#) optical AGN template classification.

^m MRR13-IR-GAL - [Rowan-Robinson et al. \(2013\)](#) infrared galaxy template classification.

ⁿ MRR13-IR-AGN - [Rowan-Robinson et al. \(2013\)](#) infrared AGN template classification.

^o MRR13-FIR - [Rowan-Robinson et al. \(2013\)](#) far-infrared luminosity.

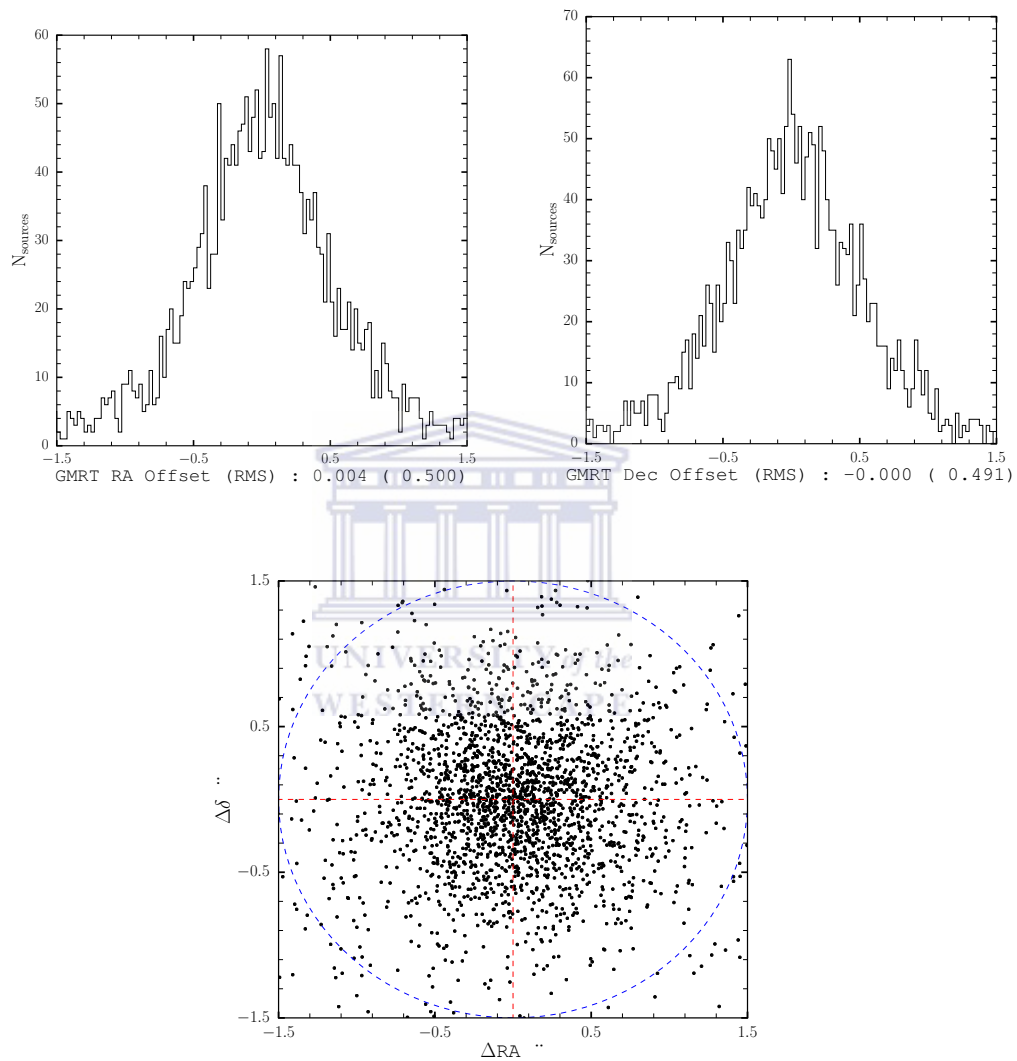


FIGURE 2.8: Positional Differences between the GMRT and multi-wavelength ancillary data (SERVS Data Fusion) from the cross correlation of the two catalogs. The top panel shows a histogram of the RA and DEC for the matched 85% sources unto SERV SIRAC 12 positions. The bottom panel shows ΔRA vs ΔDEC for the matched sources, whereas the dashed blue circle indicates the position tolerance from the identification in arc seconds.

2.4.1 Sources without SERVS 1 OR 2 catalog identifications

We were able to match 85% of GMRT sources to SERVS 1 or SERVS 2 positions (see Table 2.1), thus leaving 15% of the GMRT sources unmatched. Since we want to be able to classify all our sources, we further investigate why 15% of the sources are unmatched. We applied the following criteria to classify the unmatched sources:

- Whether the infrared image is empty and thus there is no clear infrared counterpart to the radio source.
- The region of the infrared counterpart is very bright or confused as a result of 2 infrared sources (blobs) very close together.
- There is an apparent good infrared counterpart (ID) but the source is not in the SERVS catalog.

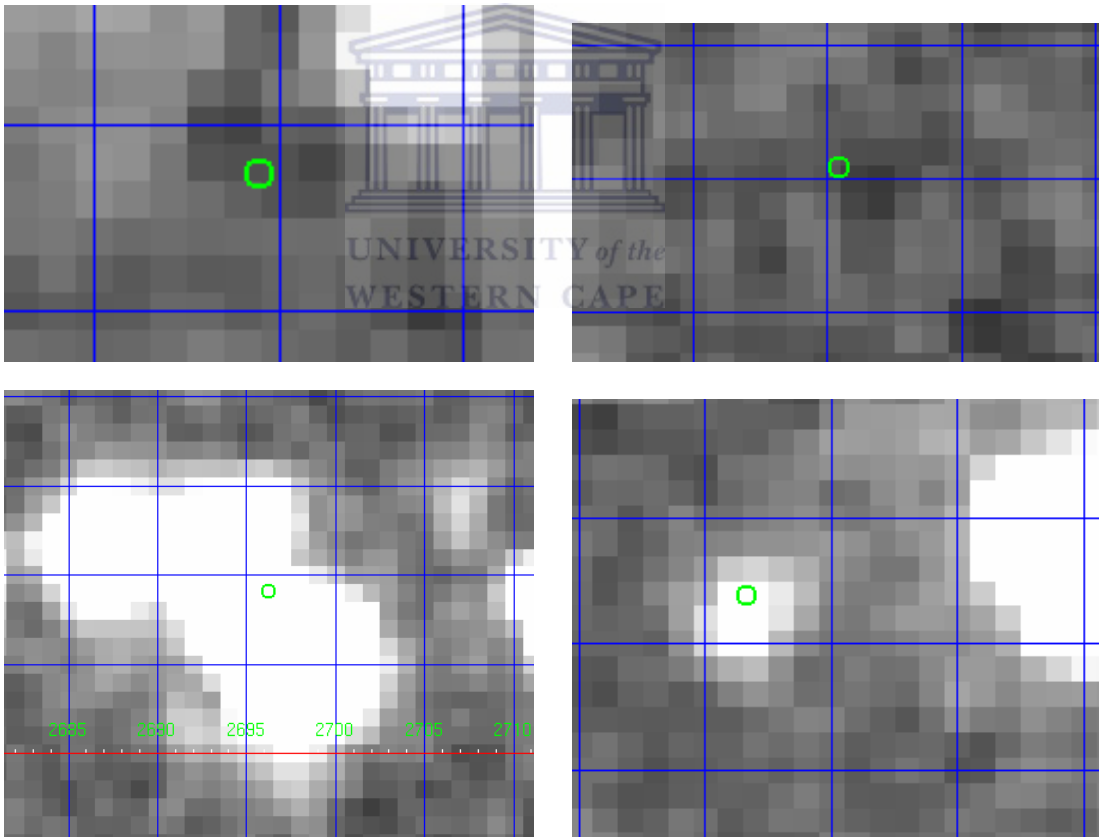


FIGURE 2.9: Classification of the unmatched radio sources to SERVS 1 OR 2 positions into their various categories. The panels corresponds to the infrared image being empty and thus there is no clear infrared counterpart to the radio source (top right) and also whether there is an identification but low possibility (top left). Bottom right: region of the infrared counterpart is very bright. Bottom left: an apparent good infrared counterpart (ID) but the detection software could not detect.

Figure 2.9 presents an example of the unmatched radio sources to SERVS 1 OR 2 positions into their various categories. The image in this figure is the SERVS mosaic with the GMRT position over-laid on the image (indicated by the green circle). Top right panel shows that the infrared image is empty and thus there is no clear infrared counterpart to the radio source therefore, we classify this as "empties" or no "identification". From the top left, we see from the over-laid radio source that the object is far but maybe not too far and that there is a low probability of having a SERVS counterpart (ID). The top panels constitutes 4.4% (124 radio sources out of the total radio population). Considering the bottom right in Figure 2.9, we see that the region of the infrared counterpart is very bright. These SERVS sources are blended and we cannot make a unique ID. This category comprises of 203 sources forming 7.3% of the population of the radio sources. Moreover, the bottom left panel indicates that there are some apparent good infrared counterpart (ID) but the detection software could not detect them. We classify this as good identifications and they form 3.9% (i.e. 109 sources from the total population of the entire radio sources). Table 2.2 presents the breakdown of unmatched radio sources to SERVS 1 OR 2 positions.

Hence from the analyses in this section (Section 2.4.1), we can infer that some of the radio sources actually have identification with SERVS 1 OR 2 positions but the source detections software cannot match them. Therefore, when we consider the "bright/confused" and "good identifications" in Table 2.2, we can actually say that the number of radio sources matched to SERVS 1 OR 2 positions is more than the initial 2369 radio sources (85%) reported in Section 2.4 (see Table 2.1) but is 2681 radio sources which comprises 95% of the radio population.

TABLE 2.2: Classification of the unmatched radio sources to SERVS 1 OR 2 positions into their various categories

Unmatched Sources		
Criteria	Number	Fraction (%)
Empties/No identification /Low probability	124	4.4 %
Bright/Confused	203	7.3%
Good identification	109	3.9%

2.5 Redshifts of identified sources

2.5.1 Spectroscopic redshift

We obtained our spectroscopic redshifts through a follow up campaign of GMRT deep field targets in the in the EN1 with the SDSS-III (BOSS) field (see Section 2.3.2).

The spectroscopic redshifts were obtained through a cross-identification of the available redshifts with your GMRT catalogue. The main BOSS survey program consists of two galaxy target samples (Padmanabhan *et al.* (2012)) whereby galaxy samples are classed CMASS for "constant mass" and LOWZ for "low-redshift". The BOSS spectral classification and redshift-finding analyses are approached as a χ^2 minimization problem where linear fits are made to each observed spectrum using multiple templates and combinations of templates evaluated for all allowed redshifts. Then the global minimum- χ^2 solution is adopted for the output classification and redshift Bolton *et al.* (2012). The basic outputs of the redshift determination and classification algorithm described in Bolton *et al.* (2012) are the measured redshift **Z**, its associated 1-sigma statistical error **Z ERR**, a classification category **CLASS** (either "GALAXY", "QSO" for quasar, or "STAR"), and a confidence flag **ZWARNING** that is zero for confident measurements and non-zero otherwise. The spectroscopic redshift counterparts were identified by cross-matching (see Section 2.4, Table 2.1). In all, we were able to attain spectroscopic redshift associations for 29% of the radio sources. Figure 2.10 presents the spectroscopic redshift distribution of our radio sample.

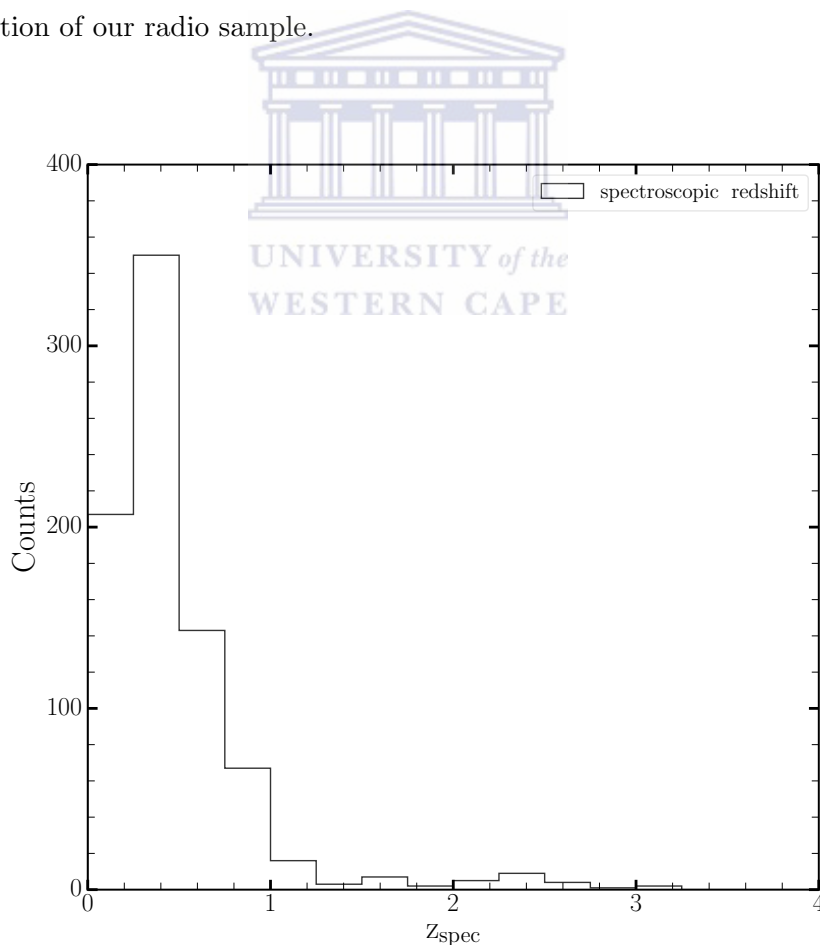


FIGURE 2.10: Histogram of the distribution of spectroscopic redshift for objects with secure spectroscopic redshift detections.

2.5.2 Photometric redshift

In order to increase the redshift completeness of our sample, we also use photometric redshift estimates. We use the photometric redshift catalog compiled by [Rowan-Robinson *et al.* \(2008\)](#) and [Rowan-Robinson *et al.* \(2013\)](#). Rowan-Robinson *et al.* (2008) reported photometric redshifts for over 1 million galaxies in the Spitzer SWIRE survey, the SWIRE Photometric Redshift Catalogue (hereafter SPRC) and gave a detailed review of earlier work on photometric redshifts. They were able to derive photometric redshifts in SPRC for 8.72 deg² of ELAIS-N1 therefore, the GMRT mosaic is fully covered by this dataset. The revised Spitzer Wide-Area Infrared Extragalactic survey (SWIRE) Photometric Redshift Catalogue ([Rowan-Robinson *et al.*, 2013](#)) takes into account new optical photometry in several of the SWIRE areas, and incorporates Two Micron All Sky Survey (2MASS) and UKIRT Infrared Deep Sky Survey (UKIDSS) near-infrared data. The photometric redshift method in [Rowan-Robinson *et al.* \(2013\)](#), is a two-pass template method based on six galaxy (11 in the second pass) and three AGN templates. Galaxy templates were first generated empirically and modelled with a full star formation history so that star formation rates and stellar masses can be derived. After the first pass, the infrared excess relative to the starlight fit was then modelled with four infrared SED types (Cirrus, M82 starburst, Arp 220 starburst and AGN dust torus). Dust extinction with A_V ranging up to 1.0 was permitted. For quasi-stellar object (QSOs), Small Magellanic Cloud (SMC) dust properties were assumed.

The photometric redshift associations were identified by cross-matching (see Section 2.4, Table 2.1). In all, we were able to attain photometric redshift associations for 52% of the radio sources. Figure 2.11 presents the photometric redshift distribution of our radio sample.

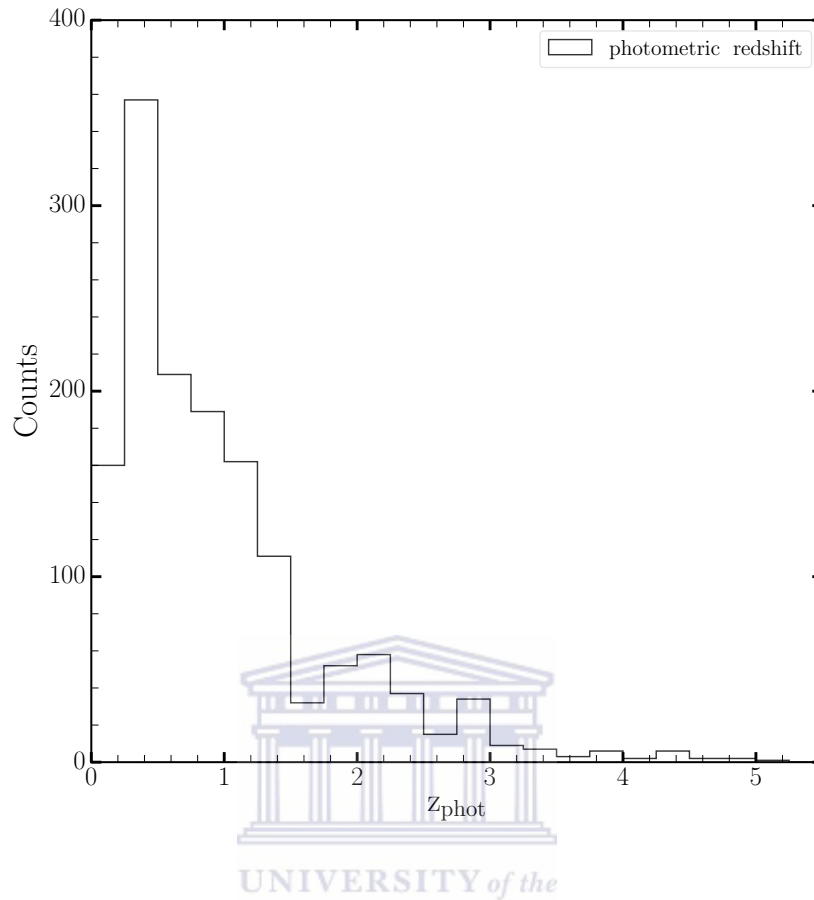


FIGURE 2.11: Histogram of the distribution of photometric redshift for objects with secure photometric redshift detections.

2.5.3 Comparison of spectroscopic and photometric redshift

The most direct method of determining the accuracy of a photometric redshift is by comparison with available spectroscopic data. Figure 2.12 presents a comparison for the GMRT sources with both photometric and spectroscopic associations from the cross-matching (see Section 2.4, Table 2.1). The histograms on the top and the right of Figure 2.12 presents the entire distributions of the photometric and the spectroscopic redshifts respectively. In general, the photometric redshifts compare well to the spectroscopic redshifts, although we note that this comparison is primarily from galaxies at $z_{\text{spec}} < 1.5$. Many of the sources generally follow the one-to-one line (dashed diagonal black line). Conversely, there are also sources which tend to have large departures from this line. The galaxies that are outliers from the one-to-one relation. This scatter can be due to either their redshift errors and can be considered as catastrophic outliers, or to the contamination of AGNs in our sample.

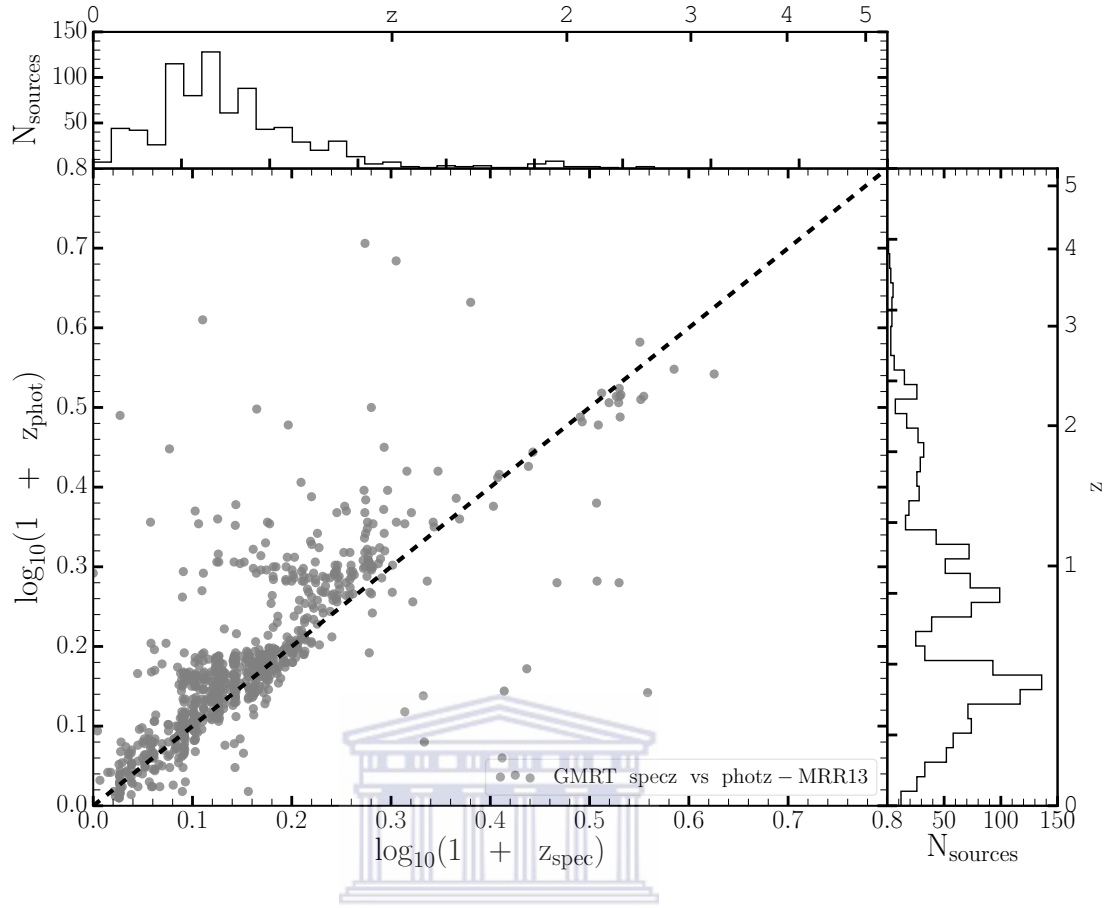


FIGURE 2.12: Comparison between photometric and spectroscopic redshift for the GMRT sources with both photometric and spectroscopic redshift. The solid black line corresponds to $z_{\text{spec}} = z_{\text{phot}}$. The top and right histograms corresponds to that of the spectroscopic and photometric redshifts respectively.

In Figure 2.13 we show the $\Delta z/(1+z)$ distribution between the photometric and spectroscopic redshifts for the sample of our GMRT sources with available spectroscopic and photometric redshift associations. The standard deviation is $\sigma[\Delta z/(1+z)] \sim 0.20$.

Figure 2.14 presents $\Delta z = z_{\text{spec}} - z_{\text{phot}}$ as a function of $\log_{10}(1 + z_{\text{spec}})$ (left panel) and $\log_{10}(1 + z_{\text{phot}})$ (right panel). The vertical line in each panel shows where $\log_{10}(1 + z)$ is = 0.3, above which outliers dominate the right panel. This plot demonstrates that the fraction of outliers increase significantly towards higher values of z_{phot} . This biased behaviour of the photometric redshift has implications for studies of cosmic evolution as it systematically reduces the number of observed sources at low redshift whilst simultaneously enhancing the number of observed sources at higher redshifts. The effect, whilst systematic, is nevertheless small and as such should not have a large impact on the conclusions of this study. Figure 2.15 we plot only $\log_{10}(1 + z_{\text{phot}}) < 0.3$, when outliers are removed. The plot shows that the standard deviation reduces to $\sigma[\Delta z/(1+z)] \sim 0.12$

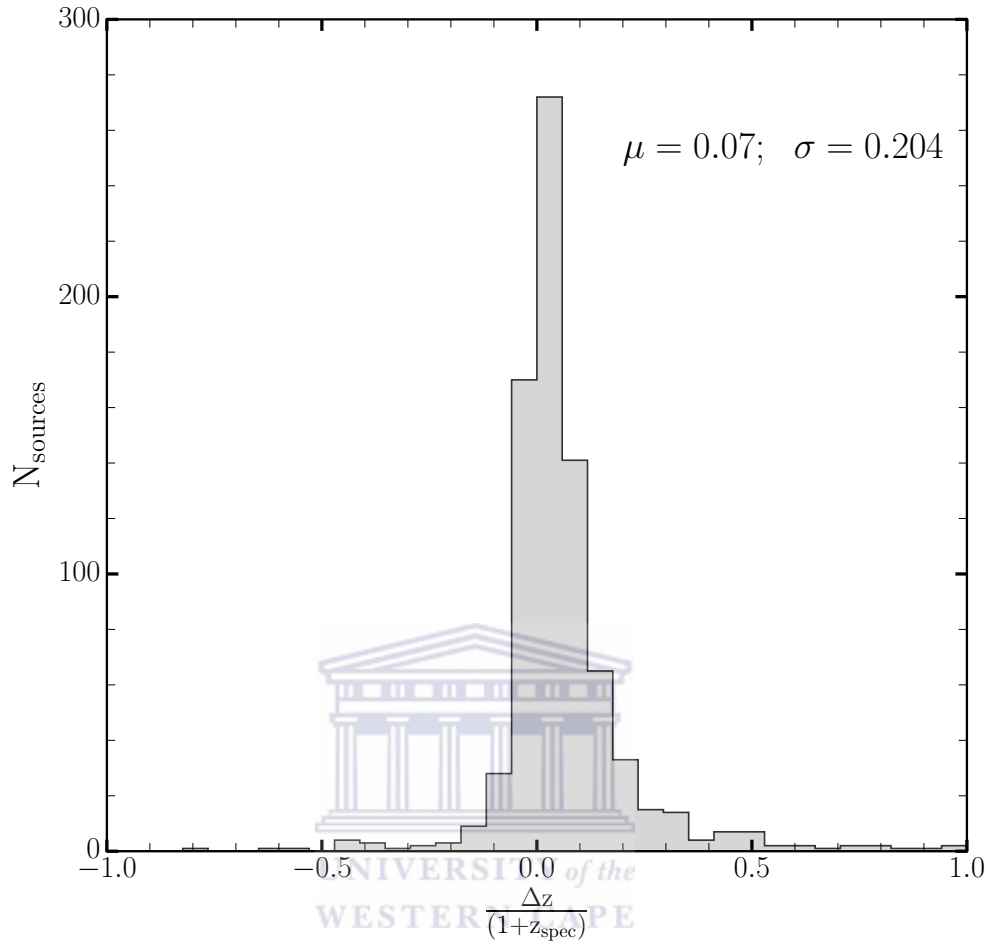


FIGURE 2.13: Comparison of the photometric and spectroscopic redshifts for the GMRT radio sources which spectroscopy is available. The mean (μ), and standard deviation (σ) of the distribution are indicated in the top right of the panel.

and therefore the photometric redshift estimates that we use in this work agrees well with the spectroscopic redshift to about a redshift of ~ 1 .

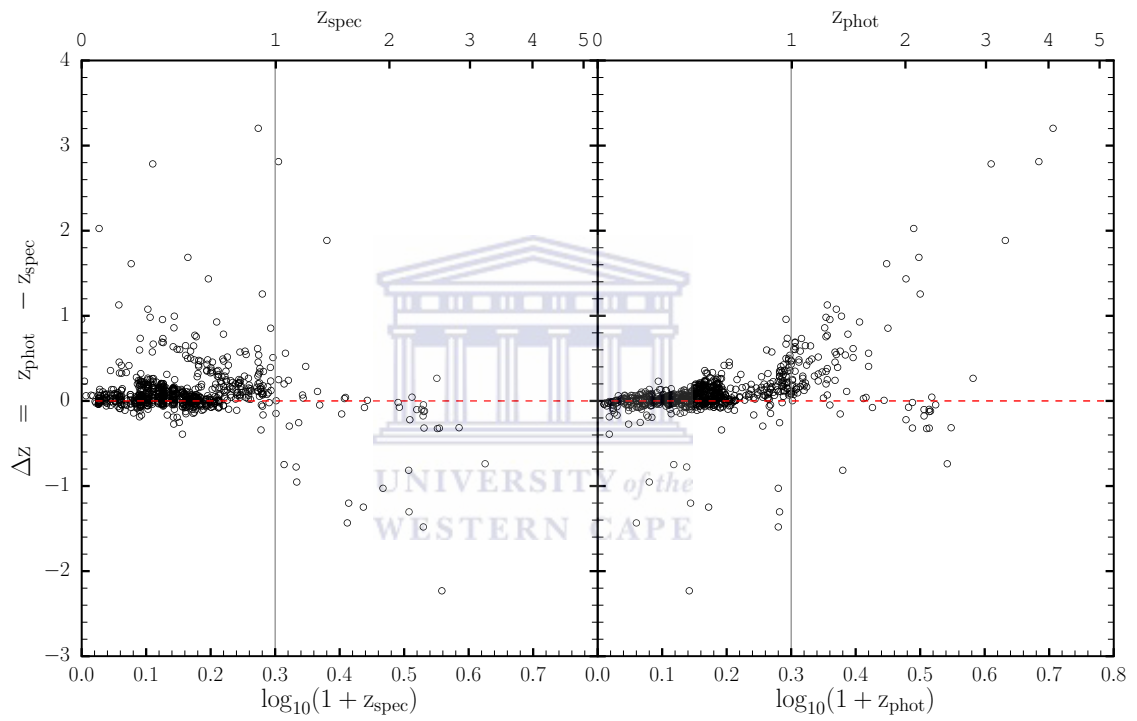


FIGURE 2.14: The $\Delta z = z_{\text{spec}} - z_{\text{phot}}$ as a function of $\log_{10}(1 + z_{\text{spec}})$ (left panel) and $\log_{10}(1 + z_{\text{phot}})$ (right panel) for objects with secure spectroscopic and photometric redshifts.

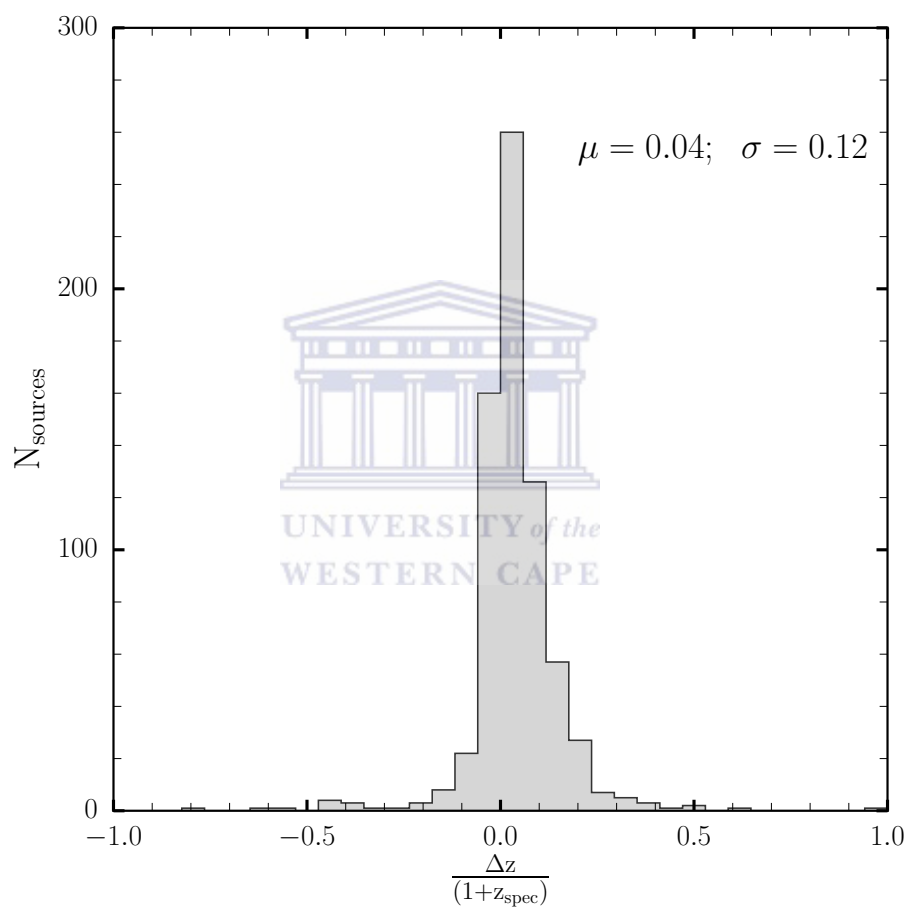


FIGURE 2.15: Same as Figure 2.13, where we have plotted only $\log_{10}(1+z_{\text{phot}})$ is < 0.3 , above which outliers dominate the right panel in Figure 2.14.

2.5.4 Redshift distribution

In the case where both spectroscopic and photometric redshifts are available, we use the spectroscopic one if available and the photometric redshift otherwise. Combining spectroscopic and photometric information, we assign a redshift to 1760 objects, 63% of the radio sources with counterpart (817 spectroscopic redshifts and 943 photometric redshifts). Figure 2.16 presents the redshift distribution for the GMRT sources with an X-ray counterpart (top panel), with a FIR counterpart (middle panel) and with an optical counterpart (bottom panel).



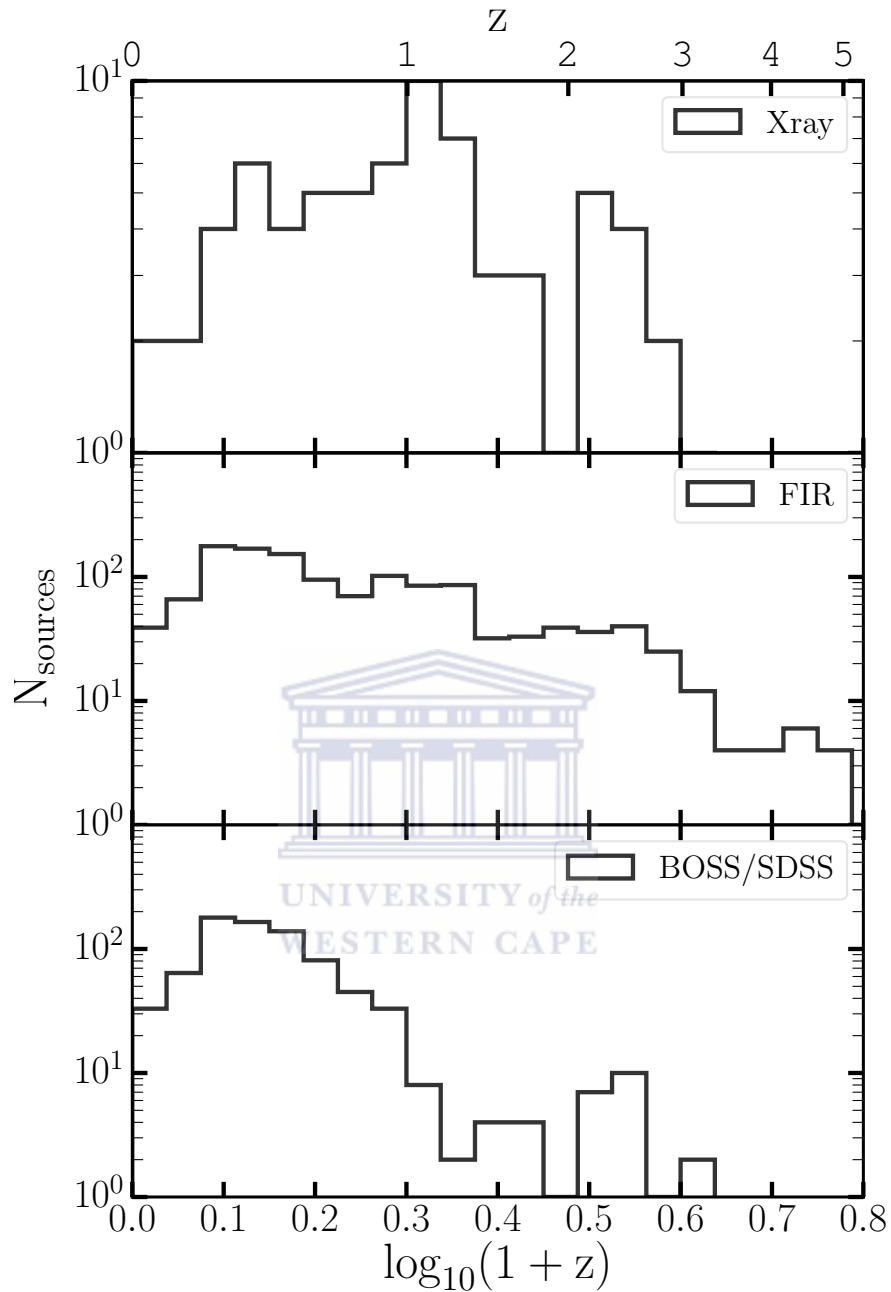


FIGURE 2.16: Redshift distribution for the radio sources with an X-ray counterpart (top panel), with a FIR counterpart (middle panel) and with an optical counterpart (bottom panel).

2.6 Summary

We have presented radio observations and the multi-wavelength ancillary data. The counterpart identification to the radio sources have been outlined.

We have identified the counterparts for a high fraction (85%) of radio sources. We first matched the GMRT catalog to SERVS IRAC12 positions using a fixed search radius of 1.5 arcseconds. This allowed us to obtain only 77% counterparts of our radio sources with SERVS IRAC12 positions in the SERVS Data Fusion. In order to reach a higher completeness, we improved upon this matching using a variable search radius for each source, equal to three times the estimated astrometric error in the GMRT. We further investigated the 15% of the GMRT sources without SERVS 12 catalog identifications and found that 109 sources have good identifications but they are too faint to be detected and included in the SERVS catalogue.

We have presented the spectroscopic and photometric redshift associations of the GMRT sources detected through the cross-match. We were able to associate 1456 sources, comprising 52% of the GMRT population, with photometric redshifts and 817 sources, comprising 29% of the GMRT population, with spectroscopic redshifts. We have compared the photometric redshifts to the spectroscopic redshifts in order to infer the redshift accuracy. In general, we have shown that the photometric redshifts agrees well with the spectroscopic redshifts especially up to $z \sim 1$. We combined the spectroscopic and photometric redshift information such that we adopt the spectroscopic redshift if available otherwise we use the photometric redshift information. From this, we increased the redshift counterparts of the GMRT sources to 1760 (i.e. 63%).

Chapter 3

AGN Diagnostic Techniques

3.1 Introduction

AGNs are broadband emitters and can be identified via a variety of multi-wavelength techniques. In this Chapter, we describe several multi-wavelength diagnostics used to identify AGN.

The bright radio sky is dominated by jet or lobe emission from AGNs and therefore, large radio surveys, e.g. NVSS, can provide numerous samples of radio loud AGNs. However, radio AGNs are only a tiny fraction ($< 10\%$) of the AGN population and therefore the bright radio sky offers a highly biased perspective. Low-excitation AGNs do not show any other signature of activity in other bands rather than the radio (e.g., [Evans et al. \(2006\)](#); [Hardcastle et al. \(2007\)](#)), hence a radio identification is the only way to select them. However, at low flux densities (< 1 mJy), a radio selected sample becomes strongly dominated by SFGs and identifying AGNs using only the radio information becomes more challenging (see [Padovani et al. \(2009\)](#); [Bonzini et al. \(2013\)](#)). Following [Sajina et al. \(2007\)](#) we adopted $L_{1.4\text{GHz}} > 10^{25} \text{ WHz}^{-1}$ as the radio-loud AGN criterion.

In addition, X-ray selection can be a valuable tool for identifying AGN. Deep X-ray surveys from Chandra and XMM-Newton ($E = 0.5 - 10$ keV) have been successful in revealing thousands of AGN (e.g. see [Giacconi et al. \(2002\)](#); [Alexander et al. \(2003\)](#); [Hasinger \(2004\)](#); [Mainieri et al. \(2007\)](#)). X-ray emission in AGN is thought to form in a hot corona around the accretion disk. Electrons in the corona inverse-Compton scatter optical and UV accretion disk photons to higher (i.e. X-ray) energies. These X-rays can readily pierce through the obscuring medium, provided that the "torus" is not Compton-thick. Extinction due to the host galaxy also generally has a negligible impact on X-ray attenuation.

From [Spinoglio and Malkan \(1989\)](#) the mid-infrared (MIR) emission constitutes 20% of the bolometric flux for both Type 1 and Type 2 AGN. The obscuring medium surrounding the AGN absorbs optical and UV accretion disk photons and re-radiates the emission in the IR. Thus AGNs can be identified based on their IR emission hence providing a useful tool for selecting those sources where the optical and UV emission are blocked from the line of sight due to the obscuring effect of the "dusty torus". These identification methods include selecting AGN using ratios of flux densities ([Lacy et al., 2004](#)) or the difference in magnitude ([Stern et al., 2005](#)). One can also use the power-law shape of the mid-infrared spectral energy distribution as shown by [Donley et al. \(2007, 2010\)](#)

In the optical, AGNs can be distinguished from star-forming galaxies (SFGs) by the ratios $[N II]/H\alpha$ vs $[O III]/H\beta$ using the diagnostic plot known as the Baldwin, Phillips, Terlevich (BPT) diagram ([Baldwin et al., 1981](#)). Applying the [Kauffmann et al. \(2003\)](#) empirical division between star-forming galaxies (SFGs) and AGNs, as well as the [Kewley et al. \(2001\)](#) theoretical division curves we can classify our sources as AGNs, SFGs and composites (i.e. the sources residing between these two boundaries). Star-formation can not be ruled out as being responsible for the emission in composite sources while an increasing amount of nuclear activity may also be likely, moving these sources off the sequence of SFGs and closer to AGN.

All of these different selection methods have various shortcomings. For example, dusty host galaxies can attenuate the optical emission lines (e.g. $[O III]5007\text{\AA}$) used to identify AGN, therefore causing some AGN to be missed. AGN samples selected by IR methods can be contaminated by star-forming galaxies. X-ray emission will be extinguished in Compton-thick sources due to both photo-electric absorption of X-ray photons and Compton scattering of photons out of the line of sight. Even hard X-ray surveys will then be biased against the Compton-thick population. Thus in this Chapter, we investigate the radio through to the X-ray properties that characterize AGN and star formation activity along the sequence of star-forming galaxies to composites to AGN. We investigate the various AGN activity diagnostic techniques and study the discrepancies between these various diagnostics.

3.2 AGN selection

3.2.1 Radio selection of AGNs

The main mechanism of radio continuum emission in both AGNs and SFGs is the synchrotron emission. Synchrotron radiation is produced when relativistic particles (usually

electrons) are accelerated in a magnetic field. In SFGs cosmic ray electrons are accelerated in supernova (SN) explosions of massive ($M > 8M_{\odot}$) stars, while in AGNs the electrons are accelerated in relativistic jets powered by the accretion onto a supermassive black hole.

We study the radio luminosity distributions of our sources. In order to derive the luminosities of galaxies, we k-corrected the observed flux density S_{ν} at frequency ν to get a rest-frame luminosity L_{ν} at the same frequency (see Chapter 2 Section 2.2). The luminosity of a source at redshift z and luminosity-distance d_L is therefore given by:

$$L_{\nu} = \frac{4\pi d_{\text{lum}}^2}{(1+z)} S_{\nu}^{\text{obs}} (1+z)^{-\alpha} = 4\pi d_{\text{lum}}^2 \frac{S_{\nu}^{\text{obs}}}{(1+z)^{1+\alpha}} \quad (3.1)$$

Mauch and Sadler (2007) derived the local radio luminosity function (RLF) for the 6dFGS-NVSS sample. As shown in Figure 3.1 at $P_{1.4\text{GHz}} = 10^{23} \text{ WHz}^{-1}$, SFGs dominate the population of radio sources while radio-loud AGNs dominate the population above it.

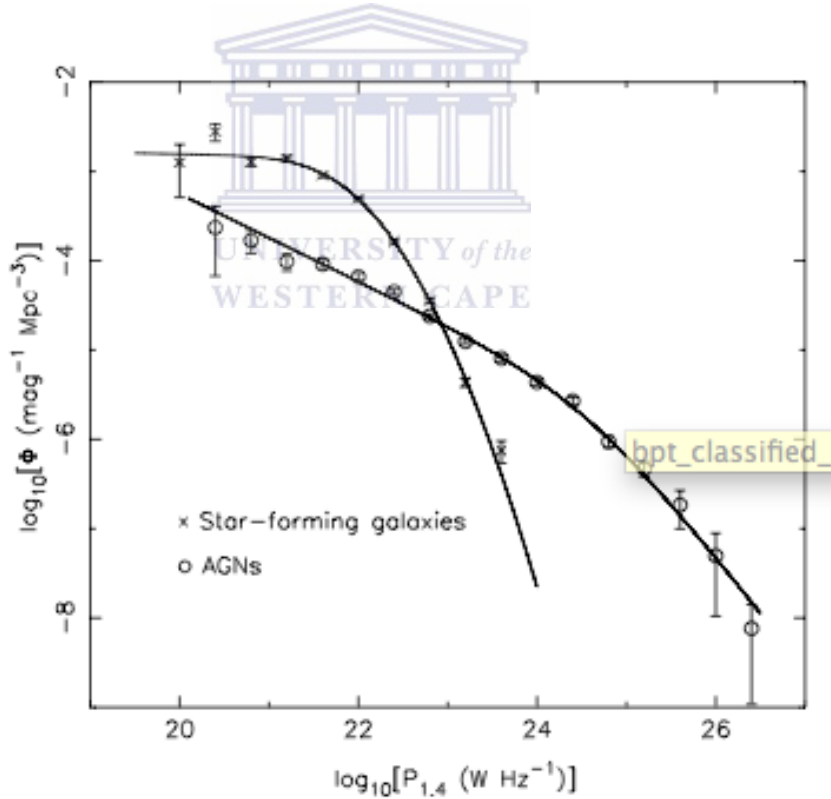


FIGURE 3.1: The local luminosity function at 1.4 GHz derived separately for the radio-loud AGNs (circles) and SF galaxies (crosses) in the 6dFGS-NVSS sample. Adopted from Mauch and Sadler (2007)

In classifying sources as radio-loud AGNs based on their radio luminosity, we adopted $L_{1.4\text{GHz}} > 10^{25} \text{ WHz}^{-1}$ (e.g., Sajina *et al.* (2007); Jiang *et al.* (2007); Sajina *et al.* (2008)). We note that this is a very conservative criterion, as it allows one to select

only the brightest radio-loud galaxies and quasars. The AGN RLF is rather flat at low powers, indicating that we have a large fraction of radio galaxies also below the power cutoff assumed in this work. The dash horizontal black line in Figure 3.2 indicates the sources we select according to this criterion. From the histogram in Figure 3.2, we see that this classification only selects a small number of sources out of the whole GMRT population. The dash horizontal blue line in the histogram shows the median value of the computed radio luminosities. According to this selection criterion, we select only 26 radio sources constituting 0.6% of our entire radio population.

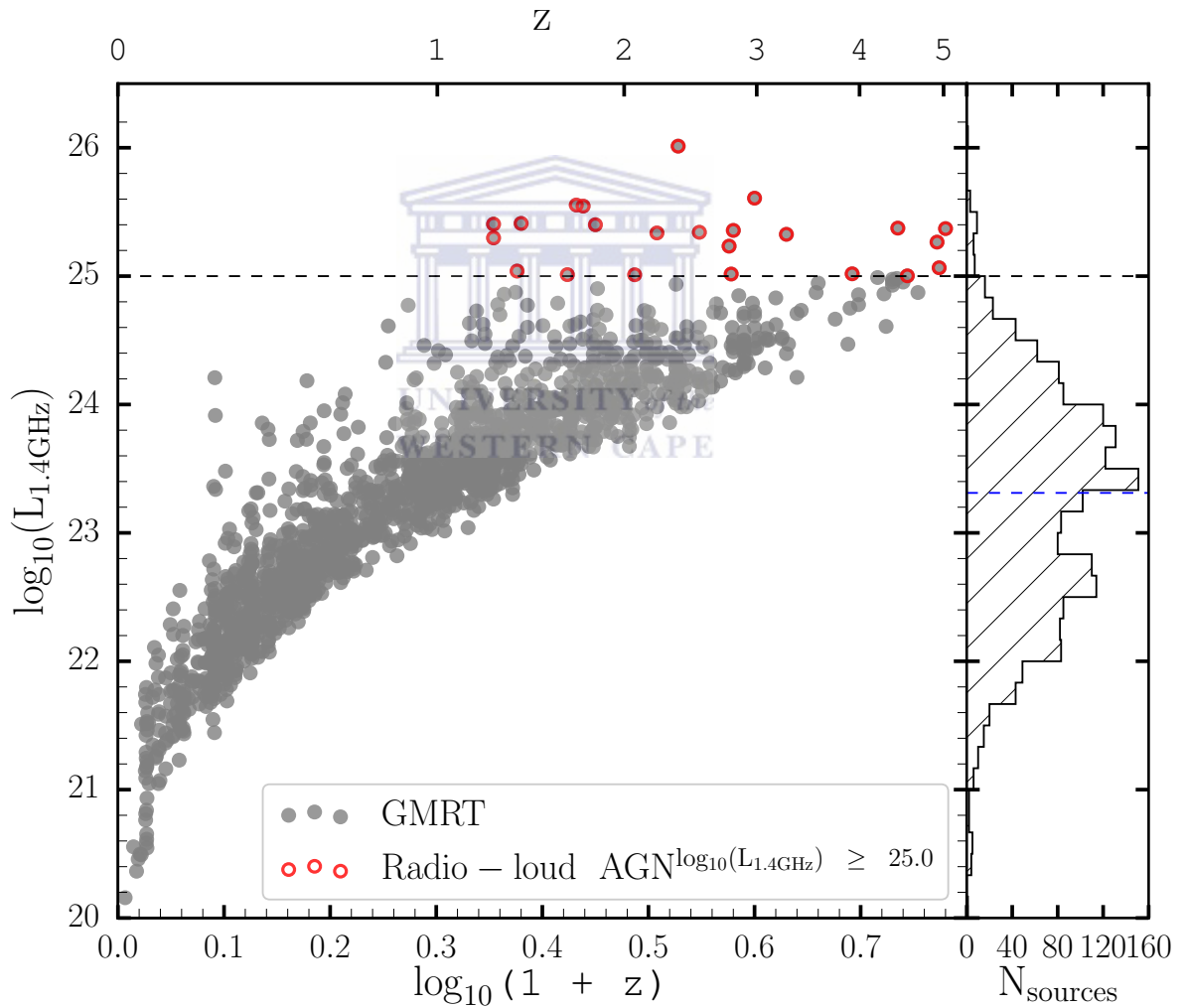


FIGURE 3.2: 1.4 GHz luminosity versus redshift plot for the GMRT sample with redshift detections. The dashed black line shows a commonly adopted radio luminosity threshold to classify a source as a radio-loud AGN (see e.g. Jiang *et al.* (2007); Sajina *et al.* (2008)). The open red circles represents the sources selected according to this classification criteria.

3.2.2 X-ray selection of AGNs (X-ray Luminosities)

X-ray surveys are one of the cleanest methods to select AGN since they can directly probe their high energy emission. The situation is more complex when dusty tori obscure the X-ray emission and reprocess it into infrared emission. Thus, the AGN detections through X-ray and infrared are somewhat complementary.

For X-ray detected GMRT sources, we compute the X-ray luminosity (2 -10 keV) using the relation below.

$$L_X = 4\pi \times S_X \times d_L^2 (1+z)^{2-\gamma} \quad (3.2)$$

We fix the photon-index to the commonly observed value $\gamma = 1.8$ (Dadina, 2008). We use both the X-ray deep and X-ray shallow data, outlined in Section 2.3.1 of Chapter 2. If available, we adopt the X-ray deep information. Where there is no x-ray deep, we adopt the x-ray shallow information. In Figure 3.3, it can be seen that most of the sources (as outlined in Table 2.1) have $L_{2-10\text{keV}} > 10^{42} \text{ erg s}^{-1}$. However, there is one source which resides in the "Galaxies" regime in Figure 3.3. This source does not meet the criterion above, so we do not classify this particular source as an AGN. We adopted the cut mentioned in Section 2.3.1 in order to select a source as an AGN. By using the $10^{42} \text{ erg s}^{-1}$ cut as our selection criterion, we select 70 radio sources constituting 2.5% of the GMRT radio population.

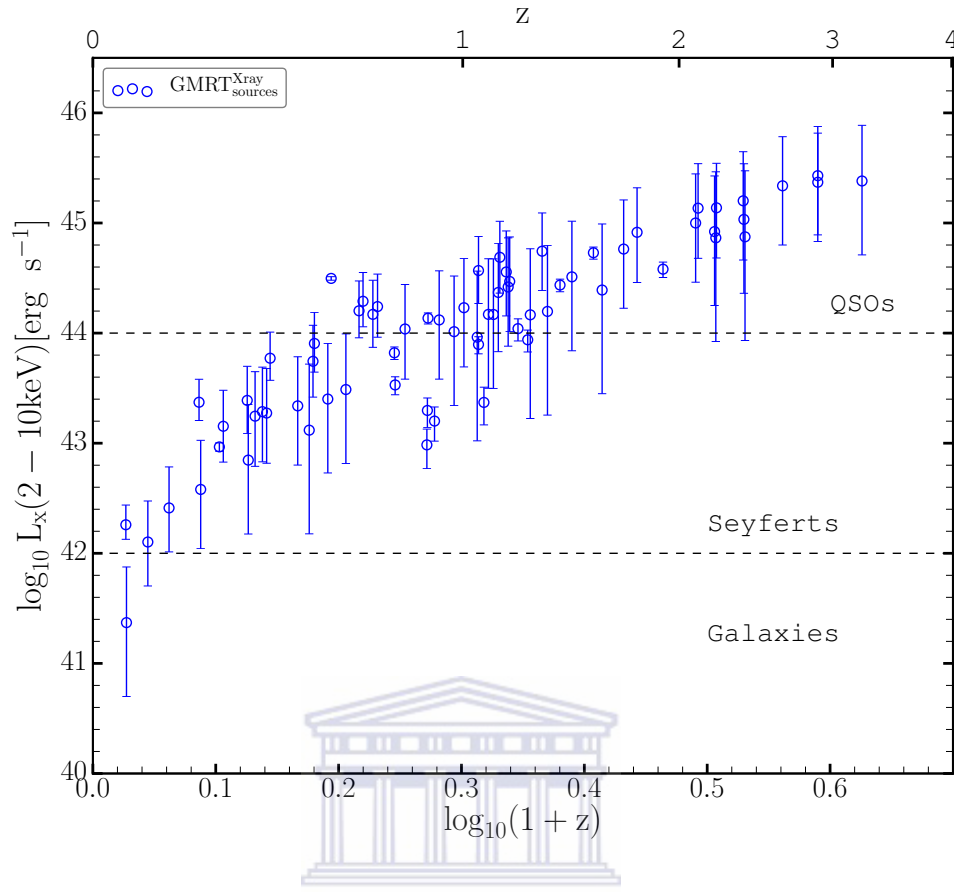


FIGURE 3.3: X-ray luminosity as a function of redshift for the GMRT sources with X-ray detections. The dash horizontal line represents the typical demarcations for Galaxies, Seyferts and QSOs.

3.3 BOSS/SDSS classification

The BOSS spectroscopic classifications (stored in **CLASS** and **SUBCLASS** parameters Bolton *et al.* (2012)) are as follows:

1. GALAXY: identified with a galaxy template; can have subclasses:

- STARFORMING : the galaxy has detectable emission lines that are consistent with star-formation according to the criterion:

$$\log_{10}(\text{OIII}/\text{H}\beta) < 0.7 - 1.2(\log_{10}(\text{NII}/\text{H}\alpha) + 0.4)$$
- STARBURST: galaxy is star-forming with an equivalent width of $\text{H}\alpha$ greater than 50 \AA
- AGN: the galaxy has detectable emission lines that are consistent with being a Seyfert or LINER:

$$\log_{10}(\text{OIII}/\text{H}\beta) > 0.7 - 1.2(\log_{10}(\text{NII}/\text{H}\alpha) + 0.4)$$

2. QSO: identified with a QSO template.
3. STAR: identified with a stellar template.

In addition, if any galaxies or quasars have lines detected at the 10-sigma level with velocity dispersion > 200 km/sec at the 5-sigma level, the indication 'BROADLINE' is appended to their subclass. From Chapter 2, Table 2.1, 706 of the GMRT sources with SDSS/BOSS spectroscopic identifications are classed as SFGs whilst 73 sources are identified as AGNs (QSOs). These AGNs are defined only according to those sources satisfying criterion 1. However, when we include sources satisfying criterion 2 (from the SUBCLASS parameter), the number of AGNs selected increases to 96 sources constituting of 3.4% of the GMRT population. These sources comprises "Broadline", "Starburst Broadline", "QSO" and "AGN" SUBCLASS classifications. Table 3.1 presents the breakdown of the number of the **CLASS** and **SUBCLASS** parameters of the BOSS spectroscopic classifications.

TABLE 3.1: Table showing the number of the **CLASS** and **SUBCLASS** for the BOSS spectroscopic classifications.

Category	CLASS Number	SUBCLASS Number
Starforming	0	172
Starburst	0	141
Starburst Broadline	0	4
Broadline	0	43
Galaxy	706	0
QSO	73	0
AGN	0	19
Star	0	3

^a Starforming - described by BOSS spectroscopic **SUBCLASS** as "Starforming".

^b Starburst - described by BOSS spectroscopic **SUBCLASS** as "Starburst".

^c Starburst Broadline - described by BOSS spectroscopic **SUBCLASS** as "Starburst Broadline".

^d Broadline - described by BOSS spectroscopic **SUBCLASS** as "Broadline".

^e Galaxy - described by BOSS spectroscopic **CLASS** as "Galaxy".

^f QSO - described by BOSS spectroscopic **CLASS** as "QSO".

^g AGN - described by BOSS spectroscopic **SUBCLASS** as "AGN".

^h Star - described by BOSS spectroscopic **CLASS** as "star".

3.4 MIPS 24 micron flux

We used the MIPS (Rieke *et al.*, 2004) $24_{\mu\text{m}}$ flux density and the effective 1.4 GHz flux density to calculate the $q_{24_{\mu\text{m}}}$ parameter, which is the logarithm of the ratio of IR to radio flux density. The $q_{24_{\mu\text{m}}}$ parameter is given by :

$$q_{24_{\mu\text{m}}} = \log_{10}(S_{24_{\mu\text{m}}}/S_{1.4\text{GHz}}) \quad (3.3)$$

From Table 2.1, we have 1672 GMRT sources with MIPS 24 micron detections, 1408 of these detections have redshift associations constituting $\sim 50.3\%$ of the entire GMRT population. The distribution of the MIPS 24 micron IDs with redshift detections for our GMRT sample is presented in Figure 3.4. From Equation 3.3, we compute the $q_{24_{\mu\text{m}}}$ for the radio sources with MIPS $24_{\mu\text{m}}$ detections and compare it to the redshifted $q_{24_{\mu\text{m}}}$ value of the M82 (local standard starburst galaxy) template used by Bonzini *et al.* (2013) to identify SFGs and radio-loud AGNs. The M82 template is normalised by the local average value of $q_{24_{\mu\text{m}}}$. Sargent *et al.* (2010) defined this average value $q_{24_{\mu\text{m}}}$ as $\langle q_{24_{\mu\text{m}}} \rangle = 1.31^{+0.10}_{-0.05}$ for sources with $0.08 < z < 0.23$. We measure a median $q_{24_{\mu\text{m}}} = 0.86 \pm 0.01$ for our sample with MIPS 24 micron detections. This is in agreement with previous work from Appleton *et al.* (2004) who estimated $q_{24_{\mu\text{m}}} = 0.84 \pm 0.28$ by matching Spitzer sources at 24μ with VLA 1.4 GHz μJy radio sources obtained for the Spitzer First Look Survey (FLS).

Figure 3.5 presents the $q_{24_{\mu\text{m}}}$ parameter against redshift for the MIR detected GMRT sources with redshift along with the curve showing predicted value of M82 template. The grey pixels represent a two dimensional histogram of our GMRT sources with MIPS 24 micron detections having redshift associations. The radio-loud AGNs selected from this method reside below the -2σ dispersion curve (see the blue triangles). This selection criterion, selects 42 radio sources constituting $\sim 1\%$ of our entire radio population. We compare this method to the radio-loud AGN classification presented in Section 3.2.1. From the total of 26 sources selected as radio-loud AGNs in Section 3.2.1 only 15 have MIR detections. Among them, 5 of these sources agree with the $q_{24_{\mu\text{m}}}$ vs $\log_{10}(1+z)$ radio-loud selection criterion. Ten radio-loud AGN selected sources from Section 3.2.1 Figure 3.2 reside in star forming galaxy/radio-quiet AGN regime. These sources residing in the galaxy/radio-quiet AGN regime must be very dusty hybrids.

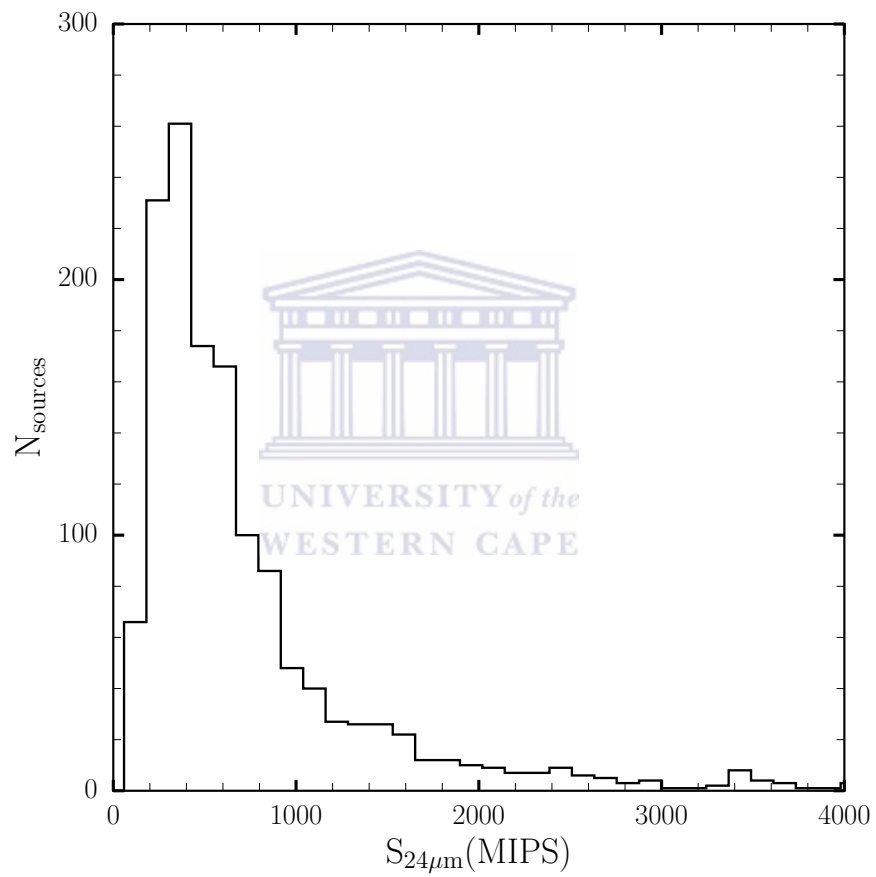


FIGURE 3.4: The distribution of the MIPS 24 micron IDs with redshift detections for our GMRT sample.

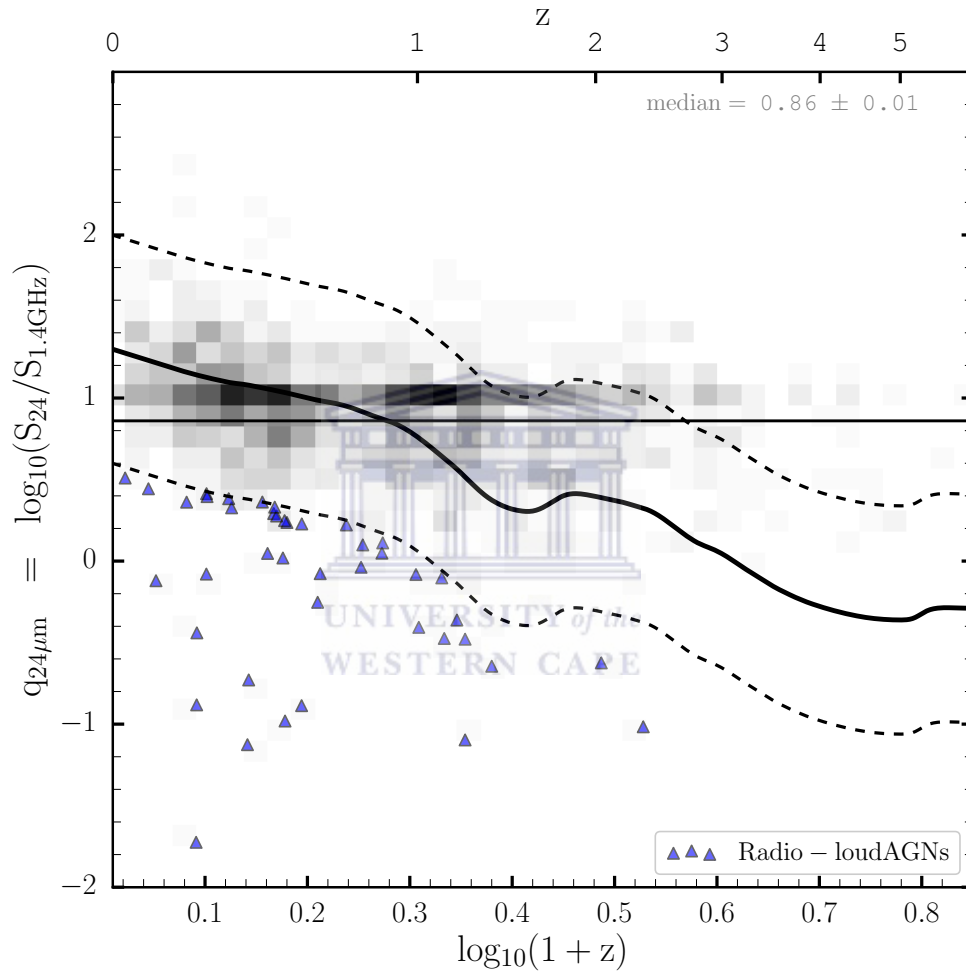


FIGURE 3.5: $q_{24\mu m}$, the logarithm of the ratio between the MIR and radio flux for the GMRT sources with redshift detections. The curve shows the predicted value of M82 template, the dividing line between radio quiet and radio-loud AGNs with $\pm 2\sigma$ dispersion (dash curve). The horizontal line is the weighted median value of $q_{24\mu m}$ for the sources

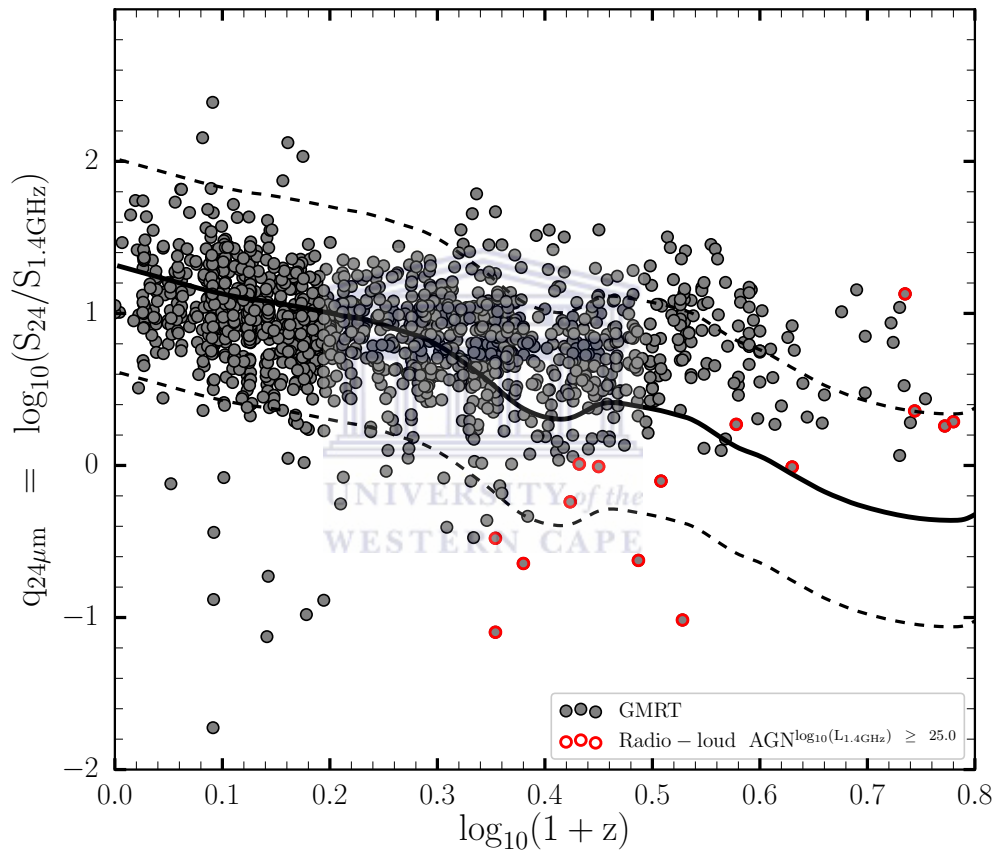


FIGURE 3.6: $q_{24\mu\text{m}}$ vs $\log_{10}(1+z)$ for the GMRT sources with MIPS $24\mu\text{m}$ with redshift detections. Over-plotted are the radio-loud AGN classification from the adopted radio luminosity threshold (see Section 3.2.1 Figure 3.2)

3.5 AGN classification

We combine the four AGN selection methods discussed as our surest AGN candidates up to this point in the work. Table 3.2 presents a breakdown of the various selections (i.e. radio, X-ray, BOSS/SDSS spectroscopy and the MIPS 24 micron flux density). Thus by combining these, we select 191 (7%) sources of the entire GMRT population as AGNs. From the 63% of our radio sources with redshift information (Chapter 2 Section 2.4), this selection constitutes 11% of this population (i.e. sources with redshift). A schematic of this AGN selection is presented in Figure 3.7

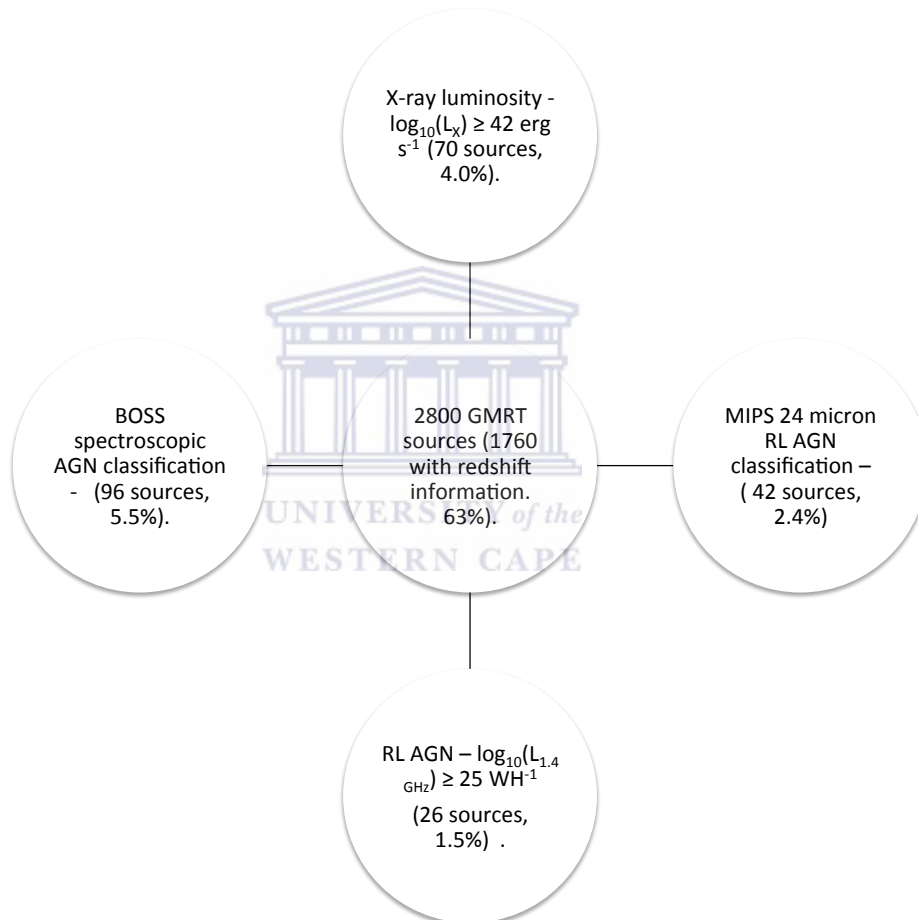


FIGURE 3.7: A schematic of AGN selection from the radio, x-ray, BOSS/SDSS spectroscopy and the MIPS 24 micron flux density. Note that the percentages presented here are with respect to the sources with redshift.

TABLE 3.2: Table showing the breakdown of AGN selection from the radio, X-ray, BOSS/SDSS spectroscopy and the MIPS 24 micron flux density for the sources with redshift.

Category	AGNs	AGNs Fraction (%)
Radio luminosity (radio-loud AGN)	26	1.5%
X-ray luminosity	70	4.0%
BOSS/SDSS classification	96	5.5%
MIPS 24 micron	42	2.4%
Total number of AGN	191	11%

^a Criterion for radio-loud selection of AGNs according to their radio luminosity (see [Jiang et al. \(2007\)](#)).

^b Criterion for X-ray selection of AGNs according to their X-ray luminosity.

^c AGN classification satisfying the BOSS/SDSS spectroscopic pipeline criterion.

^d Radio luminosity (radio-loud AGN) classification according to the MIPS 24 micron criteria following [Bonzini et al. \(2013\)](#).

3.6 MIR color evolution of galaxies

Different levels of star-forming processes in different types of galaxies, result in different mid infrared (MIR) colors. Thus it is important to understand the correlation between the star-forming processes in a galaxy and the color indices of the galaxy as a whole. Instead of classifying galaxies according to their morphologies, it is possible to classify them according to their colors. Furthermore, star-formation rate changes as galaxies evolve, which enables us to study the color evolution of galaxies.

In order to see the color evolution of our sources in the infrared regime, we plot $[5.8] - [8.0]$ (Vega) (top panel) and $[3.6] - [4.5]$ (Vega) (bottom panel) vs $\log_{10}(1 + z)$ presented in Figure 3.8. For the Vega magnitudes, we applied the following conversions:

$$F_{\nu [Jy]} = F_{\nu} \cdot 10^{-0.4m_{AB}} \quad (3.4)$$

where $F_{\nu} = 3631$ Jy (following [Oke and Gunn \(1983\)](#))

$$\therefore m_{AB} = -2.5 \cdot \log_{10} F_{\nu} + 8.9 \quad (3.5)$$

Over-plotting the AGN selection as indicated by Figure 3.7 and the BOSS/SDSS spectroscopic pipeline galaxy classification, we see that galaxies generally follow a trend as it is evident by the BOSS/SDSS galaxy (black stars) in both the top and bottom panels. At $0.2 \lesssim z \lesssim 0.5$, galaxies appear redder in $[3.6] - [4.5]$ due to a combination of μm PAH features shifting through the IRAC $4.5\mu\text{m}$ band (for actively star-forming galaxies) and the deep $2.35 - 2.5\mu\text{m}$ CO absorption due to red supergiants (e.g. see

TABLE 3.3: Table showing the various conversion we applied in converting to the Vega magnitude system. The zero point fluxes are in μJy .

Band	conv	F_{zp}
IRAC-1	2.78	277.5
IRAC-2	3.26	179.5
IRAC-3	3.75	116.5
IRAC-4	4.38	63.1

[Förster Schreiber \(2000\)](#)) shifting through the IRAC 3.6 μm band for old stellar populations). There is a clear evolution between color and redshift at $z \simeq 1$ in Figure 3.8 (both panels). [Martinez-Manso *et al.* \(2014\)](#) showed that [3.6] – [4.5] (Vega) colors the strong correlation between color and redshift at $z > 0.6$ occurs because the IRAC bands map the galaxy spectrum across the stellar bump at rest-frame H-band going from $z = 0.6$ to $z = 2$. This results in a monotonic change in the observed color within $z = 0.6$ to $z = 2$. An insightful description of this phenomenology can be found in [Muzzin *et al.* \(2013\)](#). Conversely, AGNs deviate from the trend followed by galaxies.



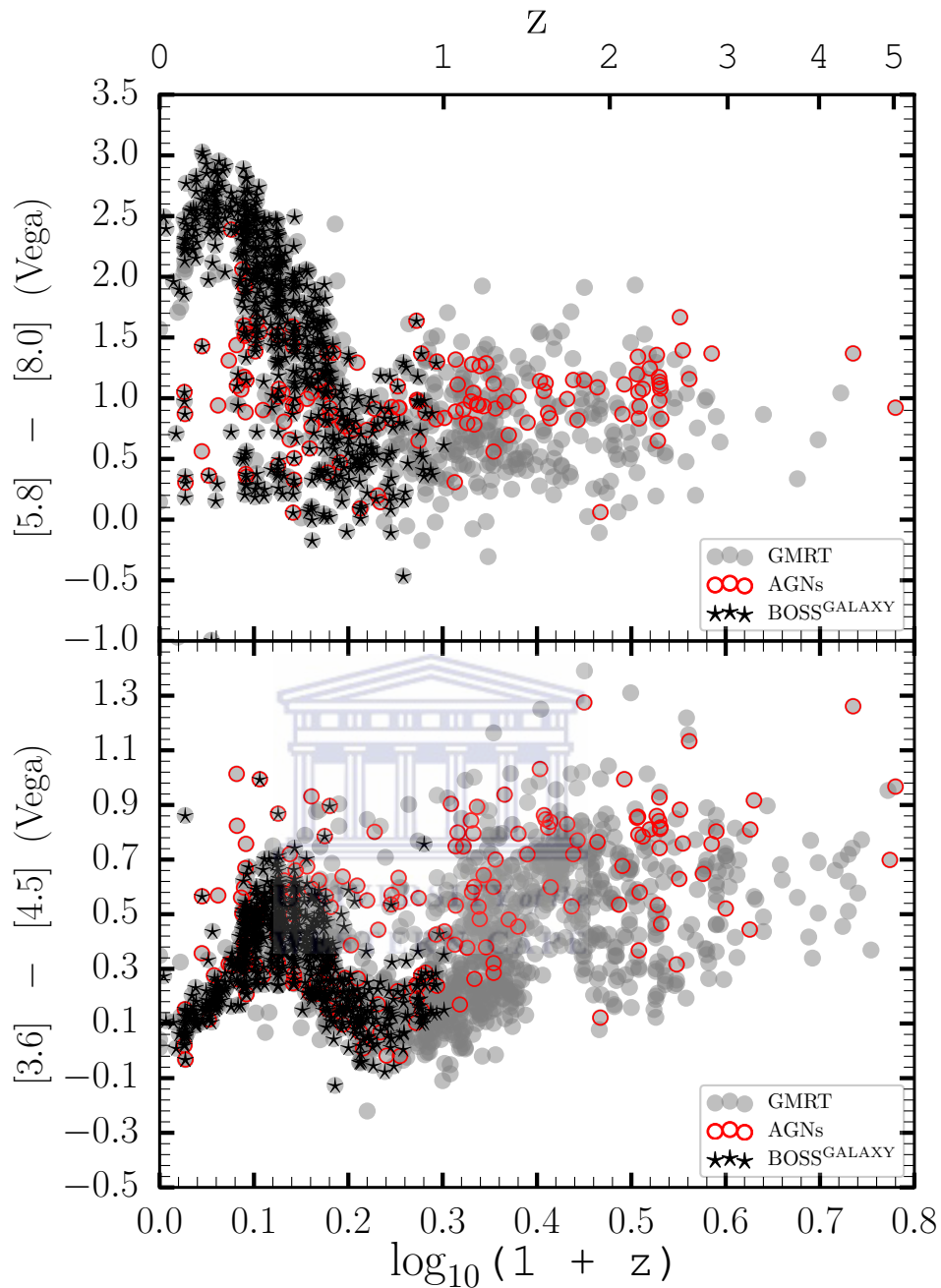


FIGURE 3.8: Color evolution of Mid Infrared (MIR) bands. $[5.8] - [8.0]$ (Vega) (top panel) and $[3.6] - [4.5]$ (Vega) (bottom panel) vs $\log_{10}(1 + z)$. Over-plotted are the various AGN and galaxy classifications from Figure 3.7.

3.7 Mid-Infrared diagnostics (IRAC colors)

With the advent of the Infrared Array Camera (Fazio *et al.*, 2004) on board of the Spitzer (Werner *et al.*, 2004) space telescope it has become possible to obtain MIR photometry for large samples of field galaxies, and thus using MIR SEDs to identify

specific populations of AGNs and star-forming galaxies in four bands at 3.6, 4.5, 5.8, and 8.0 μm . The MIR continuum from galaxies arises mostly from three sources:

1. H II regions dominated by emission from very small dust grains (producing a steeply rising continuum at 12-16 μm)
2. Photodissociation regions dominated by bands of polycyclic aromatic hydrocarbon (PAH) emission,
3. AGNs dominated by a strong 3-10 μm continuum.

The spectral energy distributions (SEDs) arising from each of these was shown by [Laurent et al. \(2000\)](#) to be sufficiently distinct to allow discrimination of AGNs from star-forming (SFGs) galaxies based on their MIR SEDs. In AGNs, the peak emission in the MIR is around 20-30 μm that is at shorter wavelength compared to the emission from star heated dust, at few hundreds μm , as the AGN radiation is so intense that heats the dust grains up to their sublimation temperature of $T_{dust} \sim 1000 - 1500 \text{ K}$. If the AGN is sufficiently luminous compared to its host galaxy, the superposition of the blackbody emission from the AGN-heated dust will fill in the dip in the galaxy's SED and produce a red power-law-like thermal continuum across the IRAC bands.

The IRAC color-color cuts most commonly adopted for AGN selection were defined by ([Lacy et al., 2004, 2007](#)) and [Stern et al. \(2005\)](#) using shallow IRAC data to which additional flux cuts at 8 μm , 24 μm , or R band served to reject all but the brightest sources ($S_{8\mu\text{m}} \geq 1 \text{ mJy}$, [Lacy et al. \(2004\)](#); $R < 21.5$ and $S_{8\mu\text{m}} \geq 76 \mu\text{Jy}$, [Stern et al. \(2005\)](#); $S_{24\mu\text{m}} \gtrsim 5 \text{ mJy}$, [Lacy et al. \(2007\)](#)). [Lacy et al. \(2004\)](#) used SDSS quasars to provide an empirical localization of the AGN population in the MIR color-color space. These initial color cuts effectively select luminous AGNs in samples containing only AGNs and bright, low-redshift star-forming galaxies (see also [Sajina et al. \(2005\)](#)). In deeper IRAC surveys they extend into regions of IRAC color -color space populated by moderate to high-redshift ($z \gtrsim 0.5$) star-forming galaxies (e.g., [Donley et al. \(2007\)](#); [Yun et al. \(2008\)](#); [Brusa et al. \(2009\)](#); [Richards et al. \(2009\)](#); [Park et al. \(2010\)](#)). From the crossmatch in Section 2.4, we were able to associate 1091, comprising 39%, of our radio sources with the four IRAC channels at 3.6, 4.5, 5.8, and 8.0 μm respectively (see Table 2.1) In this section we study the various cuts for selecting AGNs and compare them to our BOSS/SDSS spectroscopic galaxy classification and also the AGN criteria outlined in Section 3.4 Figure 3.7.

3.7.1 Lacy Wedge

Lacy *et al.* (2004) used the Spitzer Space Telescope First Look Survey (FLS) to assess the fraction of AGNs with mid-infrared (MIR) luminosities that are comparable to quasars and that are missed in optical quasar surveys because of dust obscuration. Figure 3.9 shows the IRAC color-color plot using all four broadband channels of the IRAC instrument presented in Lacy *et al.* (2004).

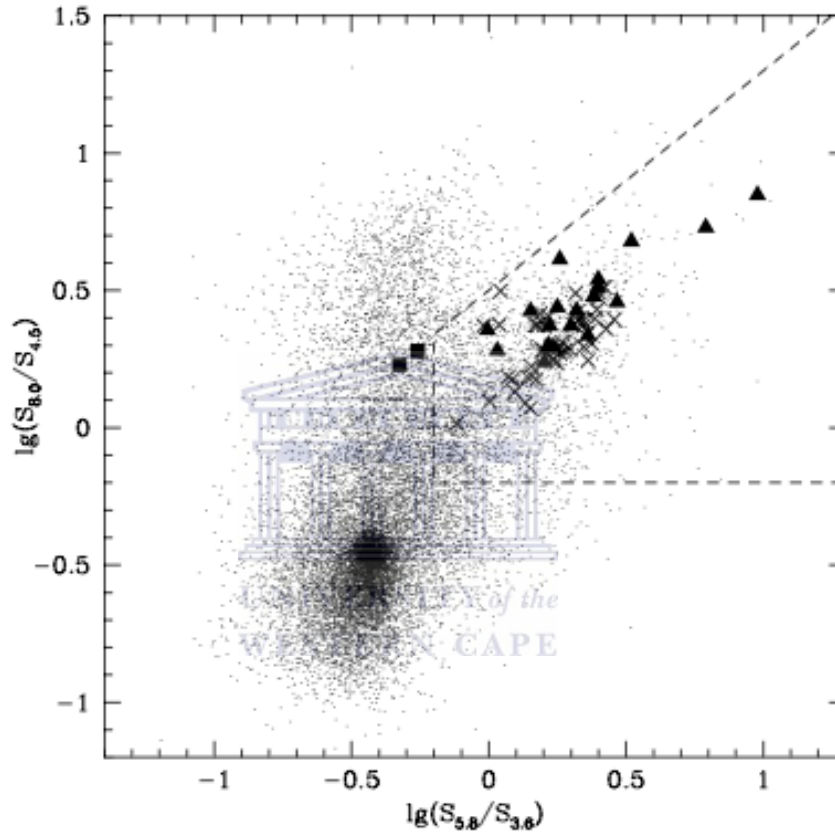


FIGURE 3.9: IRAC color-color plot using the main-field FLS data. The dots represent $\sim 16,000$ objects with "clean" detections in all four IRAC bands. Crosses show the colors of all the SDSS and radio-selected quasars, squares the SDSS Seyfert 1 galaxies, and triangles the bright ($S_{8.0} \geq 1\text{mJy}$) sample of obscured AGNs. The dashed line shows the color criteria used to pick out the AGN sample. Adopted from Lacy *et al.* (2004).

The "Lacy wedge" (Lacy *et al.*, 2004, 2007), selects AGN based on their color relative to starforming galaxies. This selection is given by the following color cuts:

$$\log_{10}(S_{5.8}/S_{3.6}) > -0.1$$

$$\log_{10}(S_{8.0}/S_{4.5}) > -0.2$$

$$\log_{10}(S_{8.0}/S_{4.5}) \leq 0.8 \cdot \log_{10}(S_{5.8}/S_{3.6}) + 0.5$$

The above color cuts produce the wedge-shaped area in the upper right corner of Figure 3.9. This area represents the objects most likely to be AGN accreting at $\sim 10\%$ of the Eddington rate in "cold mode" accretion. Figure 3.10 presents IRAC color-color diagram for our GMRT sample with four IRAC band detections. Over-plotted are the AGN selected as indicated in Section 3.4 by Figure 3.7 as well as the sources classified as star-forming galaxies by the BOSS/SDSS pipeline. Using this AGN wedge selection criterion, we select 438 radio sources constituting 16% of the entire GMRT population. We then compared this method to the 136 AGN sources described in Figure 3.7 of Section 3.5 with detections in the four IRAC channels. We found 103 of the already classified AGNs fall within the Lacy wedge with 33 of them falling outside the wedge. Many of the BOSS/SDSS galaxies falling within this wedge may also be highly-obscured AGN, but cannot be confirmed as such from optical/near-infrared data alone [Lacy et al. \(2013\)](#).

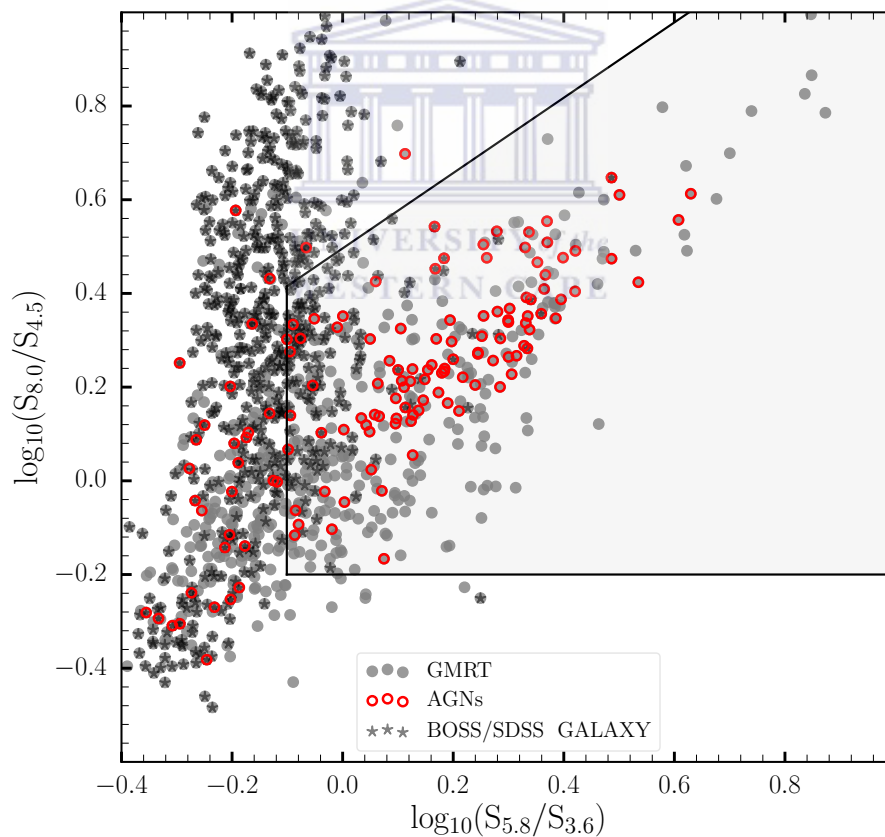


FIGURE 3.10: IRAC color-color diagram for our GMRT sample with four IRAC band detection in [Lacy et al. \(2004\)](#) color space. Over-plotted are AGN selection as indicated by Figure 3.7 and also the BOSS/SDSS spectroscopic pipeline galaxy classification.

3.7.2 Stern Wedge

[Stern et al. \(2005\)](#) reported on the Spitzer Space Telescope mid-infrared colors, derived from the IRAC Shallow Survey, of nearly 10,000 spectroscopically identified sources from the AGN and Galaxy Evolution Survey (AGES). They showed by considering only broad-lined AGNs, that their mid-infrared color criteria identify over 90% of spectroscopically identified quasars and Seyfert 1 galaxies. They applied their color criteria to the full imaging data set, and discussed the implied surface density of AGNs, finding evidence for a large population of optically obscured active galaxies (see [Stern et al. \(2005\)](#)). Figure 3.11 presents an IRAC color-color diagram for the AGES sample, with symbols denoting spectroscopic classification from [Stern et al. \(2005\)](#).

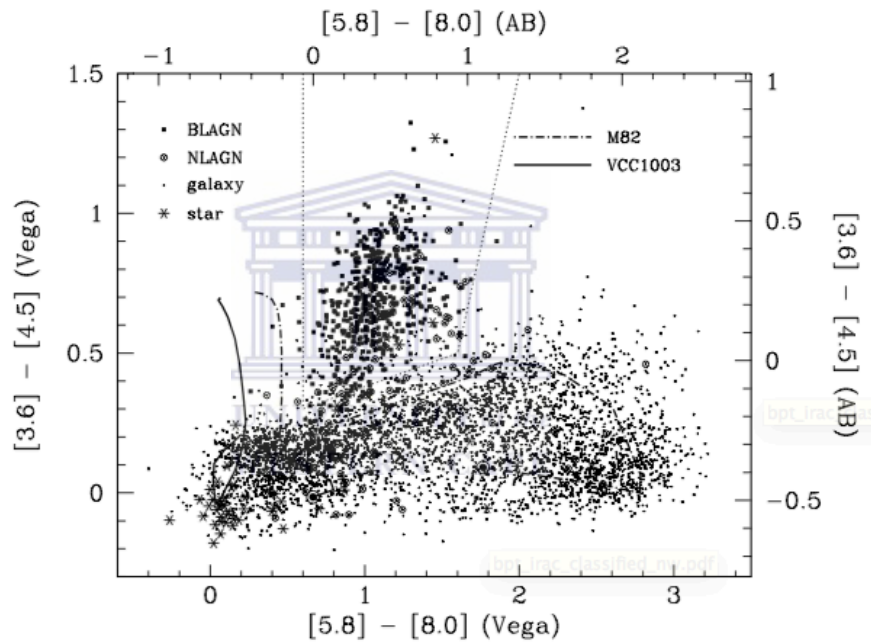


FIGURE 3.11: IRAC colors of spectroscopically identified objects from the AGES survey. Axes indicate both the Vega and AB magnitude systems. The dotted line empirically separates active galaxies from Galactic stars and normal galaxies. Adopted from [Stern et al. \(2005\)](#).

The criteria adopted by [Stern et al. \(2005\)](#):

$$([5.8] - [8.0]) > 0.6 \wedge ([3.6] - [4.5]) > 0.2 \times ([5.8] - [8.0]) + 0.18$$

$$\wedge ([3.6] - [4.5]) > 2.5 \times ([5.8] - [8.0]) - 3.5$$

Figure 3.12 presents [Stern et al. \(2005\)](#) IRAC color-color diagram for our GMRT sample with four IRAC band detection (grey circles). The over-plotted open red circles are AGN as indicated in Section 3.5 by Figure 3.7 and the black stars represent the BOSS/SDSS spectroscopic pipeline galaxy classification. According to this AGN wedge selection

criterion, we select 259 radio sources constituting 9.3% of the entire GMRT population. We then compared this method to the 136 AGN sources described in Figure 3.7 of Section 3.4 with detections in the four IRAC channels. We found 88 of these already classified AGNs fall within the Stern wedge with 48 of them falling outside the wedge.

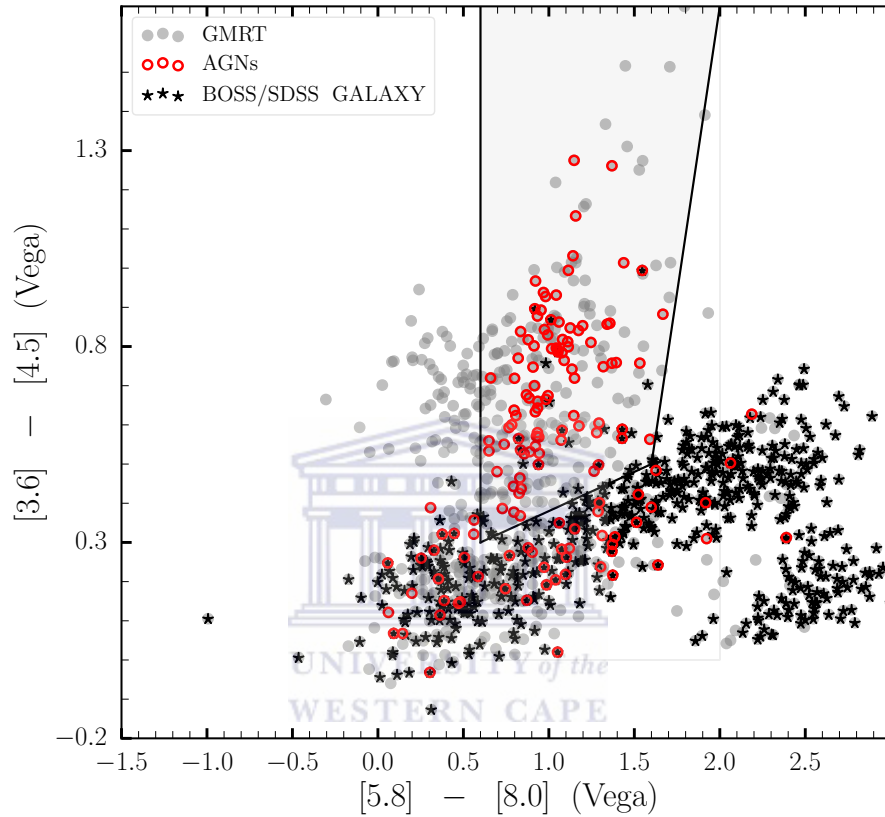


FIGURE 3.12: IRAC color-color diagram for our GMRT sample with four IRAC band detection in [Stern et al. \(2005\)](#) color space. Over-plotted are AGN selection as indicated by Figure 3.7 and also the BOSS/SDSS spectroscopic pipeline galaxy classification.

3.7.3 Donley Wedge (The Revised IRAC Selection Criteria)

[Donley et al. \(2012\)](#), minimised the contamination from both low and high redshift SFG by using the large samples of luminous AGNs and high redshift star-forming galaxies in Cosmic Evolution Survey (COSMOS) by redefining the AGN selection criteria in deep IRAC surveys. [Donley et al. \(2012\)](#) imposed the flux density to monotonically increase in the IRAC bands and the colours to be such that the sources lies in the wedge defined below. The completeness of AGN selection method is strongly dependent on AGN luminosity being high for $L_{2-10keV} \geq 10^{44} \text{erg s}^{-1}$ but relatively low ($< 20\%$) at lower luminosities (see [Donley et al. \(2012\)](#)). Seyfert 2 galaxies, are also easily missed by this selection criteria. The final revised AGN selection criteria are as follows, where

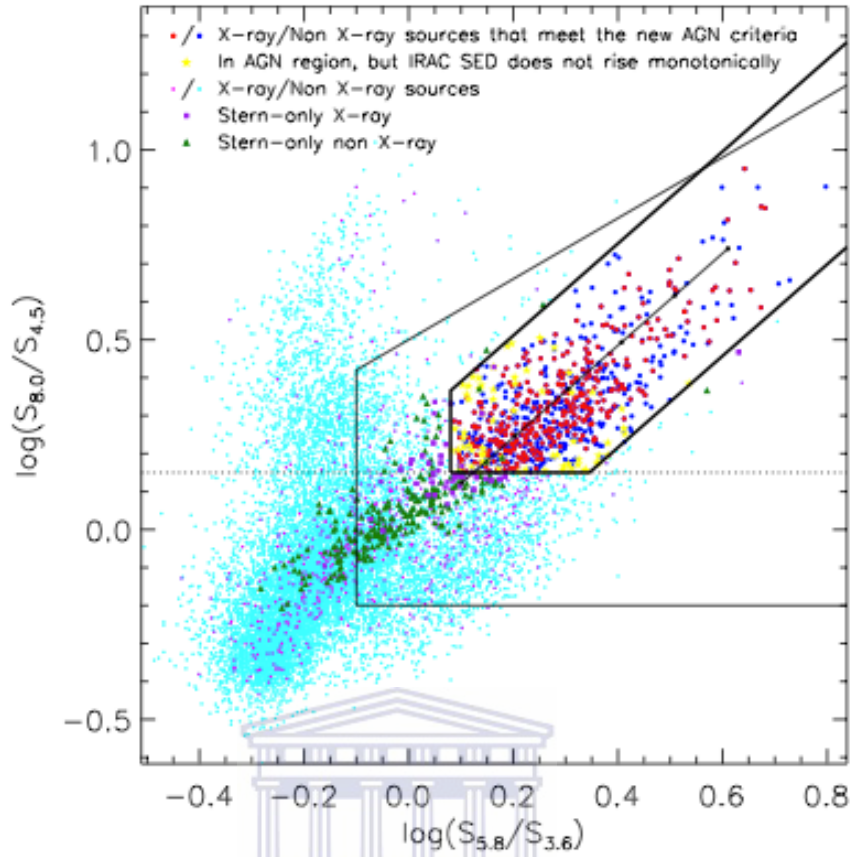


FIGURE 3.13: New AGN selection criteria (thick solid lines). The full IRAC-COSMOS sample with $T_x \geq 50$ ks are plotted as small points, and sources that meet our new criteria are shown by large filled circles. Adopted from [Donley *et al.* \(2012\)](#).

\wedge is the logical "AND" operator.

$$x = \log_{10} \left(\frac{f_{5.8\mu\text{m}}}{f_{3.6\mu\text{m}}} \right), \quad y = \log_{10} \left(\frac{f_{8.0\mu\text{m}}}{f_{4.5\mu\text{m}}} \right) \quad (3.6)$$

$$x \geq 0.08 \wedge y \geq 0.15 \wedge y \geq (1.21 \times x) - 0.27 \wedge y \leq (1.21 \times x) + 0.27 \\ \wedge f_{4.5\mu\text{m}} > f_{3.6\mu\text{m}} > f_{4.5\mu\text{m}} \wedge f_{8.0\mu\text{m}} > f_{5.8\mu\text{m}} \quad (3.7)$$

The criteria defined above have been designed to reject the majority of low - and high redshift star-forming contaminants still included in the [Lacy *et al.* \(2004, 2007\)](#) and [Stern *et al.* \(2005\)](#) AGN selection wedges. Figure 3.13 shows IRAC colors of the sources that meet these criteria. While all AGN candidates, described in [Donley *et al.* \(2012\)](#), fall by definition within the original [Lacy *et al.* \(2004, 2007\)](#) AGN selection wedge, 9% have IRAC SEDs that do not rise monotonically, but that decrease between 3.6 and 4.5 μm or 5.8 and 8.0 μm (or, in rare cases, between 4.5 and 5.8 μm), placing them on the

outskirts of the [Stern *et al.* \(2005\)](#) AGN selection region (of these, 38% formally fall outside of the [Stern *et al.* \(2005\)](#)).

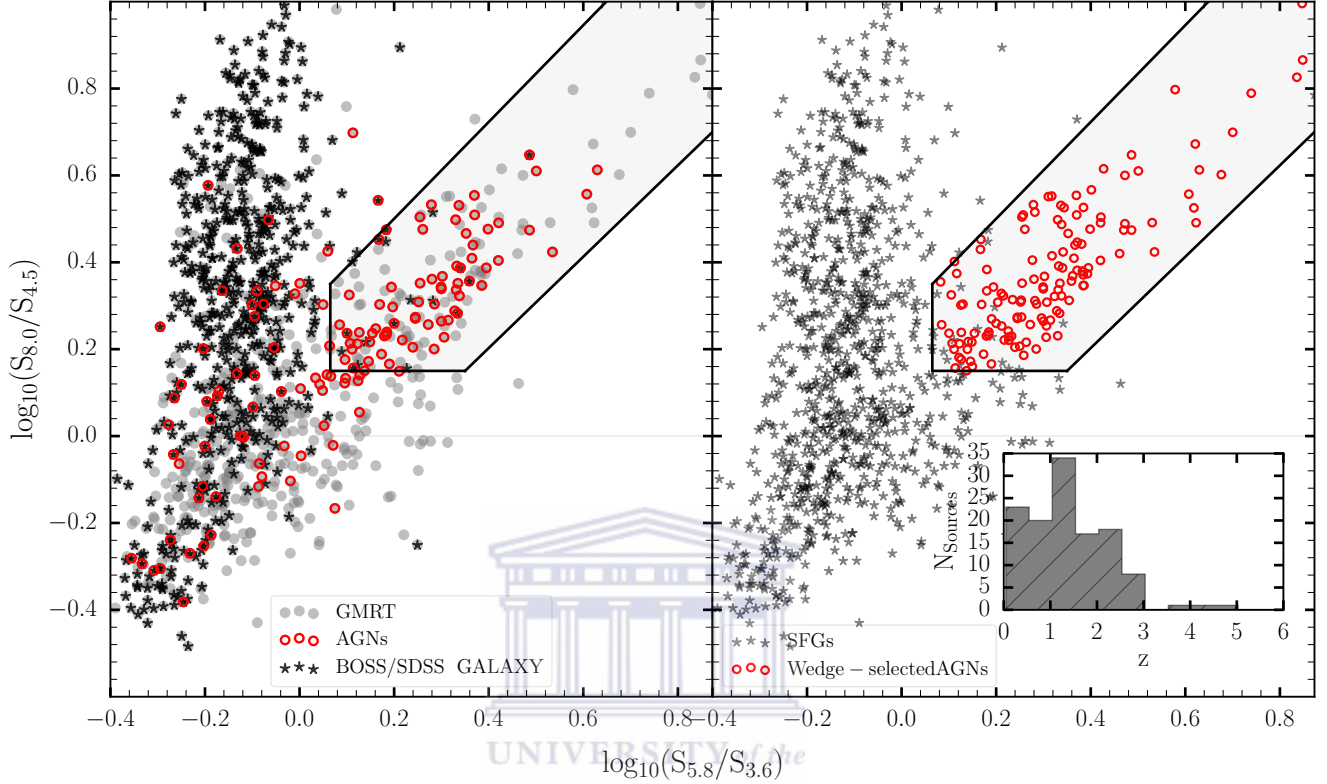


FIGURE 3.14: IRAC color-color diagram for our GMRT sample with four IRAC band detection in [Donley *et al.* \(2012\)](#) color space. Left panel: Over-plotted are AGN selection as indicated by Figure 3.7. Right panel: IRAC color-color diagram showing the separation between AGNs and star-forming galaxies (SFGs). The inset histogram shows the redshift distribution of the sources classified as AGNs according to the Donley wedge.

We also studied this method of MIR AGN selection by applying it to our GMRT data. Figure 3.14 presents IRAC color-color diagram for our GMRT sample with four IRAC band detection in [Donley *et al.* \(2012\)](#) color-color space. The left panel shows the AGN selected as indicated by Figure 3.7. The right panel is the same as the left panel but the SFG/AGN classification purely follows [Donley *et al.* \(2012\)](#). The inset histogram shows the redshift distribution of the sources classified as AGNs according to the Donley wedge. From the left panel, 66 of the AGN sources described in Section 3.5 reside within the Donley wedge with 70 sources residing outside out of the total of 136 AGNs (see Section 3.5) with the four IRAC band detections. We see that only a few sources (< 20) of the BOSS/SDSS spectroscopic pipeline galaxy classification fall within this wedge. On the right panel, we see that a few of the SFGs symbols (black stars) fall within the wedge but are not classified as AGNs by the criteria given in Equation 3.7. This is due to

the monotonically increasing flux density criterion (see Equation 3.7). Therefore, we find the Donley selection to be the most reliable (but perhaps less complete) discriminator between AGNs and SFGs as compared to the selection in Section 3.5.

However, every technique for selecting AGNs is affected by selection biases, and these ones are no exception. The color selection means that objects whose observed mid-infrared colours are not dominated by thermal emission from AGN will be missing from the sample. These effects can happen in a number of ways. First, the AGN may have such low luminosity in the infrared that the starlight from the host galaxy dominates the mid-infrared emission. This results from either the AGN being intrinsically weak or because the covering factor of the hot dust is low, perhaps because of an unusual torus geometry. Increasing redshift worsens this bias as the stellar bump in the rest-frame near-infrared is redshifted into the mid-infrared bands, and the k -correction on the thermal emission of the dust becomes large. Also, some AGNs will simply be so highly obscured that the AGN emission is not seen at observable wavelengths $< 8\mu\text{m}$. Another contributing factor could be AGN being so highly obscured that they drop out of the IRAC catalogs at short wavelengths (Lacy *et al.*, 2006). Table 3.4 shows the total number of AGNs from various selection criteria according to the MIR classifications

TABLE 3.4: Total number of AGNs from various selection criteria according to the MIR classifications.

Category	AGNs	AGNs ^{redshift}	AGNs ^{redshift}	Fraction (%)
Lacy	438	379		21.5%
Stern	259	223		12.7%
Donley	138	123		7%

^a Wedge selected AGNs according to Lacy *et al.* (2004) color space.

^b Wedge selected AGNs according to Stern *et al.* (2005) color space.

^c Wedge selected AGNs according to Donley *et al.* (2012) color space.

^d AGNs^{redshift} - Number of wedge selected AGNs with redshift.

3.7.4 Radio-quiet AGN selection

The SFG locus is the region of $\pm 2\sigma$ centred on the M82 template (see Figure 3.6), sources below this locus display a radio excess (see Bonzini *et al.* (2013)) and therefore do not follow the FIR - radio correlation. These sources are classified as RL AGNs. Above this threshold, a source is classified as a RQ AGN if it shows clear evidence for an AGN in the X-ray (see Section 3.2.2) or in the MIR bands. The "Lacy wedge" is heavily contaminated by high redshift SFGs (Donley *et al.*, 2012). Therefore, to select AGNs we adopt the stricter criteria described in Donley *et al.* (2012) that are designed

to minimize the contamination from both low and high redshift SFG. Figure 3.15 shows $q_{24\mu\text{m}}$ vs $\log_{10}(1+z)$ for the GMRT sources with MIPS $24\mu\text{m}$ with redshift detections where the left panel shows the over-plotted are X-ray and Donley *et al.* (2012) selected AGNs (open red circles) and the right panel shows the RQ AGN classification from the combination of X-ray and Donley *et al.* (2012) selected AGNs after interpolation to remove sources falling below the -2σ dispersion (dashed lines). A tight MIR (as well as far- and total-IR) radio correlation is expected for SFGs, whereas RL AGNs are expected to strongly deviate from it (e.g., Condon (1992a); Bell (2003); Appleton *et al.* (2004)).

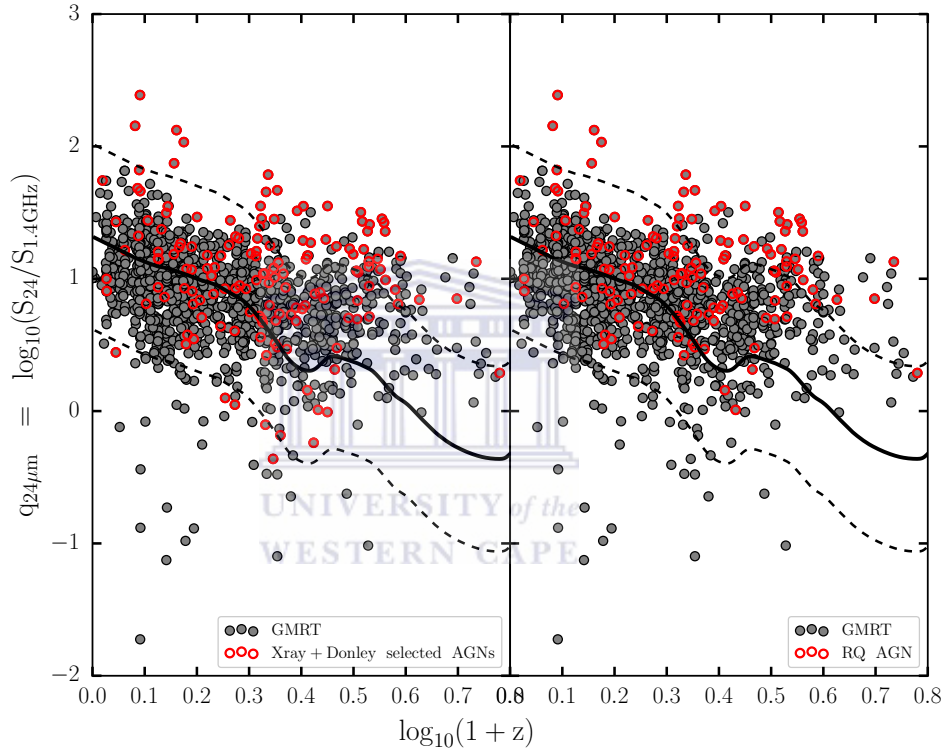


FIGURE 3.15: $q_{24\mu\text{m}}$ vs $\log_{10}(1+z)$ for the GMRT sources with MIPS $24\mu\text{m}$ with redshift detections. Left panel: over-plotted are X-ray and Donley *et al.* (2012) selected AGNs (open red circles). Right panel: RQ AGN classification from the combination of X-ray and Donley *et al.* (2012) selected AGNs after interpolation to remove sources falling below the -2σ dispersion (dashed lines).

The distribution of the $q_{24\mu\text{m}}$ -parameter for SFG and AGN galaxies is shown in Figure 3.16. The mean q -value for RL AGN is -0.4 and that of RQ AGN is 1.04 . On the other hand, the mean q -value for all the AGNs (i.e. RL AGN + RQ AGN) is 0.96 , which is significantly higher than that of the SFGs which is 1.0 .

Figure 3.17 presents $q_{24\mu\text{m}}$ as a function of redshift for RL AGN (open red circles), RQ AGN (open red squares), and SFG (black stars). The solid line show the evolution of

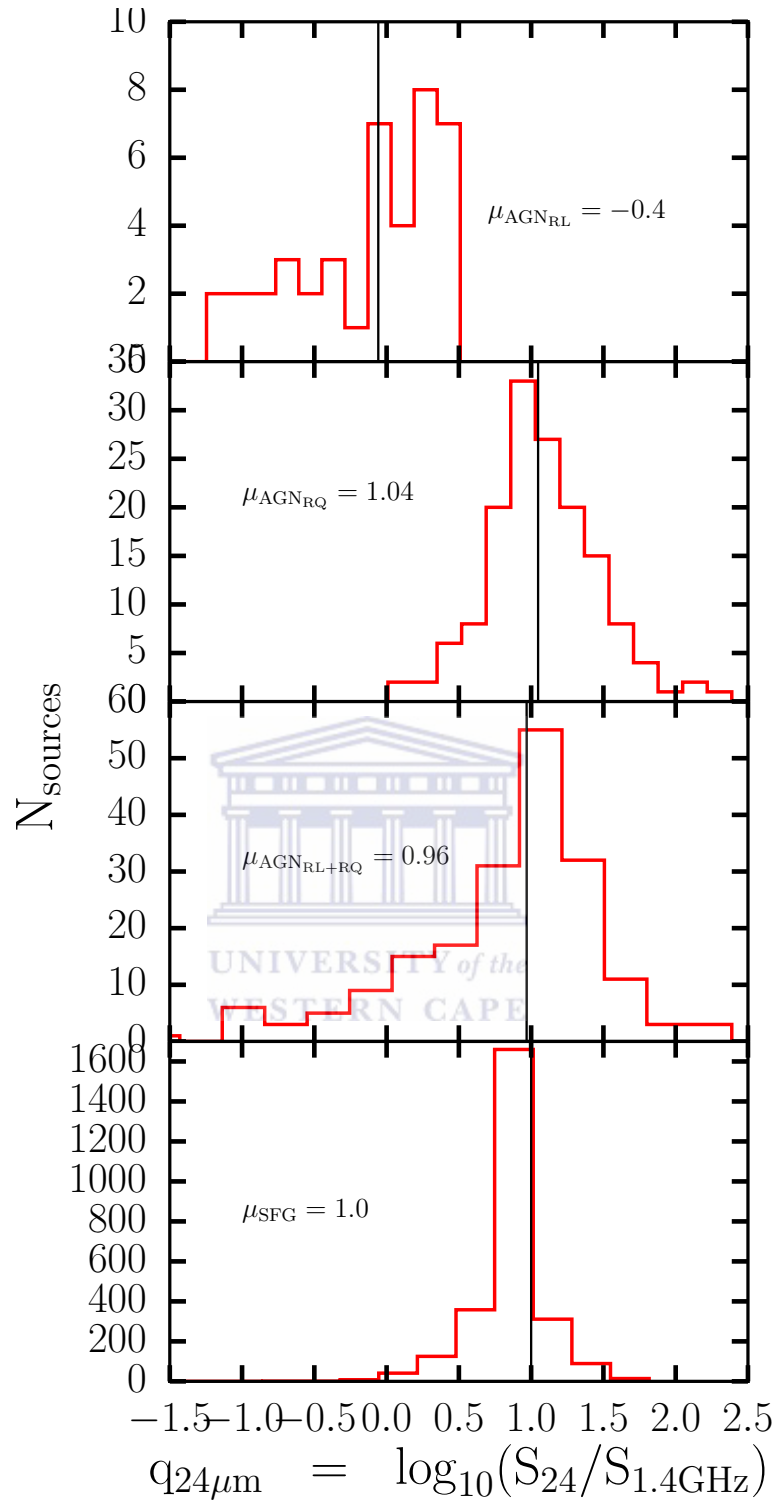


FIGURE 3.16: Distribution of the $q_{24\mu\text{m}}$ parameter for RL AGN (1st panel), RQ AGN (2nd panel) and RQ AGN+RL AGN (3rd panel) and SFG (4th panel) galaxies. The solid vertical line in each panel designates the mean value of the entire distribution.

$q_{24\mu\text{m}}$ for the M82 template as a function of redshift with $\pm 2\sigma$ dispersion (dashed lines).

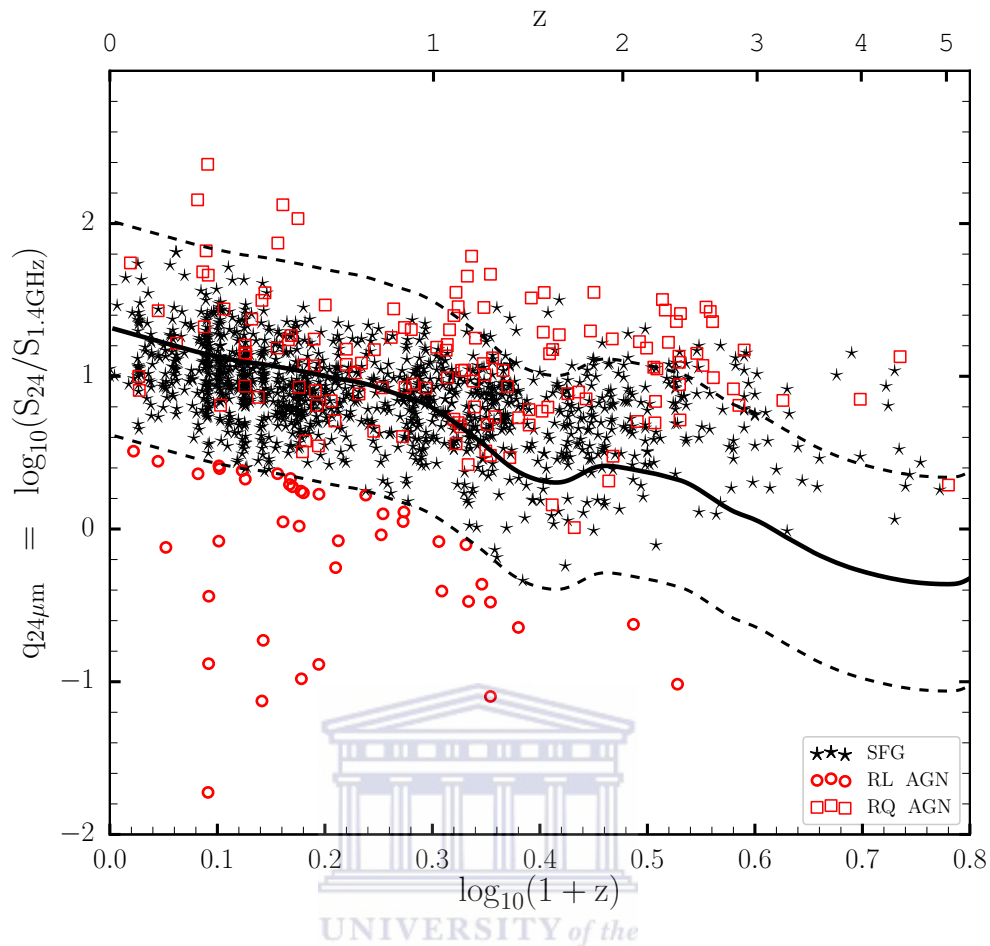


FIGURE 3.17: $q_{24\mu\text{m}}$ as a function of redshift for RL AGN (open red circles), RQ AGN (open red squares), and SFG (black stars). The solid line show the evolution of $q_{24\mu\text{m}}$ for the M82 template as a function of redshift with $\pm 2\sigma$ dispersion (dashed lines).

3.7.5 IRAC1234 & MIPS-24 detected sample

In this section compute separate AGN/SFG statistics for a smaller (and brighter) IRAC1234 & MIPS-24 detected sample. This would provide us a more homogeneous (if brighter and less complete) AGN classification. Combining IRAC1234 & MIPS-24 detected sample gives a total of 1009 sources within which 952 sources have redshift associations. Table 3.5 presents the breakdown of AGN selection from a subsample of IRAC1234 & MIPS-24 detected sample.

TABLE 3.5: Table showing the breakdown of AGN selection from a subsample of IRAC1234 & MIPS-24 detected sample. Note that the fractions have been computed with respect to the redshift population of our sources.

Category	AGNs	Fraction (%)
IRAC1234 & MIPS-24	952	54%
IRAC1234 & MIPS-24 ^{Donley}	194	11%
IRAC1234 & MIPS-24 ^{BOSS}	81	4.6%
IRAC1234 & MIPS-24 ^{Xray}	60	3.4%
IRAC1234 & MIPS-24 ^{Radio luminosity}	11	0.6%
IRAC1234 & MIPS-24 ^{RL AGN} (Bonziniet al., 2013)	27	1.5%
IRAC1234 & MIPS-24 ^{RQ AGN} Bonziniet al. (2013)	135	7.7%

^a IRAC1234 & MIPS-24 - IRAC1234 & MIPS-24 detected sample

^b IRAC1234 & MIPS-24^{Donley} - IRAC1234 & MIPS-24 detected sample with Donley *et al.* (2012) AGN detections.

^c IRAC1234 & MIPS-24^{BOSS} - IRAC1234 & MIPS-24 detected sample with BOSS AGN detections.

^d IRAC1234 & MIPS-24^{Xray} - IRAC1234 & MIPS-24 detected sample with Xray detections.

^e IRAC1234 & MIPS-24^{Radio luminosity} - IRAC1234 & MIPS-24 detected sample with radio-loud selection of AGNs according to their radio luminosity (see Jiang *et al.* (2007)).

^f IRAC1234 & MIPS-24^{RL AGN} - IRAC1234 & MIPS-24 detected sample with RL AGN (Bonzini *et al.*, 2013) detections.

^g IRAC1234 & MIPS-24^{RQ AGN} - IRAC1234 & MIPS-24 detected sample with RQ AGN (Bonzini *et al.*, 2013) detections.

3.8 AGN optical line diagnostics

3.8.1 Four-line diagnostics

Baldwin, Philips, Terlevich (hereafter BPT) (Baldwin *et al.*, 1981) showed that it was possible to tell the difference between Type 2 AGNs (see Chapter 1 Section 1.1.1) from normal star-forming galaxies by considering the intensity ratios of relatively strong emission lines. The approach was refined by Veilleux and Osterbrock (1987) and has become standard technique to classify objects according to where they reside on the BPT diagrams. These diagrams are based on the four optical line ratios ; [O III]/H β , [N II]/H α , [S II]/H α and [O I]/H α . This classification scheme depends on the excitation mechanism of the nebular emission lines in galaxies. The most commonly used BPT diagnostics are; [N II]6584/H α vs [O III]5007/H β (BPT-NII), [O I]6300/H α vs [O III]5007/H β (BPT-OI) and [S II]6717, 6731/H α vs [O III]5007/H β (BPT-SII).

Kewley *et al.* (2001) presented models used to derive a new theoretical classification scheme for starbursts and AGN based on the optical diagnostic diagrams. These models were built up on Dopita *et al.* (2000), who theoretically recalibrated the extragalactic

H II region sequence using these line diagnostic diagrams and others, in order to differentiate and quantify the effects of abundance, ionization parameter, and continuous versus instantaneous burst models. [Kewley *et al.* \(2001\)](#) used theoretical upper limits for starburst galaxies to classify the galaxies with an "extreme" mixing line produced using their shock modeling to classify galaxies into starburst, LINER, and AGN types as shown in [Figure 3.18](#).

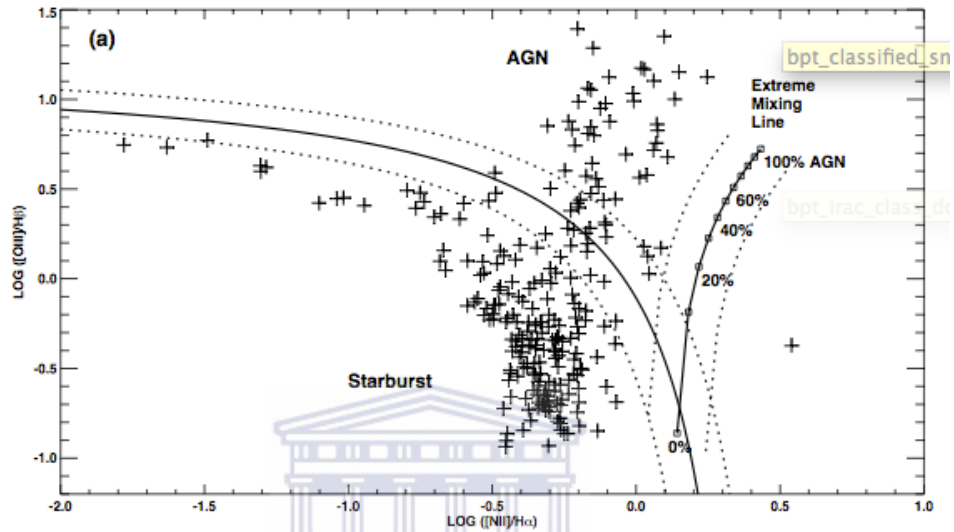


FIGURE 3.18: Diagnostic diagram showing the galaxies in the sample studied by [Kewley *et al.* \(2001\)](#). The theoretical classification line and extreme mixing line are shown by thick lines, and dashed lines represent ± 0.1 dex of these lines, indicating the error range of their modeling. Adopted from [Kewley *et al.* \(2001\)](#).

[Kauffmann *et al.* \(2003\)](#) examined the properties of the host galaxies of 22 623 narrow-line AGN with $0.02 < z < 0.3$ selected from a complete sample of 122 808 galaxies from the SDSS survey and based on their data, revised the demarcations between starburst and AGN. [Figure 3.19](#) shows of the BPT-N II diagram for all the emission line galaxies studied by [Kauffmann *et al.* \(2003\)](#)

The demarcations used to separate starburst from AGN are summarised by [Kewley *et al.* \(2006\)](#) for each diagram as follows:

1) BPT-NII:

- $\log_{10}([\text{OIII}]/\text{H}\beta) = 0.61/(\log_{10}([\text{NII}]/\text{H}\alpha) - 0.05) + 1.3$ ([Kauffmann *et al.* \(2003\)](#) line)
- $\log_{10}([\text{OIII}]/\text{H}\beta) = 0.61/(\log_{10}([\text{NII}]/\text{H}\alpha) - 0.47) + 1.19$ ([Kewley *et al.* \(2001\)](#) line)

2) BPT-SII:

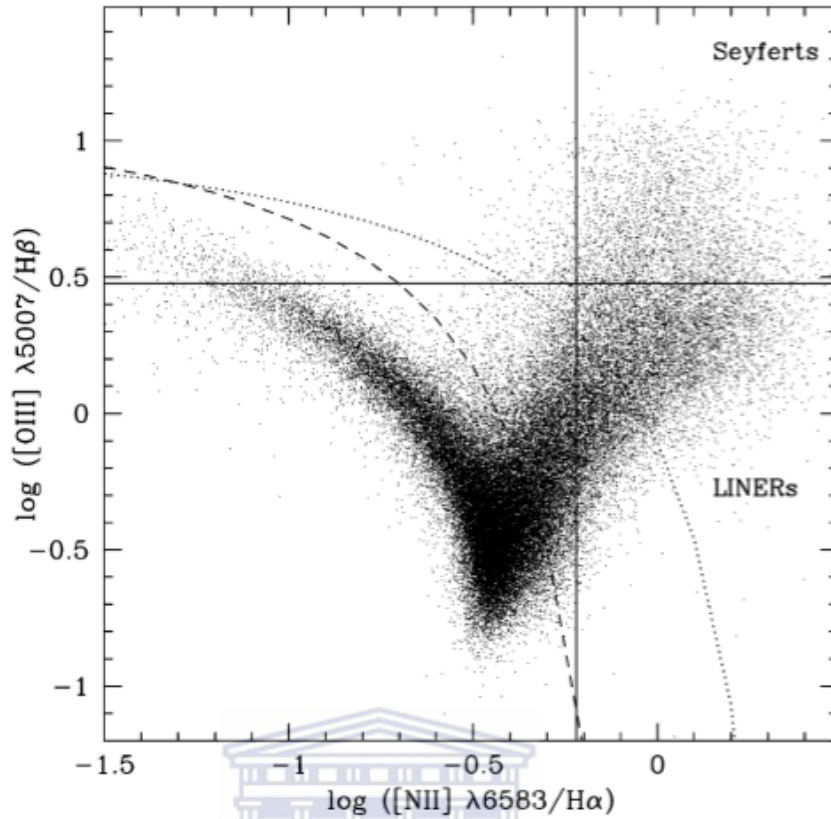


FIGURE 3.19: The BPT diagram, the dotted line represents the theoretical division between AGN and star-forming galaxies (SFGs) (Kewley *et al.*, 2001) while the dashed line is an empirical determination of this separation (Kauffmann *et al.*, 2003). Adopted from Kauffmann *et al.* (2003)

- $\log_{10}([\text{OIII}]/\text{H}\beta) = 0.72/(\log_{10}([\text{SII}]/\text{H}\alpha) - 0.32) + 1.3$ (main AGN line)
- $\log_{10}([\text{OIII}]/\text{H}\beta) = 1.89 \log_{10}([\text{SII}]/\text{H}\alpha) + 0.76$ (LINER/Sy2 line)

3) BPT-OI:

- $\log_{10}([\text{OIII}]/\text{H}\beta) = 0.73/(\log_{10}([\text{OI}]/\text{H}\alpha) + 0.59) + 1.33$ (main AGN line)
- $\log_{10}([\text{OIII}]/\text{H}\beta) = 1.89 \log_{10}([\text{OI}]/\text{H}\alpha) + 1.3$ (LINER/Sy2 line)

Figure 3.20 (a) presents the $[\text{NII}]/\text{H}\alpha$ versus $[\text{O III}]/\text{H}\beta$ standard optical diagnostic diagram from Kewley *et al.* (2006). The Kewley *et al.* (2001) and Kauffmann *et al.* (2003) classification lines are shown as the solid red and dashed lines. Galaxies that lie below the dashed Kauffmann *et al.* (2003) line are classed as H II-region-like galaxies.

Kewley *et al.* (2006) noticed that star-forming galaxies form a tight sequence going from low metallicities (low $[\text{NII}]/\text{H}\alpha$, high $[\text{O III}]/\text{H}\beta$) end the to high metallicities (high

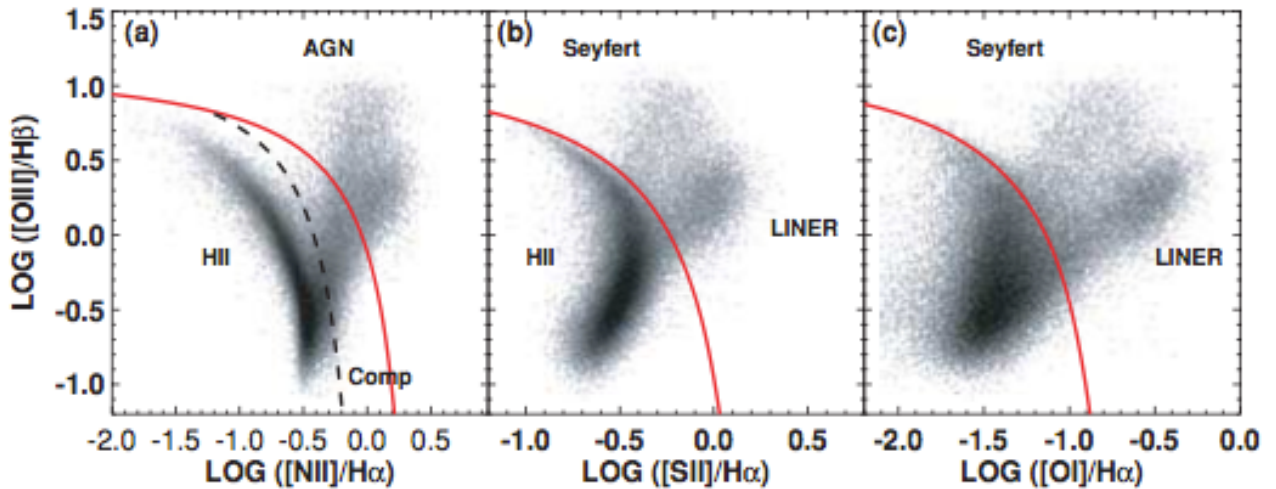


FIGURE 3.20: (a) The BPT $[\text{NII}]/\text{H}\alpha$ versus $[\text{O III}]/\text{H}\beta$ diagnostic diagram for SDSS galaxies with $S/N > 3$ in all lines. The Kewley *et al.* (2001) extreme starburst line and the Kauffmann *et al.* (2003) classification line are shown as the solid and dashed lines, respectively. (b) The BPT $[\text{S II}]/\text{H}\alpha$ versus $[\text{O III}]/\text{H}\beta$ diagnostic diagram; (c) The BPT $[\text{O I}]/\text{H}\alpha$ versus $[\text{O III}]/\text{H}\beta$ diagnostic diagram. Adopted from Kewley *et al.* (2006)

$[\text{NII}]/\text{H}\alpha$, low $[\text{O III}]/\text{H}\beta$) and referred to this as the "star-forming sequence". The AGN mixing sequence begins at the high-metallicity end of the star-forming sequence and extends towards high $[\text{NII}]/\text{H}\alpha$ and high $[\text{O III}]/\text{H}\beta$ values. Normally, galaxies that lie in between the two classification lines are on the AGN-H II mixing sequence and are classified as composites. These composite galaxies are likely to contain a metal-rich stellar population plus an AGN. Galaxies that lie above the Kauffmann *et al.* (2003) line are classified as AGN. Figure 3.20 (b) and (c) show the $[\text{O III}]/\text{H}\beta$ versus $[\text{S II}]/\text{H}\alpha$ and $[\text{O III}]/\text{H}\beta$ versus $[\text{O I}]/\text{H}\alpha$ diagrams for the SDSS sample used in Kewley *et al.* (2006). The Kewley *et al.* (2001) classification line provides an upper bound to the star-forming sequence on these diagrams.

The BPT diagram is limited to $z \leq 0.5$, the redshift at which $[\text{NII}]\lambda 6584$ leaves the optical spectrum window. A number of groups have tried to extend optical emission line diagnostics to higher redshifts by only using lines at the blue end of the spectrum. Lamareille (2010) replaced $[\text{N II}]/\text{H}\alpha$ with $[\text{O II}]\lambda 3726 + \lambda 3729/\text{H}\beta$, creating the "blue diagram", which can be used to classify galaxies out to $z < 0.9$ (see also Tresse *et al.* (1996); Rola *et al.* (1997); Lamareille *et al.* (2004)). In Figure 3.21, we establish that redshift for the GMRT sources with the corresponding four line detections is $z \approx 0.6$ and therefore our BPT diagram is valid.

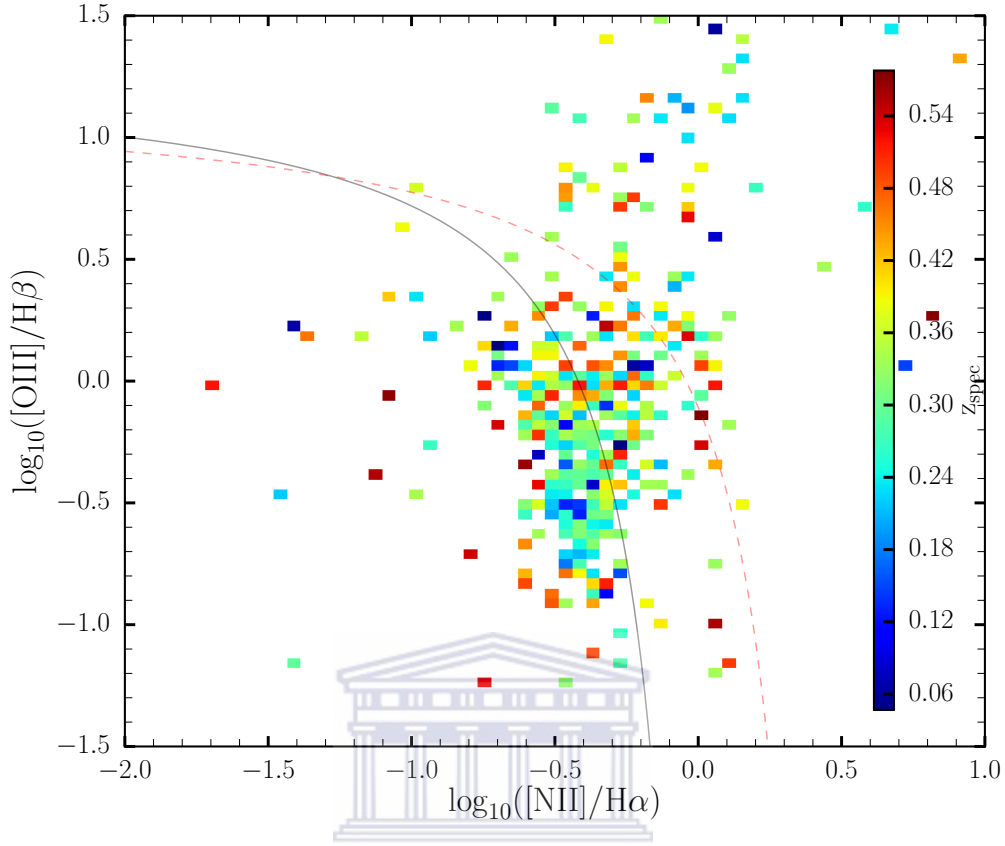


FIGURE 3.21: BPT diagram (color coded according to their spectroscopic redshifts) - $\log_{10}([\text{NII}]/\text{H}\alpha)$ vs $\log_{10}([\text{OIII}]/\text{H}\beta)$ for the GMRT sources that have $[\text{OIII}]$, $\text{H}\beta$, $[\text{NII}]$, $\text{H}\alpha$ detections. The solid black curve shows the [Kauffmann *et al.* \(2003\)](#) empirical division between star-forming galaxies and AGNs. The dashed red curve shows the [Kewley *et al.* \(2001\)](#) theoretical division.

Figure 3.22 shows the BPT diagram (based on flux ratios of the specified lines) applied to the SDSS sample studied by [Trouille *et al.* \(2011\)](#). The dotted curve indicates the [Kewley *et al.* \(2001\)](#) theoretical division and the dashed curve indicates the [Kauffmann *et al.* \(2003\)](#) empirical division between AGNs and star-forming galaxies. In this plot the SDSS data is represented using a combination of a two-dimensional histogram and plotted points. The data is represented as a histogram where more than four data points fall in an individual pixel (the size of the pixel is determined by dividing the plot into 150×150 bins) and plot it as individual points otherwise. The histograms have been square root scaled for better visibility. Each step in contour level represents 20% fewer sources.

We employ the same demarcations that are commonly used to identifying AGN-dominated galaxies versus star-forming dominated galaxies.

- [Kewley *et al.* \(2001\)](#) theoretical division between galaxies having extreme ultra

violet (EUV) ionising radiation field dominated by an AGN ($\geq 50\%$) and those dominated by star formation.

- [Kauffmann *et al.* \(2003\)](#) empirical division based on the location of the SDSS [York *et al.* \(2000\)](#) star-forming galaxies.

BPT-NII separates galaxies whose signal is dominated by star formation (BPT-SF) from galaxies those dominated by AGN activity (BPT-AGN). An AGN will generally have a higher ratio of $[\text{NII}]\lambda 6584$ than a galaxy whose highest energy photons are limited to those that can be produced by massive stars.

We use the BPT-NII diagram to classify galaxies as BPT-SF (galaxies residing in the BPT region dominated by star forming galaxies), BPT-Comp (galaxies residing between the two curves) and BPT-AGN (galaxies residing in the region above the [Kewley *et al.* \(2001\)](#) line).

In all, 697 of the GMRT sources have $[\text{O III}]$ detections, 582 have $[\text{N II}]$ detections, 657 have $\text{H}\beta$ detections and 582 have $\text{H}\alpha$ detections. We classify pure star-forming galaxies as those that lie below the [Kauffmann *et al.* \(2003\)](#) line on the $[\text{N II}]/\text{H}\alpha$ versus $[\text{O III}]/\text{H}\beta$ diagnostic diagram. Composite galaxies lie above the [Kauffmann *et al.* \(2003\)](#) line and below the [Kewley *et al.* \(2001\)](#) line following [Trouille *et al.* \(2011\)](#). The optical spectra of composites can be due to either (1) a combination of star formation and a Seyfert nucleus, or (2) a combination of star formation and LINER emission ([Kewley *et al.*, 2006](#)). The narrow line emission from galaxies lying above the [Kewley *et al.* \(2001\)](#) line is likely to be dominated by an AGN.

Figure 3.23 presents the BPT diagram for the GMRT sources that have $[\text{OIII}]$, $\text{H}\beta$, $[\text{NII}]$, $\text{H}\alpha$ detections where the black stars represents the BPT-SF classification, blue clubsuits represents BPT-Comp (dominated by seyferts/star-forming galaxies.) upon using the [Kauffmann *et al.* \(2003\)](#) and the [Kewley *et al.* \(2001\)](#) divisions.

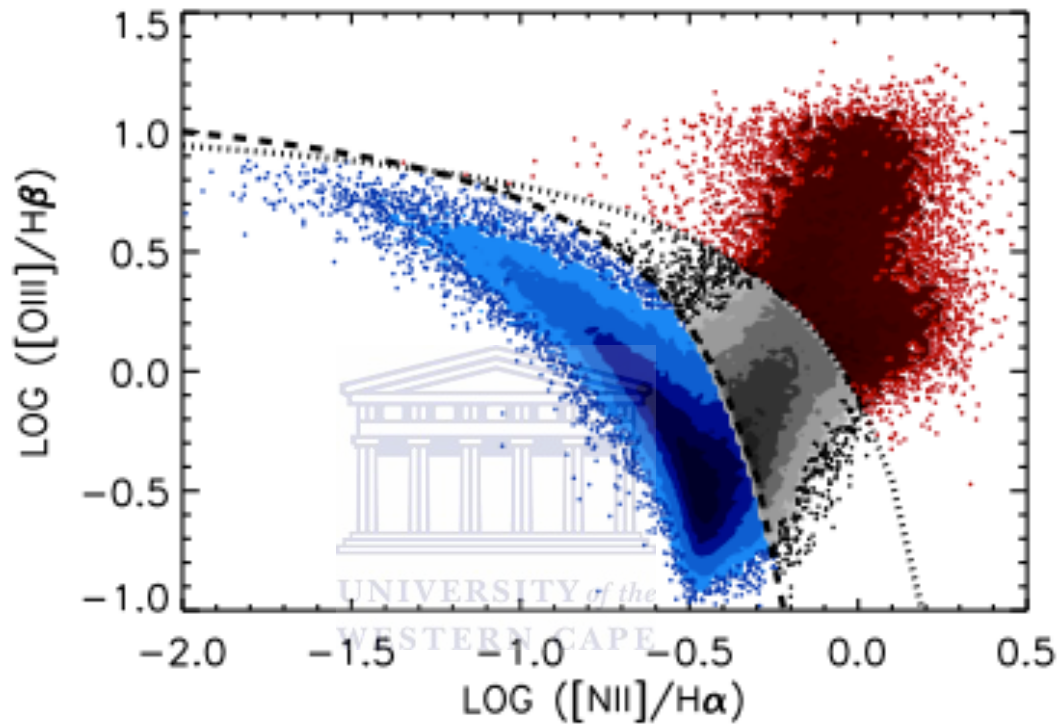


FIGURE 3.22: BPT diagram $\log([\text{N II}]/\text{H}\alpha)$ vs. $\log([\text{O III}]/\text{H}\beta)$ for the SDSS galaxies that have $[\text{O III}]$, $\text{H}\beta$, $[\text{N II}]$, and $\text{H}\alpha$ with $\text{SNR} > 5$. The dashed curve shows the [Kauffmann *et al.* \(2003\)](#) empirical division between star-forming galaxies and AGNs. The dotted curve shows the [Kewley *et al.* \(2001\)](#) theoretical division. As discussed in the text, the SDSS data is represented using a combination of a two-dimensional histogram and plotted points. BPT-SF are shown in blue, BPT-comp in gray, and BPT-AGN in red. Adopted from [Troille *et al.*, 2011](#)

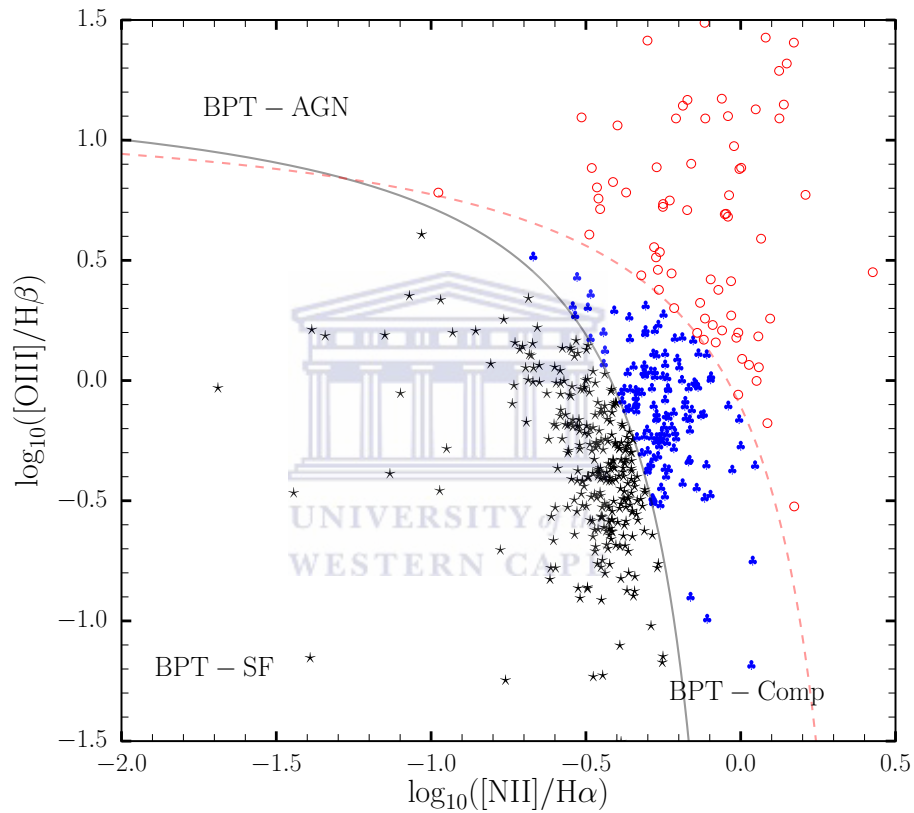


FIGURE 3.23: BPT diagram for the GMRT sources that have $[\text{OIII}]$, $\text{H}\beta$, $[\text{NII}]$, $\text{H}\alpha$ detections. The black stars represents the BPT-SF classification, blue clubsuits represents BPT-Comp (dominated by seyferts/star-forming galaxies.) and the red open circles represents the BPT-AGN classifications. The [Kauffmann *et al.* \(2003\)](#) empirical and [Kewley *et al.* \(2001\)](#) theoretical divisions are plotted to separate the sources.

3.8.2 Comparison between the emission line diagnostic and other AGN diagnostics

The misidentification of X-ray selected AGN and other AGN diagnostics as star-forming dominated galaxies is a potential issue for all optical line diagnostics. We investigate this issue by comparing the BPT-NII classification with our initial AGN classification outlined in the schematic in Section 3.4 (see Figure 3.7). This comprises selections using the radio luminosity, x-ray luminosity, BOSS/SDSS spectroscopic pipeline AGNs and radio-loud AGN using MIPS 24 micron flux density.

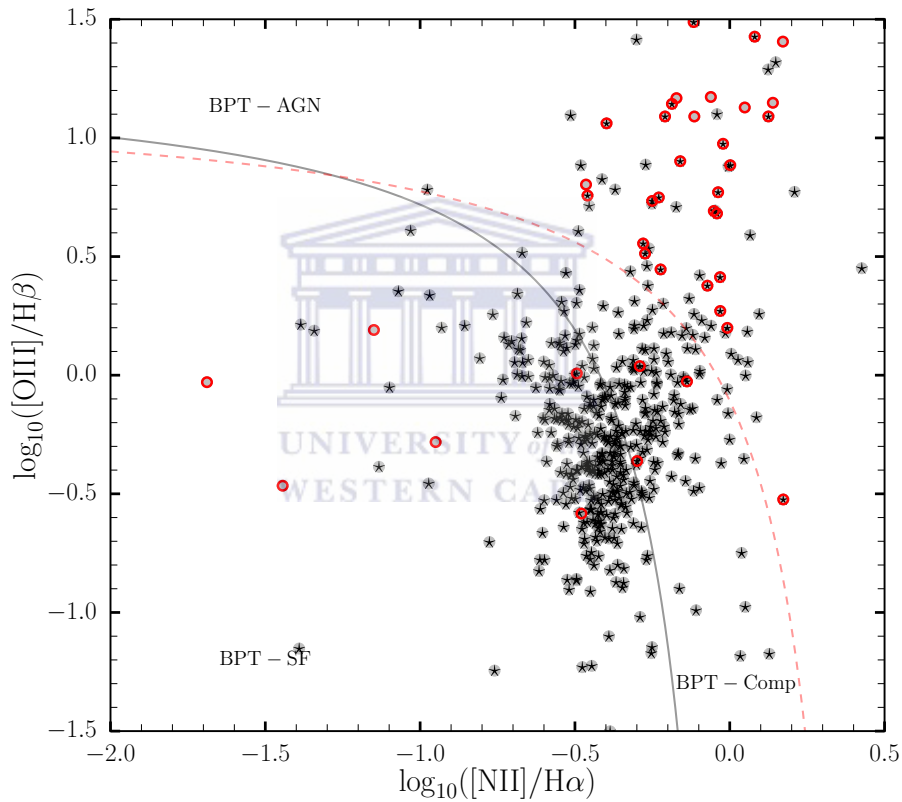


FIGURE 3.24: BPT diagram for the GMRT sources that have $[OIII]$, $H\beta$, $[NII]$, $H\alpha$ detections. The BOSS spectroscopic galaxies and the AGN classification shown in Section 3.4 Figure 3.7 are over-plotted on the BPT.

Figure 3.24 presents the comparison between the BPT-NII diagram for the GMRT sources with detections in the four emission lines (represented by grey circles) and the AGN classification outlined in Section 3.4 (represented by open red circles) and the BOSS/SDSS spectroscopic pipeline galaxy classification (represented by black stars). Out of the 170 AGN sources from Figure 3.7, 40 have four emission line detections. We can infer from the figure that 6 of these sources reside in the BPT-SF region whilst 3 of

them fall within the BPT-Comp region. The remaining 31 of these AGNs reside in the BPT-AGN region.

In Table 3.6, we summarize the results of the comparison between BPT-NII with other AGN diagnostics we have studied so far.

TABLE 3.6: BPT-NII comparison analyses results

Category	Number	Fraction (%)	Galaxies _{spec} ^{BOSS}	AGNs
BPT-SF	298	59%	293	6
BPT-Comp	130	26 %	129	3
BPT-AGN	77	15 %	69	31

^a BPT-SF - star-forming galaxy criterion according to the BPT-NII

^b BPT-Comp - composite galaxy criterion according to the BPT-NII

^c BPT-AGN - AGN galaxy criterion according to the BPT-NII

^d Galaxies_{spec}^{BOSS} - BOSS/SDSS spectroscopic pipeline galaxy classification

^e AGNs - AGN classification presented in Section 3.5 Figure 3.7

We establish that there are some discrepancies between the AGN selection presented in Section 3.5 Figure 3.7 and the BPT classification. To better address this disagreement, we apply signal-to-ratio (SNR) cuts to minimize the effect of objects with low SNR on the various emission line diagnostics. In order to remove these objects with low signal-to-ratio from our sample, we applied SNR cuts of 3, 5 and 10 respectively. We calculate the SNR using the relation below:

$$\text{SNR} = \frac{\text{EW}}{\text{EW}_{\text{error}}} \quad (3.8)$$

Where EW is the equivalent width (area of the line) of the emission line and EW_{error} , is the error measurement in the equivalent width.

Figure 3.25 presents the distribution of the equivalent width of the spectral line divided by the error measurement in the equivalent width, for the GMRT sources with [OIII], [NII], [H α] and [H β] counterparts. The red, black and green vertical lines indicates an SNR cut of 3, 5 and 10 respectively. From this figure we see that at an SNR cut of 5 and 10, we tend to lose many sources therefore we only apply an SNR cut of 3. Figure 3.26 the BPT-NII diagram for GMRT sources with [OIII], H β , [NII], H α detections for an SNR cut of 3. The number of AGNs (see Section 3.5 Figure 3.7) residing in the BPT-SF region is now 5, with only 1 AGN in the BPT-Comp region upon an SNR cut of 3.

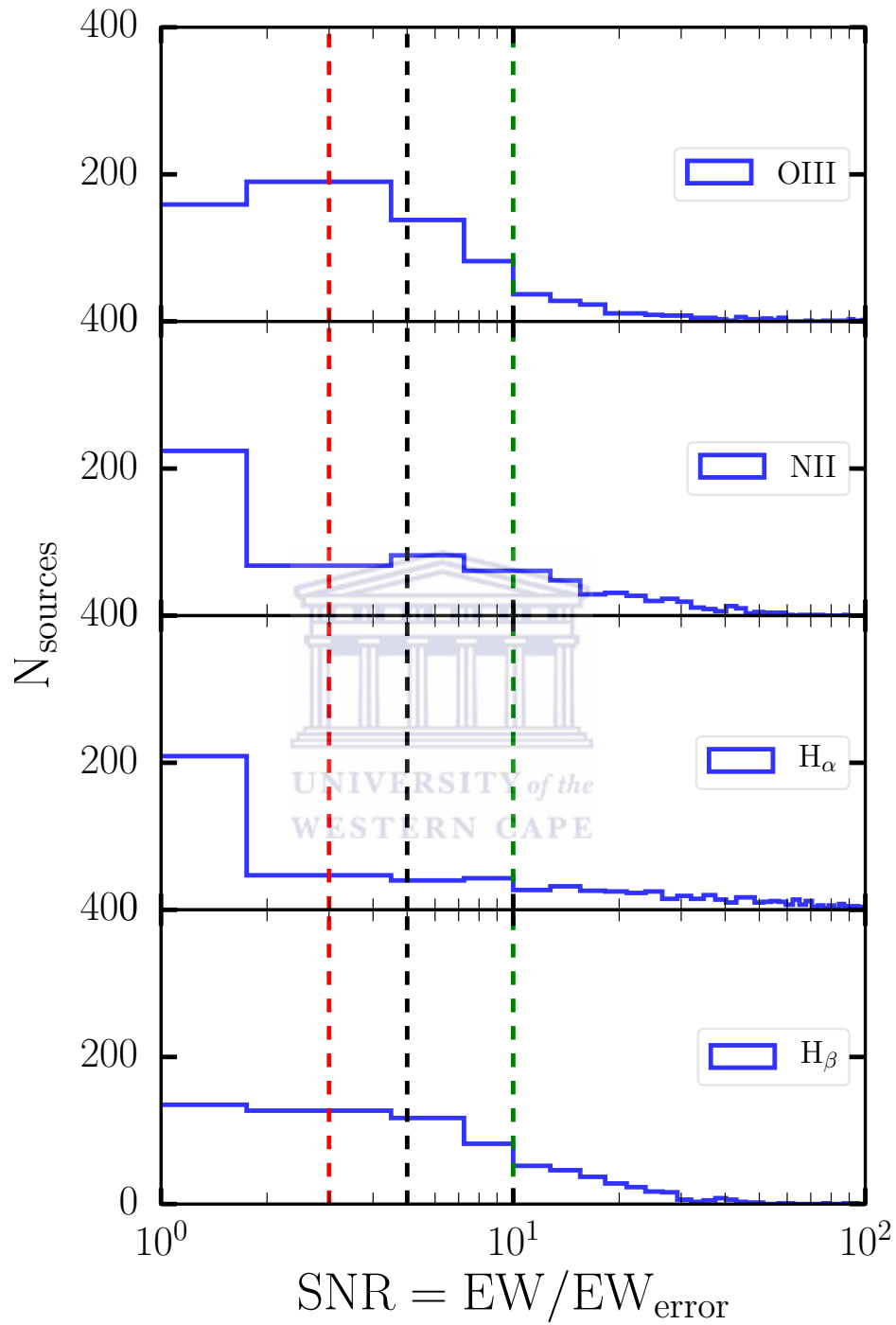


FIGURE 3.25: Histogram of the signal-to-noise ($SNR = EW/EW_{error}$, the equivalent width of the spectral line divided by the error measurement in the equivalent width, for the GMRT sources with [OIII], [NII], [H α] and [H β] counterparts. The red, black and green vertical lines indicates an SNR cut of 3, 5 and 10 respectively.

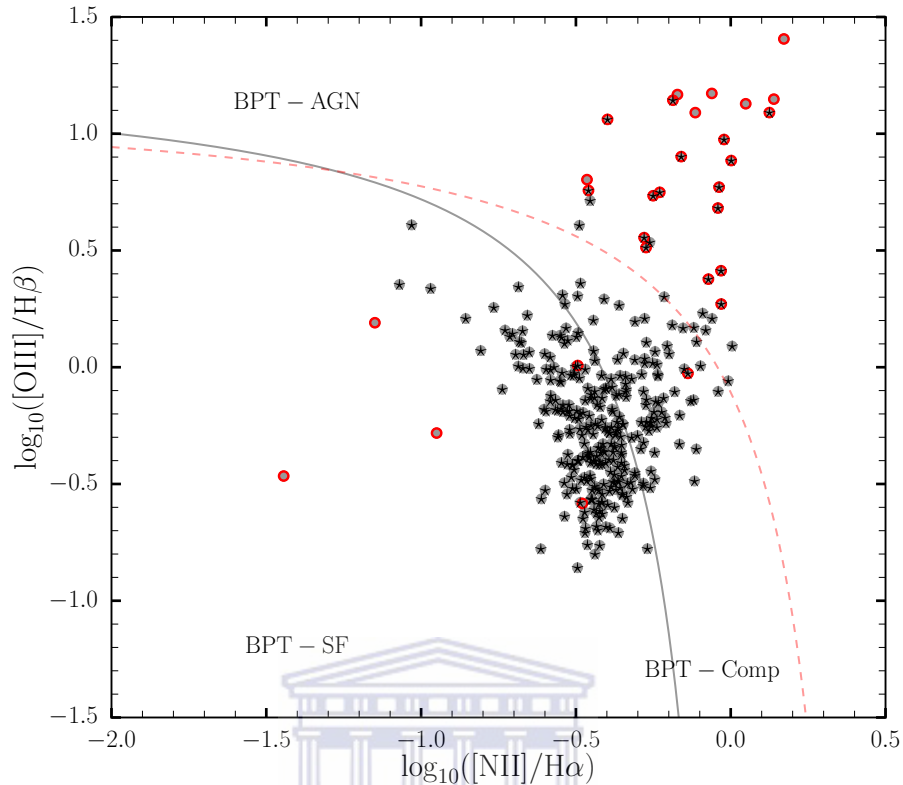


FIGURE 3.26: BPT-NII diagram for GMRT sources with $[OIII]$, $H\beta$, $[NII]$, $H\alpha$ detections for an SNR cut of 3. The plot shows the over-plotted BOSS spectroscopic galaxies and the AGN classification shown in Section 3.5 Figure 3.7. The Kauffmann *et al.* (2003) empirical (solid black curve) and Kewley *et al.* (2001) (dash red curve) (at $z \sim 0$) theoretical divisions are plotted to separate the sources.

3.8.3 Two-line diagnostics

Miller *et al.* (2003) analysed the observed fraction of galaxies with an active galactic nucleus (AGN) in the early data release of the Sloan Digital Sky Survey (SDSS). They used 4921 galaxies in the redshift range $0.05 \leq z \leq 0.095$ and brighter than $M(r^*) = -20.0$ (or $M^* + 1.45$), and found at least $\sim 20\%$ of these galaxies possess an unambiguous detection of an AGN, but this fraction could be as high as $\simeq 40\%$ after they modelled the ambiguous emission-line galaxies in their sample. They showed that it is not necessary to have significant detections of all four of these lines; $[OIII]$, $H\beta$, $[NII]$, $H\alpha$, in order to detect an AGN in a galaxy. On the other hand, it is imperative to have detections for all four lines to classify star-forming galaxies. This fact is illustrated in Figure 3.27, which shows that galaxies with either a high $[NII]/H\beta$ or a high $([OIII]/H\alpha)$ line ratio must be AGNs, regardless of the other line ratio.

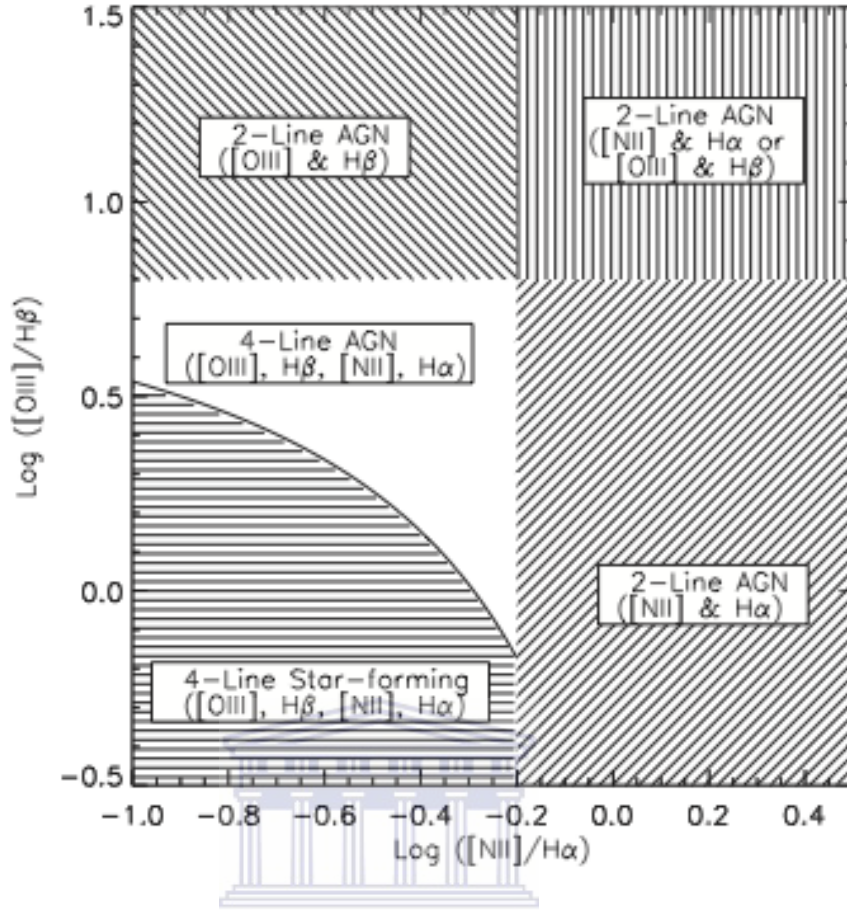


FIGURE 3.27: Illustration of the 2-line diagnostic which shows that galaxies with either a high $[\text{N II}]/\text{H}\beta$ or a high $([\text{O III}]/\text{H}\alpha)$ line ratio must be AGNs, regardless of the other line ratio.. The solid curve shows 1σ limit of [Kewley *et al.* \(2001\)](#) theoretical division curve. Adopted from [Miller *et al.* \(2003\)](#)

Hence, if a galaxy has $\log_{10}([\text{N II}]/\text{H}\alpha) \geq -0.2$ but no significant detections in $[\text{O III}]$ or $\text{H}\beta$, we can still classify it as an AGN following [Miller *et al.* \(2003\)](#). Figure 3.28 presents our illustration of this whereby the equivalent width (EW) of the $[\text{N II}]$ emission line is plotted against the ratio $[\text{N II}]/\text{H}\alpha$ for galaxies in our GMRT sample with the e-line detections shown as grey circles. The dash vertical red line indicates $\log_{10}([\text{N II}]/\text{H}\alpha) \geq -0.2$, where sources beyond this line (to the right of the line) are classified as AGNs according to this two line diagnostic ($\log_{10}([\text{N II}]/\text{H}\alpha)$). The BPT-SF (black stars), BPT-AGN (open red circles) and the BPT-Comp (blue clubsuit) are over-plotted for comparison. This diagnostic selects 133 sources (i.e. 5%) of the GMRT sources as AGNs. Out of the 77 sources classified as BPT-AGNs by the BPT-NII diagnostic, 49 of them agrees with this diagnostic (i.e. have $\log_{10}([\text{N II}]/\text{H}\alpha) \geq -0.2$). Also 36 of the sources classified as BPT-Comp by the BPT-NII diagnostic have $\log_{10}([\text{N II}]/\text{H}\alpha) \geq -0.2$ whilst there is no indication of the BPT-SF having $\log_{10}([\text{N II}]/\text{H}\alpha) \geq -0.2$.

In the same way, if a galaxy has $\log_{10}([\text{O III}]/\text{H}\beta) \geq 0.8$ but no significant detections in $[\text{N II}]$ or $\text{H}\alpha$, we can also classify it as an AGN. This illustration is presented in

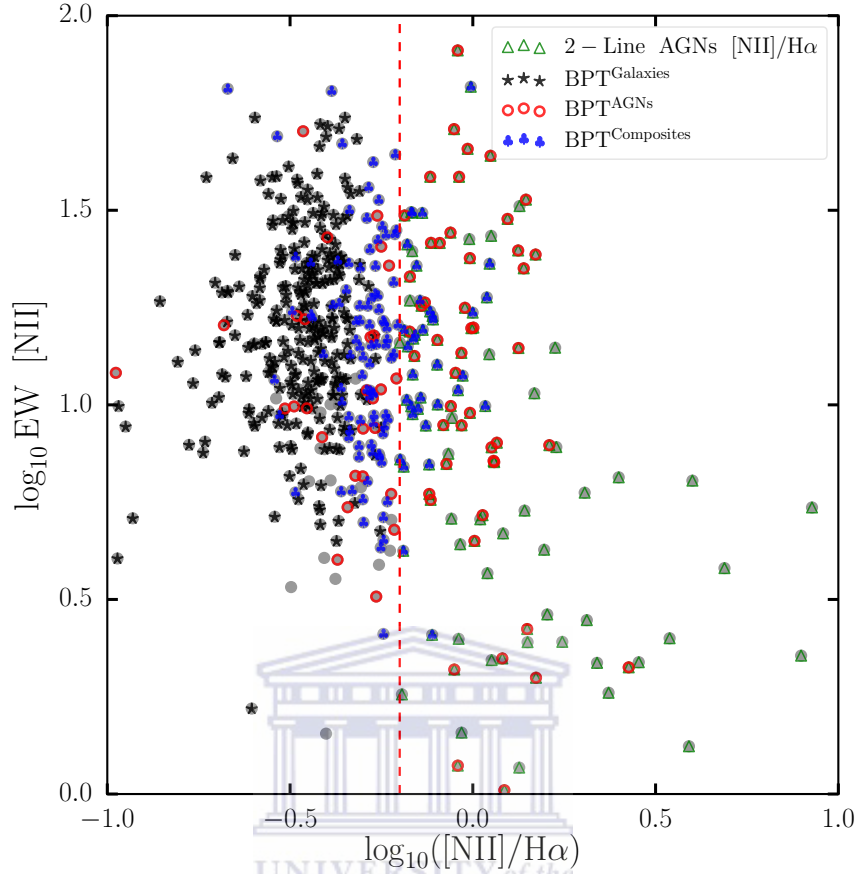


FIGURE 3.28: EW (equivalent width) of the [N II] emission line vs the ratio [N II]/H α for galaxies in our GMRT sample with the corresponding line detections shown as grey circles. The dash vertical red line indicates $\log_{10}([\text{N II}]/\text{H}\alpha) \geq -0.2$, where sources beyond this line are classified as AGNs according to this two line diagnostic ($\log_{10}([\text{N II}]/\text{H}\alpha)$). Over-plotted are the various four line diagnostic criteria i.e., BPT-SF (black stars), BPT-AGN (open red circles) and BPT-Comp (blue clubsuit).

Figure 3.29 whereby the ratio of [O III]/H β is plotted against the equivalent width of the [O III] emission line for galaxies in our GMRT sample with these line detections (grey circles). The dash horizontal red line indicates $\log_{10}([\text{O III}]/\text{H}\beta) \geq 0.8$, where sources above this line are classified as AGNs according to this two line diagnostic ($\log_{10}([\text{O III}]/\text{H}\beta)$). The BPT-SF (black stars), BPT-AGN (open red circles) and the BPT-Comp (blue clubsuit) are also over-plotted for comparison. From the 77 sources classified as BPT-AGNs by the BPT-NII diagnostic, 31 of them agrees with this diagnostic (i.e. have $\log_{10}([\text{O III}]/\text{H}\beta) \geq 0.8$). There is a good agreement for the BPT-SF and BPT-Comp with this diagnostic such that none of the sources classified as this by the BPT-NII have $\log_{10}([\text{O III}]/\text{H}\beta) \geq 0.8$.

We therefore used these two techniques to infer whether the selection of AGNs agrees well with other diagnostics we have studied up until this point in the thesis. Figure 3.30

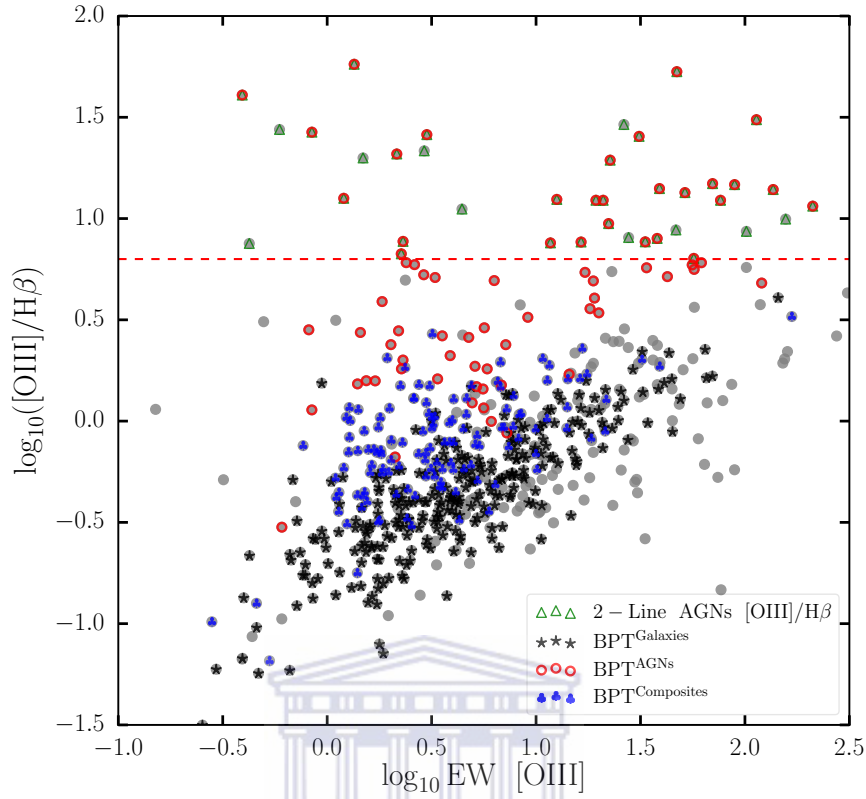


FIGURE 3.29: The ratio of $[\text{O III}]/\text{H}\beta$ vs EW of the $[\text{O III}]$ emission line for galaxies in our GMRT sample with the corresponding line detections shown as grey circles. The dash horizontal red line indicates $\log_{10}([\text{O III}]/\text{H}\beta) \geq 0.8$, where sources above this line are classified as AGNs according to this two line diagnostic ($\log_{10}([\text{O III}]/\text{H}\beta)$). Over-plotted are the various four line diagnostic criteria i.e., BPT-SF (black stars), BPT-AGN (open red circles) and BPT-Comp (blue clubsuit).

presents the EW of the $[\text{N II}]$ emission line vs the ratio $[\text{N II}]/\text{H}\alpha$ for our GMRT sample (grey circles) compared to the BOSS/SDSS spectroscopic galaxy classification and the AGN criteria according to the schematic in Section 3.5 Figure 3.7. From the total of 170 sources selected as AGNs in Section 3.5, 33 of these sources have $\log_{10}([\text{N II}]/\text{H}\alpha) \geq -0.2$ and thus agrees with this two-line diagnostic as AGNs. 124 sources selected as galaxies by the BOSS/SDSS spectroscopic pipeline also have $\log_{10}([\text{N II}]/\text{H}\alpha) \geq -0.2$ and thus does not agree with this method.

Figure 3.31 presents the same argument as Figure 3.30 with an SNR cut of 3. From this figure, we see that the number of BOSS/SDSS galaxies with $\log_{10}([\text{N II}]/\text{H}\alpha) \geq -0.2$ has decreased upon the SNR cut. The same applies to the number of AGNs (see Section 3.5) having $\log_{10}([\text{N II}]/\text{H}\alpha) \geq -0.2$ however, there are still AGNs having $\log_{10}([\text{N II}]/\text{H}\alpha) \leq -0.2$ (i.e behind the dash red line).

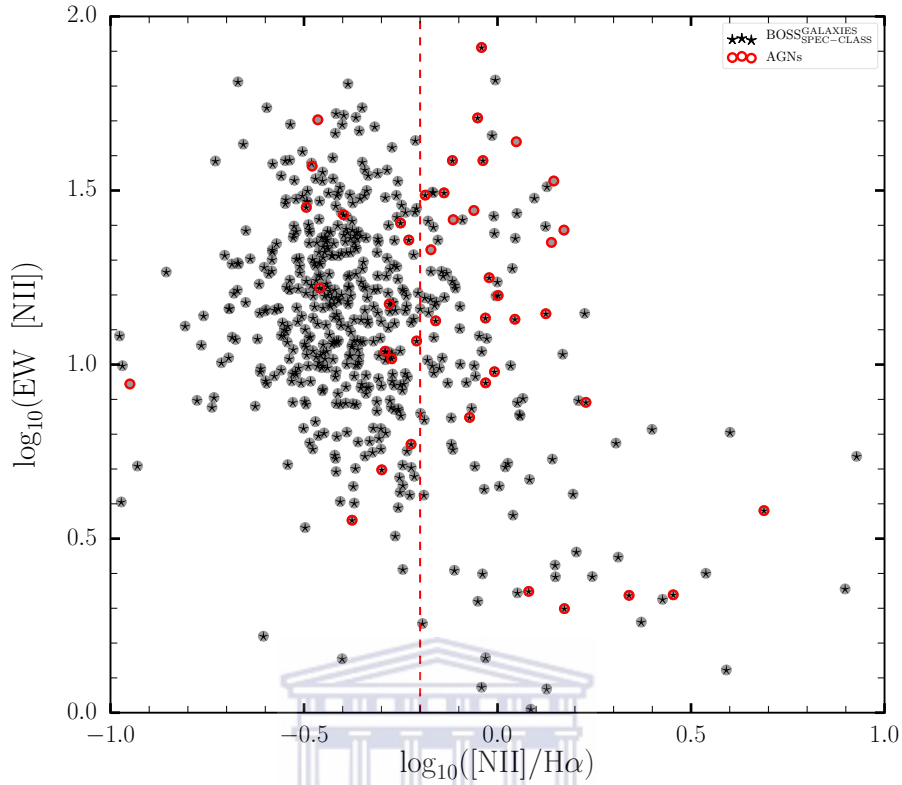


FIGURE 3.30: EW of the [N II] emission line vs the ratio [N II]/H α for galaxies in our GMRT sample with the corresponding line detections shown as grey circles. The vertical dashed red line indicates $\log_{10}([\text{N II}]/\text{H}\alpha) \geq -0.2$, where sources above this line are classified as AGNs according to this two line diagnostic ($\log_{10}([\text{N II}]/\text{H}\alpha)$). Over-plotted are the BOSS spectroscopic galaxies and the AGN classification shown in Section 3.5 Figure 3.7.

Figure 3.32 presents the the ratio [O III]/H β vs EW of the [O III] emission line for galaxies in our GMRT sample (grey circles) compared to the BOSS/SDSS spectroscopic galaxy classification and the AGN criteria according to the schematic in Section 3.5 Figure 3.7. Also, 21 of the sources classified as AGNs in Section 3.5 $\log_{10}([\text{O III}]/\text{H}\beta) \geq 0.8$. 46 sources selected as galaxies by the BOSS/SDSS spectroscopic pipeline have $\log_{10}([\text{O III}]/\text{H}\alpha) \geq 0.8$.

Table 3.7 presents a comparison analyses of the two-line diagnostics with previous results.

Figure 3.33 also presents the same argument as Figure 3.32 with an SNR cut of 3. It is evident that the number of BOSS/SDSS galaxies with $\log_{10}([\text{O III}]/\text{H}\beta) \geq 0.8$ has decreased upon the SNR cut. The same applies to the number of AGNs (see Section 3.5) having $\log_{10}([\text{O III}]/\text{H}\beta) \geq 0.8$ however, there are still AGNs having $\log_{10}([\text{O III}]/\text{H}\beta) \leq 0.8$ (i.e below the dash red line).

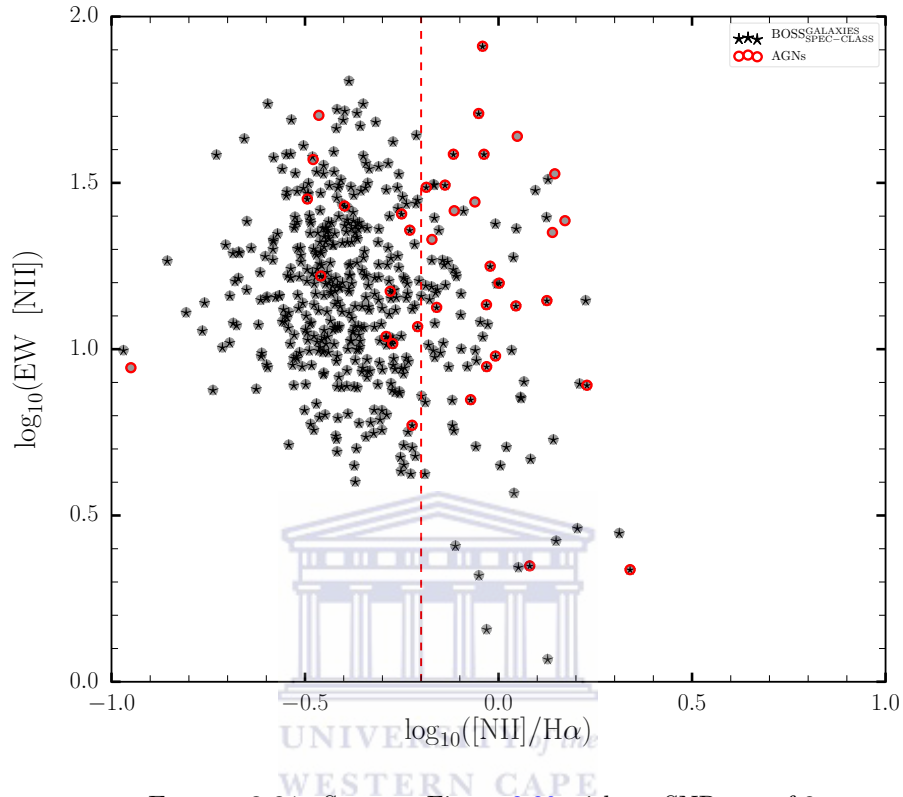


FIGURE 3.31: Same as Figure 3.30 with an SNR cut of 3.

TABLE 3.7: Comparison of the Two-line diagnostics with previous results

Category	Number ^{AGN}	Galaxies ^{BOSS_{spec}}	AGNs	BPT-SF	BPT-Comp	BPT-AGN
$\log_{10}([\text{N II}]/\text{H}\alpha) \geq -0.2$	133	124	33	0	36	49
$\log_{10}([\text{O III}]/\text{H}\beta) \geq 0.8$	46	36	21	0	0	31

^a $\log_{10}([\text{N II}]/\text{H}\alpha) \geq -0.2$ - two-line AGN diagnostic using the ratio $[\text{N II}]/\text{H}\alpha$

^b $\log_{10}([\text{O III}]/\text{H}\beta) \geq 0.8$ - two-line AGN diagnostic using the ratio $[\text{O III}]/\text{H}\beta$

^c Galaxies^{BOSS_{spec}} - BOSS/SDSS spectroscopic pipeline galaxy classification

^d AGNs - AGN classification presented in Section 3.5 Figure 3.7

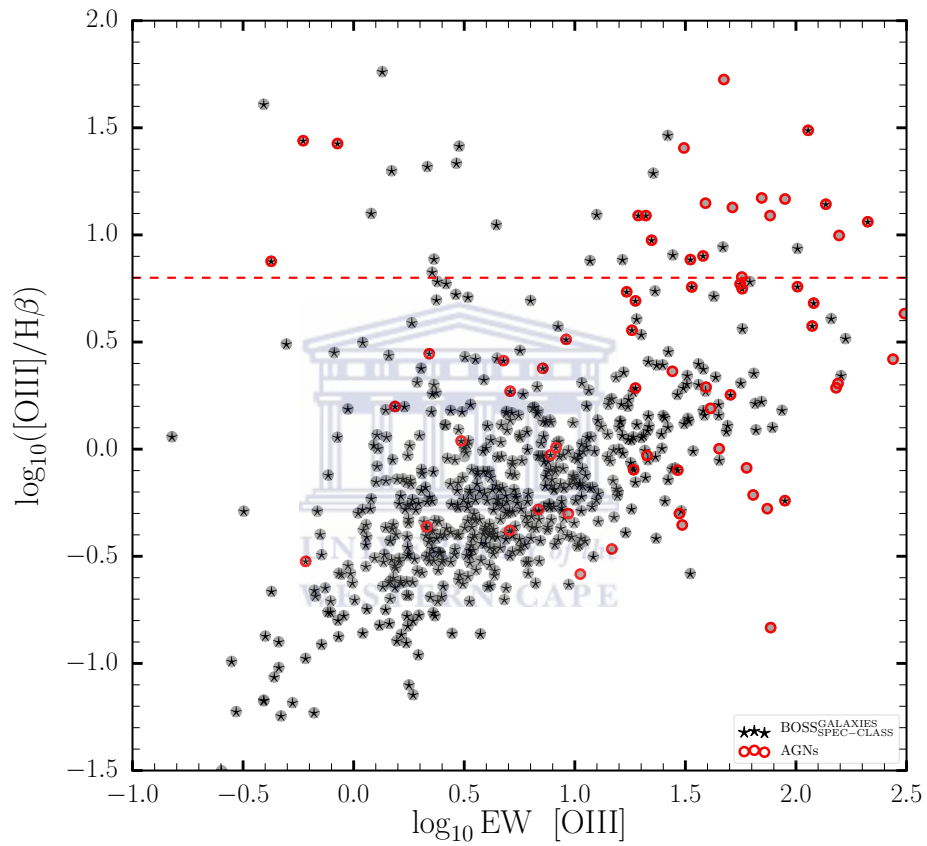


FIGURE 3.32: The ratio $[\text{O III}]/\text{H}\beta$ vs EW of the $[\text{O III}]$ emission line for galaxies in our GMRT sample with the corresponding line detections shown as grey circles. The horizontal dashed red line indicates $\log_{10}([\text{O III}]/\text{H}\beta) \geq 0.8$, where sources above this line are classified as AGNs according to this two line diagnostic ($\log_{10}([\text{O III}]/\text{H}\beta)$). Over-plotted are the BOSS spectroscopic galaxies and the AGN classification shown in Section 3.5 Figure 3.7.

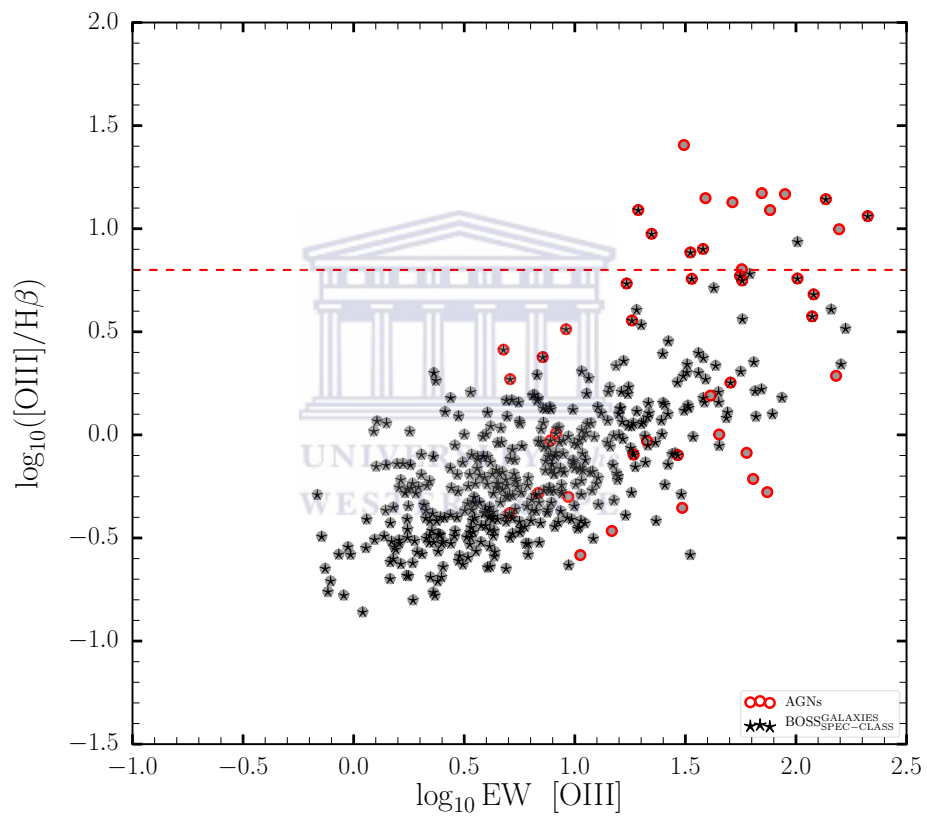


FIGURE 3.33: Same as Figure 3.32. This plot indicates an SNR cut of 3.

3.9 Summary

This Chapter builds upon the results presented in Chapter 2 where we cross-matched the wealth of multi-wavelength data available in the EN1 field to the GMRT. We have presented results from the various AGN selection techniques we have studied using the GMRT data, further dividing them into AGNs and SFGs according to the different techniques.

We have used a radio luminosity cut of $L_{1.4\text{GHz}} > 10^{25} \text{ WHz}^{-1}$ as a radio-loud AGN criterion and an X-ray luminosity cut of $L_{2-10\text{keV}} > 10^{42} \text{ erg s}^{-1}$ to select sources as AGNs. To differentiate between SFGs and RQ AGNs it is instead necessary to consider other AGN activity indicators, namely the optical spectroscopy and the MIR observed colours. We have also shown that the ratio between the IR and radio emission, parametrized by the $q_{24\mu\text{m}}$ value, is the key parameter needed to identify radio-loud AGNs following [Bonzini *et al.* \(2013\)](#). Combining the selection methods mention beforehand with our BOSS/SDSS spectroscopic classifications follow-up our GMRT sources, we have built an initial classification scheme selecting 170 (i.e. 6%) radio sources as AGNs. The simplicity of our scheme makes it suitable to be applied to large radio samples with ancillary X-ray and IR data, without the need of MIR color-color classifications. We have used this scheme to studied the MIR color evolution of galaxies. We have study the most common MIR (IRAC colors) diagnostics, namely the Lacy, Stern and the Donley wedges. Comparing our classification scheme to the Lacy and Stern selected AGNs we find many differences. However, our classification the scheme agrees well with the Donley criterion.

We have also studied the four-line diagnostics (BPT-N II diagram) and the two-line diagnostics (using $\log_{10}([\text{N II}]/\text{H}\alpha) \geq -0.2$ and $\log_{10}([\text{O III}]/\text{H}\beta) \geq 0.8$) for our sample with the four optical line ratios ($[\text{O III}]/\text{H}\beta$, $[\text{N II}]/\text{H}\alpha$). Comparing the line ratios of our sample to the our classification scheme, many discrepancies occur between our developed AGN selection scheme and where AGNs reside with respect the various emission line diagnostics. Even upon applying an SNR cut of 3 on the emission lines to removes sources with low SNR, we still see differences. Therefore the discrepancies between our earlier AGN selection and the BPT is not sensitive to signal to noise. Based on these discrepancies, we do not use the emission line diagnostics in our over all classification scheme which is presented in Chapter 4.

Chapter 4

Nature of the faint radio sources

4.1 AGN or SFG ?

The faint radio sky is a complex mixture of star forming galaxies (SFG) and active galactic nuclei (AGN) (e.g., [Mauch and Sadler \(2007\)](#); [Smolčić *et al.* \(2008\)](#)). The radio emission can either be due to the relativistic jets powered by the AGN at the centre of a galaxy or to the synchrotron emission associated with magnetic field and relativistic electrons in the galaxy disks.

Below a flux density of about 1 mJy the synchrotron emission generated in the ordinary non-active star-forming galaxies in the local universe becomes detectable ([Condon, 1992a](#)) as well as more powerful starburst galaxies at larger distances. Thus the radio population becomes a mixture of star-forming galaxies, and radio-loud AGN. In addition radio emission from radio-quiet AGN star to be detected ([Rawlings and Jarvis, 2004](#)). Henceforth, the relative contributions of each of these classes of radio sources at sub-mJy levels has for many years been the subject of much debate (e.g. [Seymour *et al.* \(2008a\)](#); [Huynh *et al.* \(2008\)](#); [Ibar *et al.* \(2009\)](#); [Padovani *et al.* \(2009\)](#)).

In this Chapter 4, we divide the radio source population into sources whose radio emission is powered by an AGN or by star formation, mainly through the diagnostics in Chapter 3. We outline the five AGN indicators we employ, use this to ascertain whether the radio emission is powered by star formation or by an AGN for a sub-sample of our sources with redshift out of the entire GMRT population. We measure the far-infrared radio correlation and investigate how this evolves with redshift and whether there is any dependence on either radio or far-infrared luminosity.

4.1.1 Classification criteria and results

We have carried out a multi-wavelength study, i.e using optical , X-ray and IR data, as different AGN emission processes can be probed by a different wavebands. We apply five observational-based indicators to our sources to identify whether an AGN is present provided they exhibit one of the following:

1. Radio power, $L_{1.4 \text{ GHz}} \geq 25 \text{ WHz}^{-1}$.
2. X-ray luminosity greater than $10^{42} \text{ erg s}^{-1}$.
3. BOSS AGN spectroscopic classification (see Section 3.3 Chapter 3).
4. Radio-loud AGN flags defined according to [Bonzini *et al.* \(2013\)](#).
5. IRAC colours satisfying the [Donley *et al.* \(2012\)](#) criteria

For criterion (1), this radio-loud AGN classification range was used since it has been shown that radio emission above this luminosity, is mainly due to the relativistic jets (e.g. see [Sajina *et al.* \(2007\)](#); [Jiang *et al.* \(2007\)](#)). Although AGN could have radio power less than this threshold, if a source has a radio luminosity above or equal to this range then we infer that this is because of the presence of an AGN.

For criterion (2), extragalactic studies often use an X-ray luminosity cut of $10^{42} \text{ erg s}^{-1}$ to distinguish between AGNs and SFGs (see [Fabbiano \(1989\)](#); [Moran *et al.* \(1996\)](#)). However, this is not the theoretical upper limit to star-forming X-ray luminosities. Following [Rawlings *et al.* \(2015\)](#), we caution that there is the possibility for a number of star-forming sources in the sample to have an X-ray luminosity above this cut. For criterion (3), we know beforehand that the BOSS/SDSS spectroscopic pipeline classifications comprises of AGNs and SFGs. The description of the sources we select as AGN according to BOSS is outlined in Chapter 3 Section 3.3. Therefore through our cross-matched, we were able to associate the AGNs classification to their GMRT counterparts.

We used the same approach employed by [Bonzini *et al.* \(2013\)](#), for criterion (4). But in our case, we use the k -corrected 1.4 GHz flux density, for sources with MIPS $24_{\mu\text{m}}$ counterparts to calculate $q_{24_{\mu\text{m}}}$.

We then explored the various MIR color classifications (i.e. Lacy, Stern, Donley) in order to be able to classify many of the radio sources with four band IRAC detections as possible. We have compared these MIR color classifications to other AGN diagnostics that we studied. We identify several discrepancies between the MIR color classifications and other AGN diagnostics especially with the Lacy wedge. The wedge included color regions that are predominantly occupied by BOSS/SDSS SFGs. We found a similar problem with the Stern wedge. The Donley wedge was however found to be the best

discriminator of SFGs and AGNs. Only few number of BOSS/SDSS SFGs were found to reside in this wedge, hence we used the Donley wedge (see Section 3.7.3 Chapter 3). A schematic of this combined AGN nomenclature is described in Figure 4.1

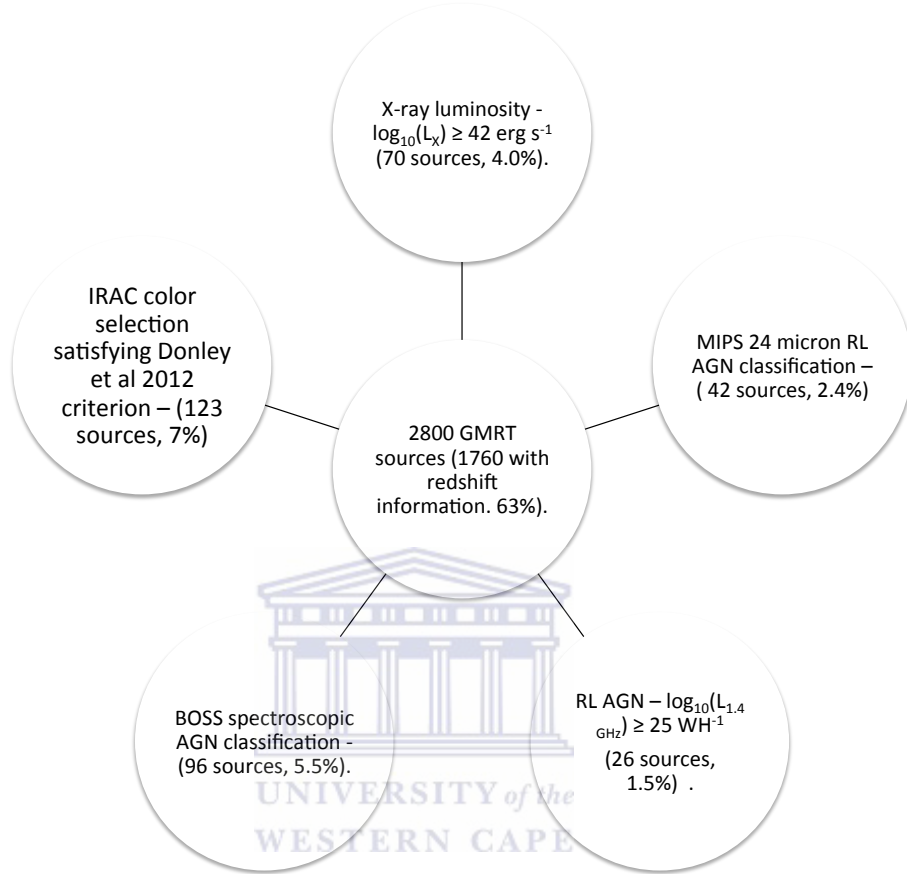


FIGURE 4.1: A schematic of AGN selection combining the selection described in Figure 3.7 of Section 3.4 with the MIR selection satisfying Donley *et al.* (2012). The percentages presented here are with respect to the sources with redshifts.

We separated from the 2800 radio sources, a sub-sample of 1760 sources which constitutes the GMRT population with redshift associations (i.e., 63%, see Chapter 2 Table 2.1). Using the above AGN indicators, we deduce whether or not the observed radio emission is powered by an AGN, for the sources in the sub-sample. If we have been unable to show that an AGN is present in the source from the above nomenclature, then we inferred the radio emission of the source is powered by star formation. If there is an indication of an AGN activity in the source satisfying any of the criteria 1 to 5, then we inferred the radio emission of the source is powered by an AGN, regardless of the results from the other indicators. Our AGN classification is very conservative, therefore we note that our SFG class is strongly contaminated by AGN unrecognized as such. Using this approach, we have been able to classify 86% as SFGs and 14% as AGNs for our GMRT sources with redshift associations as presented in Table 4.1. However this comprises 54% SFGs and 9% AGNs of our entire 2800 radio population thus leaving 37% of the

GMRT population not classified. [Rawlings *et al.* \(2015\)](#) separated the extragalactic radio source population above $\sim 50\mu\text{Jy}$ into AGN and SFGs by fitting IR SEDs constructed using Spitzer/IRAC, MIPS and Herschel/SPIRE photometry, of 380 radio sources in the Extended Chandra Deep Field South. Overall, they found that for 153 of the 380 sources, the radio emission is powered by star-formation. For 95 sources, the radio emission is powered by an AGN whereas the remaining 132 sources have were found to be hybrids (i.e. no sign of jet activity, not clear whether or not the radio emission is powered by AGN ([Rawlings *et al.*, 2015](#))).

TABLE 4.1: Total number of AGNs and SFGs from a combination of the selection described in Figure 4.1 of Section 4.1.1 plus the various MIR classification criteria for sources with redshift.

SFGs	SFGs Fraction (%)	AGNs	AGNs Fraction (%)
1515	86 %	247	14%

4.2 The far-infrared radio correlation

The far-infrared radio correlation (FRC) is one of the tightest and most universal empirical correlations known among global parameters of the observed galaxies. Presently, the FRC is believed to be driven mostly by star formation ([Condon \(1992a\)](#) ; [Yun *et al.* \(2001\)](#)). The correlation spans over a wide range of galaxy types and seems to be valid both for local and distant Universe. The reasons why the thermal dust emission at far-infrared wavelengths should be so tightly coupled to the non-thermal radio emission are not clear. One simple explanation assumes that UV and optical radiation from the most massive stars are completely absorbed by dust and re-radiated in the far-infrared, these massive stars end their lives as supernovae explosions the remnants of which creates the relativistic electrons that power synchrotron radio emission. The far-infrared and radio emission are thus both related to the levels of massive star-formation taking place in the galaxy. [Voelk \(1989\)](#) proposed this calorimeter argument where it assumes that all the energy from cosmic ray electrons accelerated by supernova remnants is converted to synchrotron radiation and all UV radiation is converted to far-infrared. Therefore the galaxy can be viewed simultaneously as an electron and a UV calorimeter. However, this is only valid if the galaxy is optically thick to UV radiation and neglects both non-synchrotron cooling and proton losses. Non-synchrotron cooling results in a decrease in the proportion of energy converted to radio emission in high density starburst environments while proton losses will instantly increase the number of secondary electrons emitting synchrotron emission. These effects may act to balance each other out in high density environments maintaining a constant FRC. For low density galaxies both the UV

and electron calorimeter approximations no longer hold, thus decreasing both the radio and far-infrared emission (see e.g. [Lacki *et al.* \(2010\)](#); [Lacki and Thompson \(2010\)](#)).

We used the integrated (8 - 1000 μm , rest frame) far-infrared luminosities (FIR) from the [Rowan-Robinson *et al.* \(2013\)](#) to examine the correlation between the infrared luminosity and the rest frame 1.4 GHz radio luminosity. These luminosities were calculated using photometric redshifts by [Rowan-Robinson *et al.* \(2013\)](#) but in our case, we defined a master redshift (z_{ultra}) whereby we use spectroscopic redshifts if available or the photometric redshifts (z_{phot} from [Rowan-Robinson *et al.* \(2013\)](#) when the spectroscopic redshift is not available in order to get redshifts for majority of our sources. Therefore, we applied the correction given by equation 4.1 below to get the corrected $L_{\text{IR,CORR}}$, since the FIR luminosities were originally derived using photometric redshifts from [Rowan-Robinson *et al.* \(2013\)](#).

$$L_{\text{IR,CORR}} = \frac{d_{\text{L,ZULTRA}}^2}{d_{\text{L,ZMRR13}}^2} \times L_{\text{IR,CAT}} \quad (4.1)$$

$L_{\text{IR,CAT}}$ represents the original far-infrared luminosity from the MRR13 catalog, $d_{\text{L,ZULTRA}}^2$ represents the luminosity distance calculated using our defined master redshift (z_{ultra}) whereas $d_{\text{L,ZMRR13}}^2$ represents the luminosity distance calculated using the redshifts from the MRR13 catalog. Figure 4.2 presents the Integrated 8 - 1000 micron luminosity from MRR13 catalog for our GMRT sample. We were able to associate 1279 GMRT sources with FIR luminosity from the catalog (see Table 2.1 Chapter 2). The dashed red vertical line indicates the median infrared luminosity of the GMRT sample of $\sim 11.5 L_{\odot}$.

Figure 4.3 presents the total IR luminosity (L_{IR}) as a function of redshift for SFGs (left panel) and AGNs (right panel) from the GMRT sample with [Rowan-Robinson *et al.* \(2013\)](#) FIR luminosity detections. We plot limits of LIRGs, ULRGs and HyLIRGs, see [Patel *et al.* \(2013\)](#), to show where the sources lie based on their IR luminosity. The distribution of the 1.4 GHz radio luminosity for our GMRT sample is presented by Figure 4.4 whereby the dash red vertical line indicates the median radio luminosity which is $\sim 10^{23.3} \text{ WHz}^{-1}$.

We characterised the IR/radio properties of our sources by the logarithmic total IR (infrared luminosities from the MRR13 catalog)/radio flux ratio q_{IR} ([Helou *et al.*, 1985](#)).

$$q_{\text{IR}} = \log_{10} \left(\frac{L_{\text{IR}}}{3.75 \times 10^{12} \text{ W}} \right) - \log_{10} \left(\frac{L_{1.4\text{GHz}}}{\text{WHz}^{-1}} \right) \quad (4.2)$$

In our following analysis we consider the median q_{IR} of our sample, since this provides a better indicator of the most typical value in case our sample has some outliers. We also compute the median absolute deviation (MAD). This is a robust measure of the

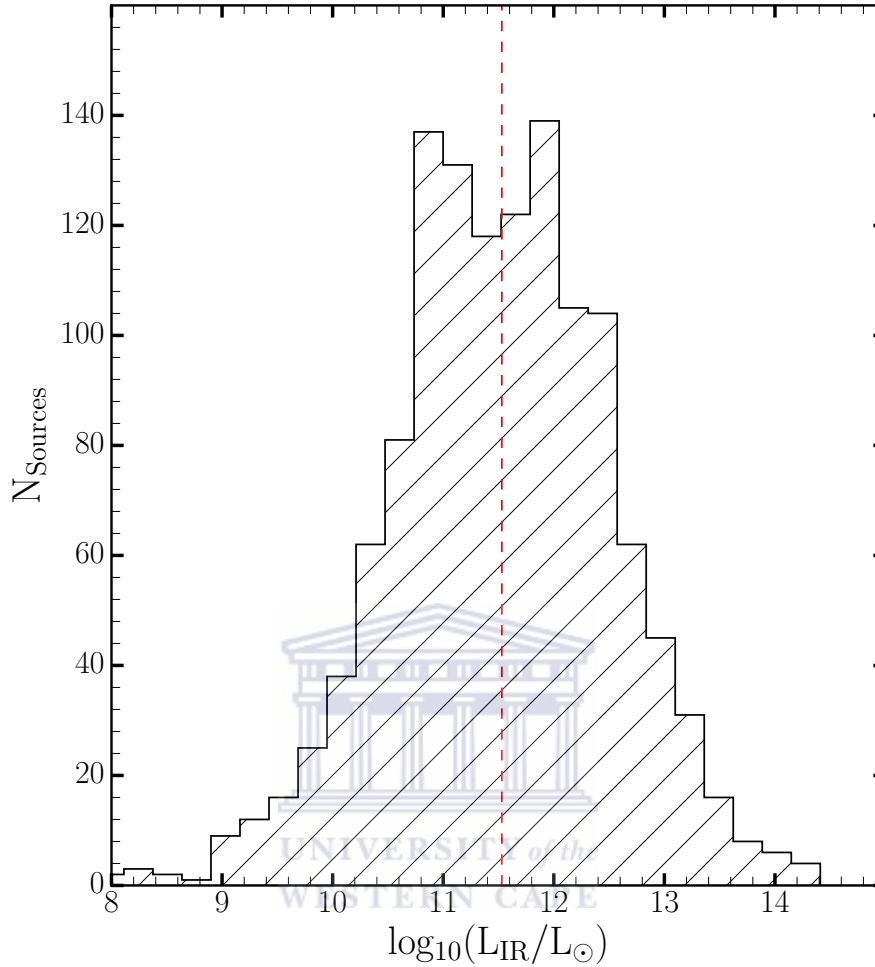


FIGURE 4.2: Histogram of the Integrated 8 - 1000 micron luminosity from MRR13 catalog for our GMRT sample. The dashed red vertical line indicates the median infrared luminosity [Rowan-Robinson *et al.* \(2013\)](#).

variability of a univariate sample of quantitative data.

$$\text{MAD} = \text{median}_i(|X_i - \text{median}_j(X_j)|) \quad (4.3)$$

The MAD can be directly related to the standard deviation σ , in a Gaussian distribution

$$\sigma \approx 1.4826\text{MAD} \quad (4.4)$$

In other words, the expectation of 1.4826 times the MAD for large samples of normally distributed X_i is approximately equal to the population standard deviation. Hence, the

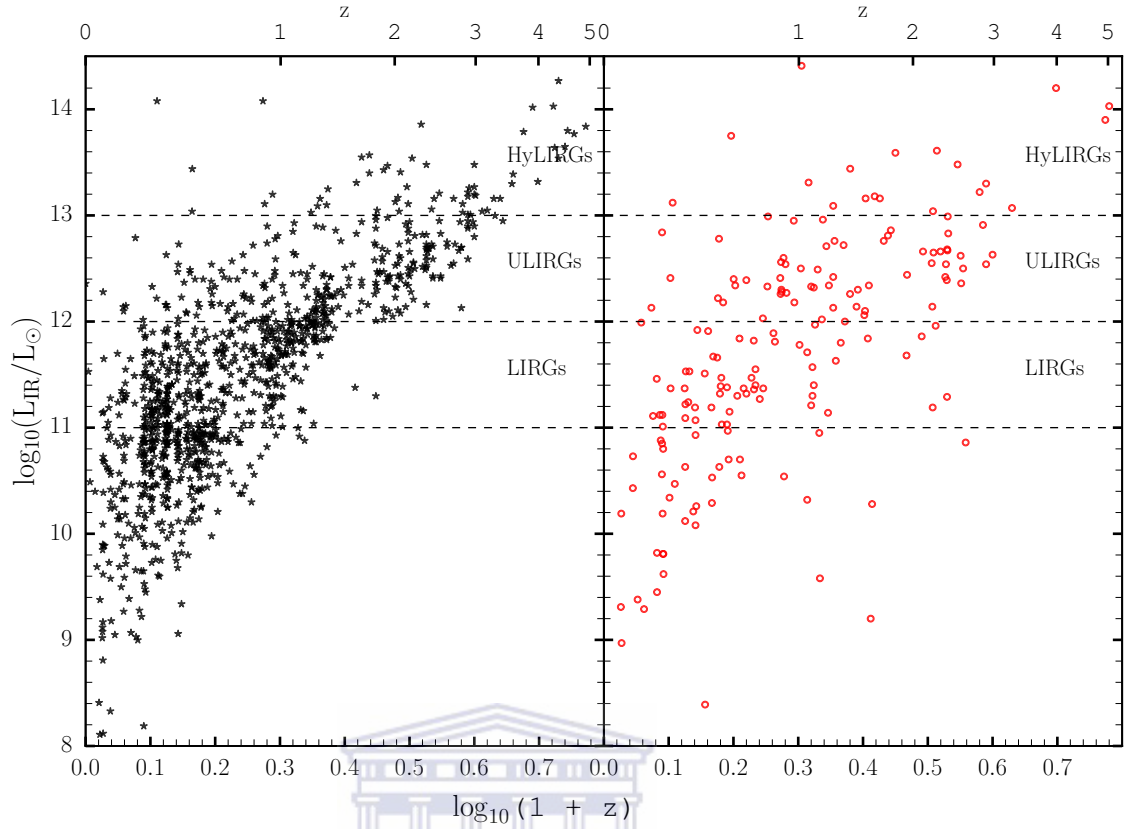


FIGURE 4.3: Total IR luminosity (L_{IR}) as a function of redshift for SFGs (left panel) and AGNs (right panel) from the GMRT sample. We plot limits of LIRGs, ULIRGs and HyLIRGs, see [Patel et al. \(2013\)](#), to show where the sources lie based on their IR luminosity.

error on the MAD is given by,

$$\text{MAD}_{\text{error}} = \frac{1.4826\text{MAD}}{\sqrt{N}} \quad (4.5)$$

where N is the number of sources.

Figure 4.5 presents radio power at 1.4 GHz versus FIR luminosity for SFGs detected by our classification. The contours represent the $0.25 \times 1\sigma$, $0.5 \times 1\sigma$, $0.75 \times 1\sigma$, 1σ , 2σ and 3σ of the GMRT sources with radio and IR luminosity respectively. The solid line shows the q_{IR} relation given in Equation 4.2 for the respective lySFGs (top panel) and AGNs (bottom panel). The dotted lines in both panels indicate the $\pm 1\sigma$ dispersion in the value of the calculated q_{IR} . The SFGs have a tight correlation with the FRC, with a median q_{IR} value of 2.45 ± 0.01 . The AGN-powered sources, lie slightly above the FRC with a median q_{IR} value of 2.27 ± 0.05 . The decrease in the median value of q_{IR} can be attributed to the additional AGN component to radio emission. The additional component to the radio luminosity for the AGN-powered sources results in lower q_{IR}

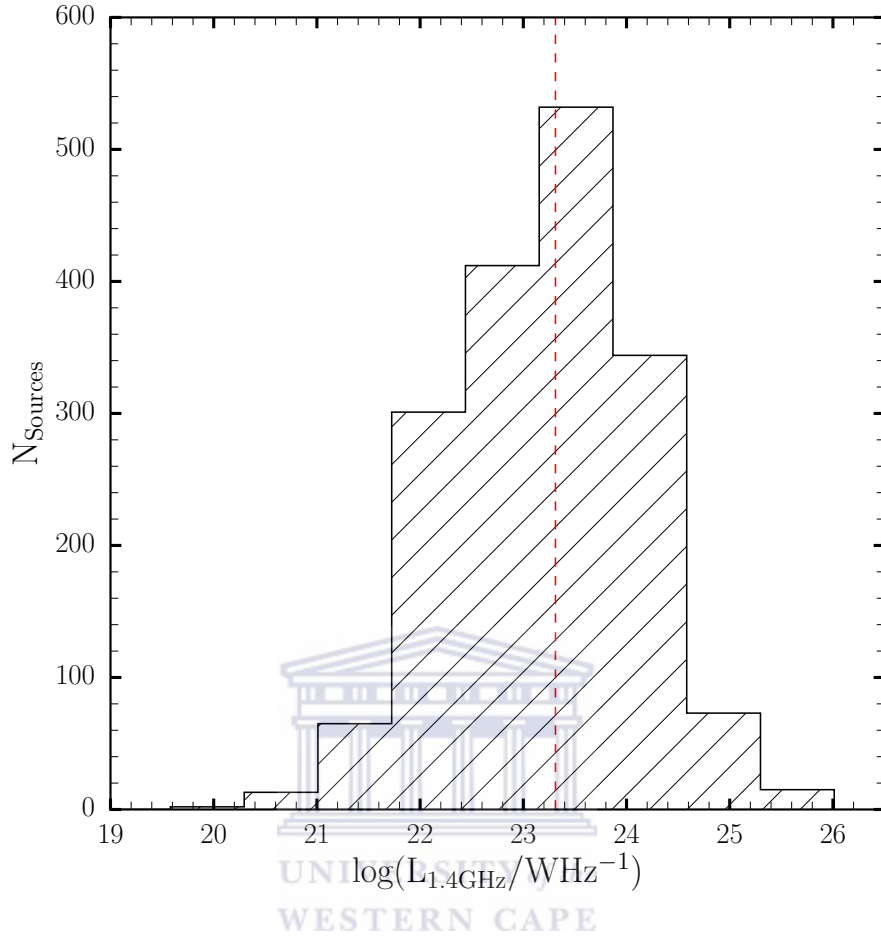


FIGURE 4.4: Histogram of the 1.4 GHz radio luminosity for our GMRT sample. The dash red vertical line indicates the median radio luminosity.

values (Rawlings *et al.*, 2015). However, for both the SFGs and AGNs, we see that the sources lie above the the median q_{IR} line at the low luminosity end. This is evident for $L_{\text{IR}} \lesssim 10.5 L_{\odot}$ and $L_{1.4\text{GHz}} \lesssim 10^{22} \text{ W Hz}^{-1}$.

Our median $q_{\text{IR}} = 2.45 \pm 0.01$ is in good agreement with previous measurements obtained by studying the FRC (e.g. Ivison *et al.* (2010b); Magnelli *et al.* (2010)). These previous studies used submillimetre galaxy (SMG) samples which were mostly biased towards sources with strong radio emission via the reliance on radio imaging to obtain counterpart IDs. Ivison *et al.* (2010b) a median $q_{\text{IR}} = 2.40 \pm 0.12$ reported for a sample of IR-bright ($S_{250\mu\text{m}} \gtrsim 20 \text{ mJy}$) galaxies out to $z < 3.5$. The median q_{IR} is higher too than $q_{\text{IR}} = 2.17 \pm 0.19$, as measured by Magnelli *et al.* (2010) for a sample of bright ($S_{850\mu\text{m}} > 5 \text{ mJy}$) single-dish submillimetre sources observed in GOODS-N. However, this value is lower than that reported by Thomson *et al.* (2014) who measured a median $q_{\text{IR}} = 2.56 \pm 0.05$ by studying the radio properties of 870 μm -selected submillimetre

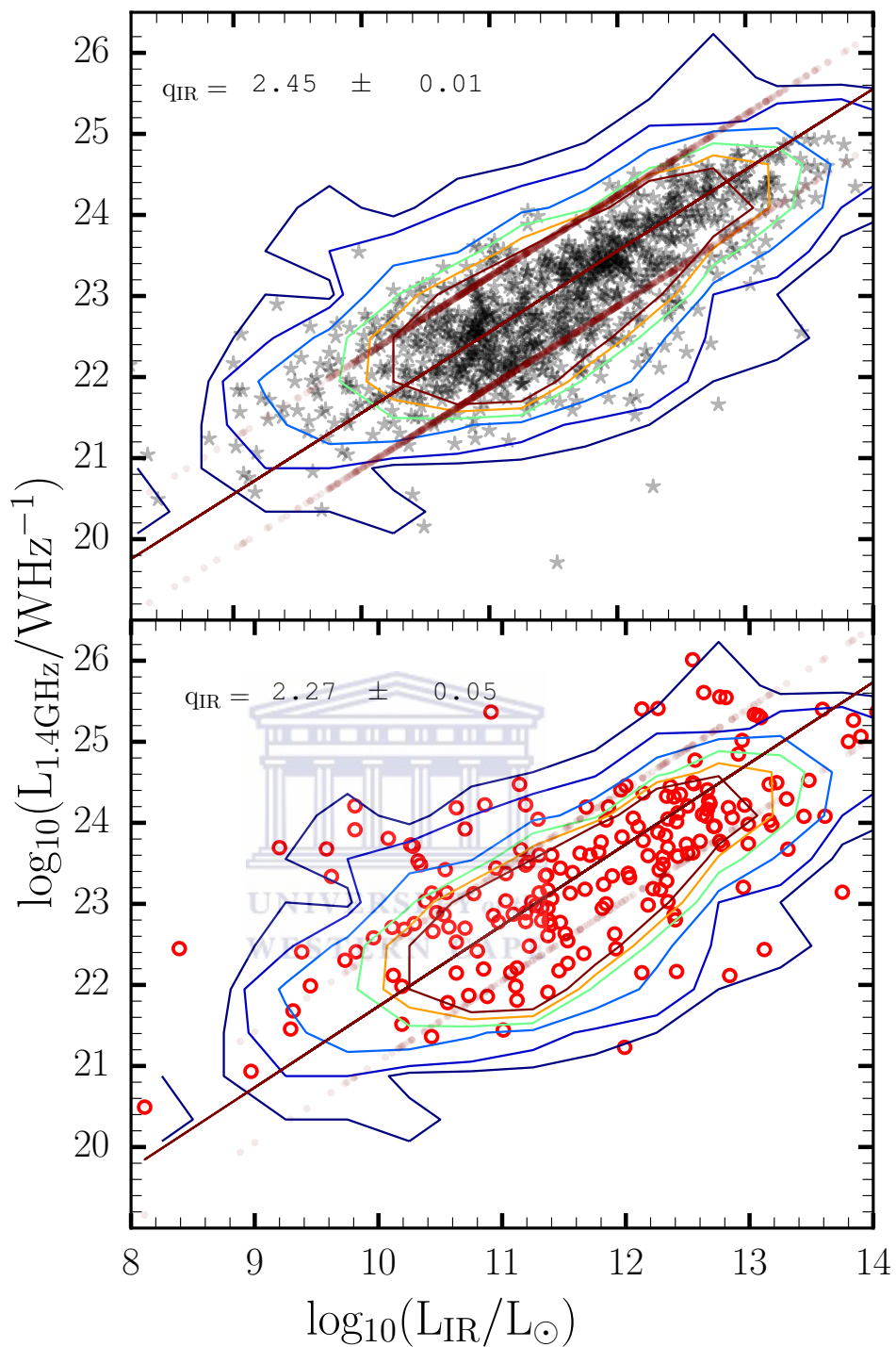


FIGURE 4.5: $L_{1.4\text{ GHz}}$ versus L_{\odot} for SFGs (top panel) and AGNs (bottom panel) according to the AGN selection described in Figure 4.1 of Section 4.1.1. The contours show $0.25\times 1\sigma$, $0.5\times 1\sigma$, $0.75\times 1\sigma$, 1σ , 2σ and 3σ of the GMRT sources with radio and IR luminosity respectively.

galaxies, observed at high resolution with ALMA in the Extended Chandra Deep Field South. Our measurement of q_{IR} is also lower than that reported by Bell (2003) who

measured $q_{\text{IR}} = 2.64 \pm 0.02$ for 162 galaxies with IR and radio data and no signs of AGN by assembling a sample of SFGs with FUV, IR and radio data to quantitatively explore the radio-IR correlation.

4.3 Luminosity dependence

Considering the large number of objects available to us due to the high-sensitivity of the GMRT, we can be able to investigate the form of the far-infrared radio correlation over a range of redshifts, far-infrared luminosities and radio luminosities. Therefore, following [Sargent *et al.* \(2010\)](#), [Jarvis *et al.* \(2010\)](#) and [Iverson *et al.* \(2010a\)](#) we split our sample into four radio luminosity bins (Figure 4.6) and four far-infrared luminosity bins (Figure 4.7) and determine the mean and median value for q_{IR} in each of these bins in order to investigate their q_{IR} distribution more quantitatively.

4.3.1 Binning in radio luminosity

The right panel of Figure 4.6 shows q_{IR} versus redshift for our selected star-forming galaxies, split into four log-spaced bins of $L_{1.4\text{GHz}}$ with the median values of q_{IR} in each panel shown. The grey regions in the left panel of Figure 4.6 shows the various binning ranges both in the vertical and horizontal axes whereas the number of SFGs residing in each range is printed at the bottom. We find that the median values of q_{IR} decrease with increasing radio luminosity from $q_{\text{IR}} = 2.60 \pm 0.02$ for $10^{20.0} \leq (L_{1.4\text{GHz}}/\text{WHz}^{-1}) < 10^{22.5}$ to $q_{\text{IR}} = 2.37 \pm 0.02$ for $10^{22.5} \leq (L_{1.4\text{GHz}}/\text{WHz}^{-1}) < 10^{23.5}$ and increases slightly to $q_{\text{IR}} = 2.39 \pm 0.02$ for $10^{23.5} \leq (L_{1.4\text{GHz}}/\text{WHz}^{-1}) < 10^{24.5}$ then increases to $q_{\text{IR}} = 2.45 \pm 0.06$ for $10^{24.5} \leq (L_{1.4\text{GHz}}/\text{WHz}^{-1}) \leq 10^{25.5}$. Table 4.2 presents the q_{IR} in the different radio luminosity bins. The most straightforward explanation of this is that there we have an increasing fraction of AGN contamination as we advance to higher radio luminosities. Figure 4.7 show again that there is a tight correlation between radio power and redshift. This means that you cannot disentangle possible luminosity trends (see Table 4.2) from possible redshift trends. The increase in q_{IR} at low-power/low-redshift, if real, can be due either to the galaxy luminosity or to the galaxy redshift. We therefore suggest that the evidence for an increase in the FIRC towards low redshifts found by previous authors (eg. [Bourne *et al.* \(2011\)](#) [Jarvis *et al.* \(2010\)](#)) can be explained by one or a combination of resolving out extended radio emission in high-resolution radio data coupled with an increased contribution from dust heated by evolved stars at progressively lower redshifts.

Rowan-Robinson (2003) and Calzetti *et al.* (2010) outlined at longer wavelength the IR emission has an increasing contribution from evolved stars. From this explanation we would then expect the low-redshift sources to exhibit less correlation with the radio emission due to the fact that our data definitely probe longer rest-frame wavelengths. Jarvis *et al.* (2010) from their analyses of Herschel-ATLAS: far-infrared radio correlation explained that this would not have a large effect within their data set which is limited to $z < 0.2$ for direct detections. However, they also stated that when considering the evolution from $z \sim 1$ to 0, this could explain the increase in q_{IR} towards the low redshifts, where there is an increased relative contribution to the total far-infrared luminosity from dust heated by evolved stars.

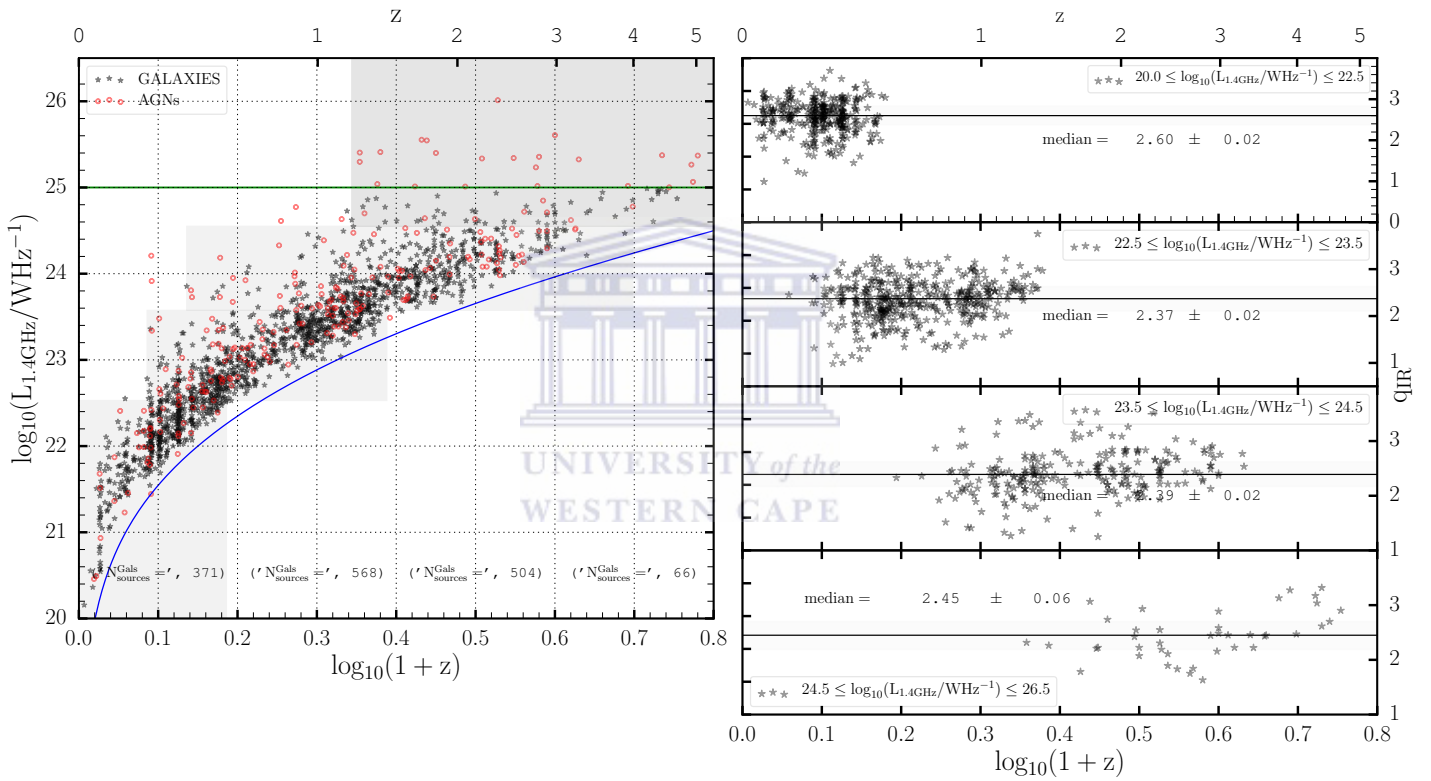


FIGURE 4.6: Left panel: Radio power vs redshift for all sources classified as AGNs and SFGs according to our combined multi-wavelength classification satisfying the Donley Wedge with respect to the MIR. The GMRT flux density limit (solid blue curve) and the adopted luminosity threshold to classify a source as a radio-loud AGN (solid green line) are shown. Right panel: The FIRC as a function of redshift separated into four radio luminosity bins shown in the individual panels. The solid horizontal line in each panel shows the median value of q_{IR} for all non-AGN sources and the grey shaded area shows the median absolute deviation(MAD) of the same sources.

TABLE 4.2: q_{IR} trend in the different radio luminosity bins

q_{IR}	SFGs
$\log_{10}^{(L_{1.4\text{GHz}})} \in [20.0, 22.5]$	2.60 ± 0.02
$\log_{10}^{(L_{1.4\text{GHz}})} \in [22.5, 23.5]$	2.37 ± 0.02
$\log_{10}^{(L_{1.4\text{GHz}})} \in [23.5, 24.5]$	2.39 ± 0.02
$\log_{10}^{(L_{1.4\text{GHz}})} \in [24.5, 26.5]$	2.45 ± 0.06

4.3.2 Binning in infrared luminosity

Figure 4.7 shows the q_{IR} parameter as a function of redshift, also split into into four log-spaced bins of far-infrared luminosity. Similarly, the grey regions in the left panel of Figure 4.7 shows the various binning ranges both in the vertical and horizontal axes whereas the number of SFGs residing in each range is printed at the bottom. We find evidence that the median q_{IR} increases with far-infrared luminosity. We find evidence that the median q_{IR} increases with far-infrared luminosity, such that $q_{\text{IR}} = 2.12 \pm 0.08$ for $10^{8.0} \leq (L_{\odot}) < 10^{10.0}$ to $q_{\text{IR}} = 2.41 \pm 0.01$ for $10^{10.0} \leq (L_{\odot}) < 10^{12.0}$. This continues to increase at $q_{\text{IR}} = 2.60 \pm 0.02$ for $10^{12.0} \leq (L_{\odot}) < 10^{13.0}$ through to $q_{\text{IR}} = 2.88 \pm 0.05$ for $10^{13.0} \leq (L_{\odot}) \leq 10^{15.0}$. Table 4.3 presents the q_{IR} in the different radio luminosity bins.

TABLE 4.3: q_{IR} trend in the different infrared luminosity bins

q_{IR}	SFGs
$\log_{10}^{(L_{\text{IR}})} \in [8.0, 10.0]$	2.12 ± 0.08
$\log_{10}^{(L_{\text{IR}})} \in [10.0, 12.0]$	2.41 ± 0.01
$\log_{10}^{(L_{\text{IR}})} \in [12.0, 13.0]$	2.50 ± 0.02
$\log_{10}^{(L_{\text{IR}})} \in [13.0, 15.0]$	2.88 ± 0.05

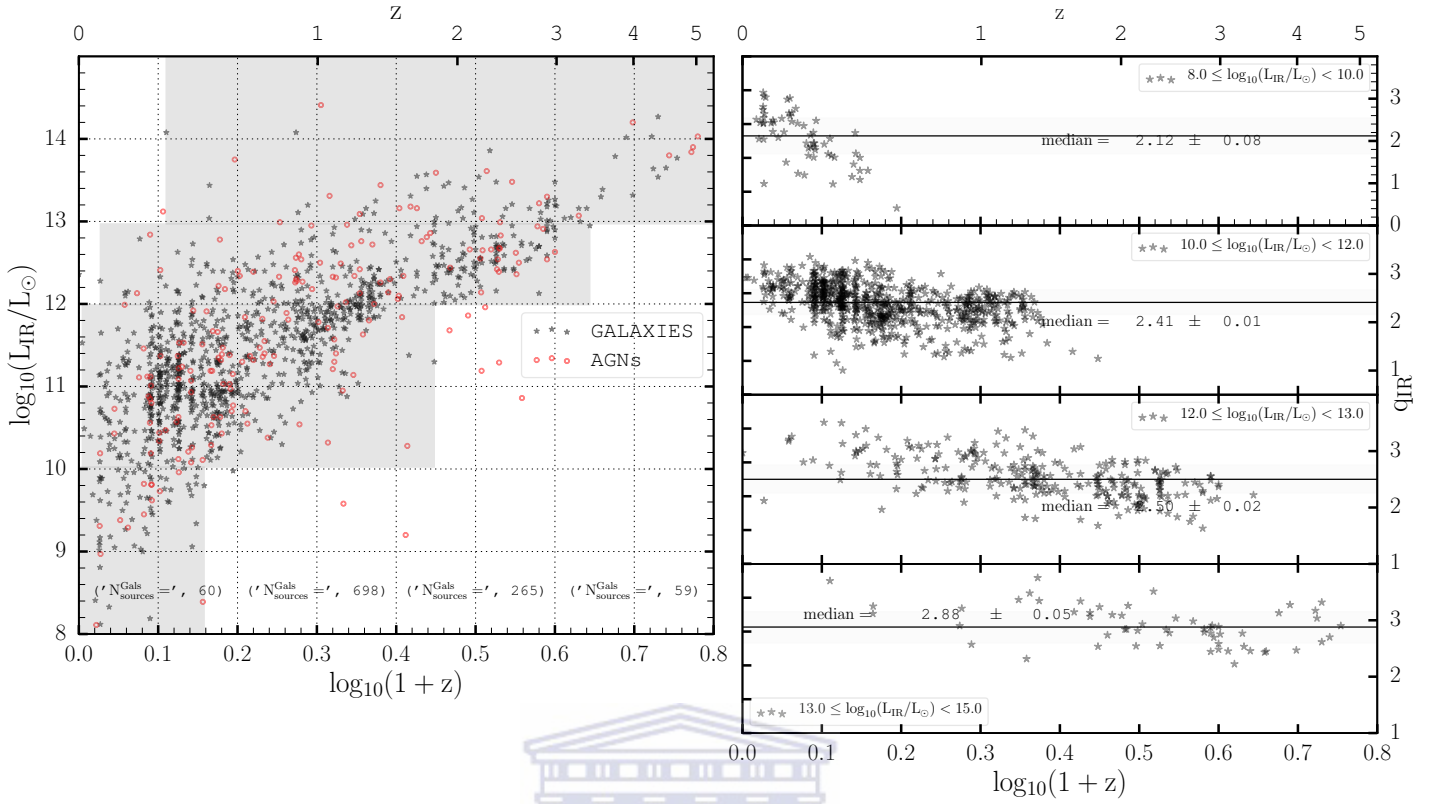


FIGURE 4.7: Left panel: Infrared luminosity vs redshift for all sources classified as AGNs and SFGs according to our combined multi-wavelength classification satisfying the Donley Wedge with respect to the MIR. Right panel: The FIRC as a function of redshift separated into four radio luminosity bins shown in the individual panels. The solid horizontal line in each panel shows the median value of q_{IR} for all non-AGN sources and the grey shaded area shows the median absolute deviation (MAD) of the same sources.

4.4 Summary

The need to better understand the faint radio source population is a primary motivation for the construction of the next generation of radio telescopes, the study presented in this chapter thus joins the increasing ranks of detailed small area studies of faint radio sources which aim to uncover the results of these much anticipated surveys.

The various diagnostics presented in Chapter 3 has enabled us to separate star-forming galaxies and AGN in a sub-sample of 1760 sources, comprising the sources with redshift. These various multi-wavelength AGN indicators, have revealed that there are sources in the GMRT population that contain an AGN. Many of the AGN indicators used in this study are conservative and therefore we can be confident that the AGN identifications are reliable. We determined that for 227 (i.e. 8%) of these sources out of 2800 sources, the radio emission is powered by an AGN. For 55% of our GMRT population, there is no

sign of an AGN and their radio emission is therefore being powered by star formation. The remaining 37% have not been classified as they do not have redshift associations.

Using a combination of the far-infrared data from [Rowan-Robinson *et al.* \(2013\)](#) and the radio data from the GMRT we study the FRC and we find median $q_{\text{IR}} = 2.45 \pm 0.01$ for the sources we select as SFGs in this Chapter 4.

Separating the sample into bins of radio luminosity shows that in our far-infrared detected sample the FRC is consistent with being constant with radio luminosity for sources restricted to the regime where star-forming systems dominate. The weak dependence of q_{IR} on $L_{1.4\text{GHz}}$ likely reflects the influence of low radio-power AGN. However, the dependence of q_{IR} on L_{IR} is more puzzling, perhaps reflecting the dependence of L_{IR} on redshift, or dust temperature T_{d} (e.g. [Chapman *et al.* \(2005\)](#)), or even selection effects



Chapter 5

Summary and future work

This thesis presents the study of the nature of radio sources microJy source population over a survey area of 1.2 deg^2 comprising of 2800 sources with the GMRT at 610 MHz down to an rms noise of $10.3 \mu\text{Jy}/\text{beam}$. This work is particularly useful for paving the way to upcoming radio surveys that current and future radio facilities will provide. Indeed, we are at the dawn of a bright era for radio astronomy as many radio facilities have been recently upgraded or are in construction phase (e.g., APERTIF, ASKAP, JVLA, e-MERLIN, LOFAR, MeerKAT). Radio continuum surveys with these new facilities have been planned with the goal of studying the formation and evolution of galaxies and AGNs over cosmic time. The upcoming large surveys with the SKA pathfinders and precursor telescopes will detect tens of millions of radio sources down to below 1 mJy, and the SKA itself will detect hundreds of millions of objects down to the microJy levels, that we explore in this thesis. It is therefore extremely important to be able to predict which kind of sources these facilities will observe and what are the key data in other spectral windows necessary to complement the radio information to maximise the scientific outputs of these projects.

Using a variable search radius equal to three times the estimated astrometric error., we identified the IR, optical and X-ray counterparts of the radio sources with a completeness of 85%. For about 63% of the sources we were able to associate a redshift, 29% of which are spectroscopic (see Chapter 2). The counterparts and redshift catalog have been compiled. This first part of the thesis demonstrated the key role played by MIR bands in the identification of radio sources. Indeed, a significant fraction of them (15%) are not detected even in deep multi-wavelength data, probably due either to obscuration or to their high redshift. Future surveys with SKA pathfinders require a means to separate the star-forming galaxies and AGN contributions at faint flux densities but there is the difficulty of obtaining spectroscopic observations over large areas of sky for such sources.

The Chapter 3 of the project was aimed at disentangling the different radio populations that contribute to the faint radio sky. We have explored different methods, that combines radio, MIR, optical and X-ray data, to efficiently separate the radio sources in two classes: SFGs and AGNs. We have shown that selection method commonly used in the literature based on the optical emission lines sources (i.e, BPT diagram) may miss a significant fraction of sources classified by different diagnostics as AGNs. We have determined the relative contribution of the two different classes of sources and we find that 86% are SFGs and 14% are AGNs. This confirms the overcoming of SFGs over AGNs in this faint regime. Therefore the upcoming radio surveys, that will be deeper than the observation considered in this work reaching the nanoJy sensitivity, the classical radio-loud AGNs will be a minority of the sources and the population will be dominated by normal star forming galaxies.

We have explored the far-infrared radio correlation of both the AGNs and SFGs of the GMRT sample with redshift associations. The SFGs have a tight correlation with the FRC, with a median q_{IR} value of 2.45 ± 0.01 . The AGN-powered sources, lie slightly above the FRC with a median q_{IR} value of 2.27 ± 0.05 . This decrease in the median value of q_{IR} for the AGNs can be attributed to the additional AGN component to radio emission for the AGN-powered sources results in lower q_{IR} .

Future extensions of the work presented here would be to obtain more spectroscopy and also improved photometric redshifts from SERVS for the radio sources. Spectroscopy would result in more accurate redshift determinations used in this study and could be used to identify and study the evolution of the radio sources out to higher redshifts. Reliable separations of the AGNs and SFGs populations would also be extremely useful in studies of the role of AGN feedback in shaping the global star-formation history of the universe. Obtaining additional mid-infrared data from SWIRE and SERVS surveys, far-infrared observations from Herschel Multi-tiered Extragalactic Survey (HERMES; [Oliver *et al.* \(2012\)](#)) would allow us to study the star-formation activity of AGN across cosmic time to determine if AGN feedback processes influence the star-formation properties of their host galaxies and the relative significance of the two postulated modes of AGN feedback as a function of cosmic time. This would also allow us to extend the classification and investigation of the properties of faint radio sources presented in Chapter 4.

A further useful extension of this work would be to determine the radio luminosity function (RLF) of our GMRT sample and also determine the RLF of the various classifications. The additional data would be very important in the identification both radio-loud and radio-quiet AGN and star-forming galaxies more securely and possibly out to higher redshifts allowing me to derive separate RLF for each of these classes

and determining which sources are primarily driving the different evolutionary trends observed in the RLF of the total faint radio source population.

The FRC study presented in Chapter 4 could also be extended in a number of ways. By using monochromatic far-infrared data (e.g. MIPS 70/160, SPIRE 250/350/500), we can determine whether the monochromatic FRC results will be consistent with the results presented in this study. Previous studies (e.g. Boyle *et al.* (2007); Garn and Alexander (2009); Jarvis *et al.* (2010); Ivison *et al.* (2010b); Bourne *et al.* (2011); Smith *et al.* (2014)) found no evidence for redshift evolution of the FRC as probed by the k-corrected monochromatic 250 μm luminosity density. We can extend our study using the monochromatic FRC to confirm this lack of evolution with redshift. Further extensions would be to probe the temperature dependence of the monochromatic FRC, this illustrates the radio continuum version of the far-infrared 'L-T' relations discussed in several previous studies (e.g. Chapman *et al.* (2003); Hwang *et al.* (2010)). The far-IR temperature/colour dependence of the FIRC is likely to be of critical importance for future investigations, given the upcoming of SKA pathfinder and precursor radio continuum surveys from ASKAP Norris (2011) and Jarvis (2012). Radio observations will be crucial in the future, since they will not only be sufficiently sensitive to detect the entire $z < 0.5$ star-forming galaxy population, they will provide a more reliable tracer of a galaxy's star formation rate than observations sampling long FIR wavelengths ($>250 \mu\text{m}$).

This thesis attempted to classify objects as either SFG or AGN, the situation appears more complex. Not all objects gave unambiguous results over all criteria. In many cases some indicators suggested SFG and others the presence of AGN emission. The reality is that there is likely contributions to both types of emission contributing to the total radiation from a galaxy. We should perhaps rather speak of AGN dominated emission and SFG dominated emission on the ends of a continuous distribution of composite. Future studies should focus on this approach and attempt to place objects on this continuum rather than discrete bins at the extremes of the distribution.

Appendix A

Source Catalog and Radio Observations

Figure A.1 presents the entire distributions of the photometric and the spectroscopic redshifts respectively. In general, the photometric redshifts compare well to the spectroscopic redshifts. Over-plotted are AGNs and SFGs according to optical (top panel) and infrared (bottom panel) SED templates from [Rowan-Robinson *et al.* \(2013\)](#) (see Table 2.1, Section 2.4). SFGs generally follow the one-to-one line (dashed diagonal black line) but AGNs tend to have large departures from this line as presented in both panels.

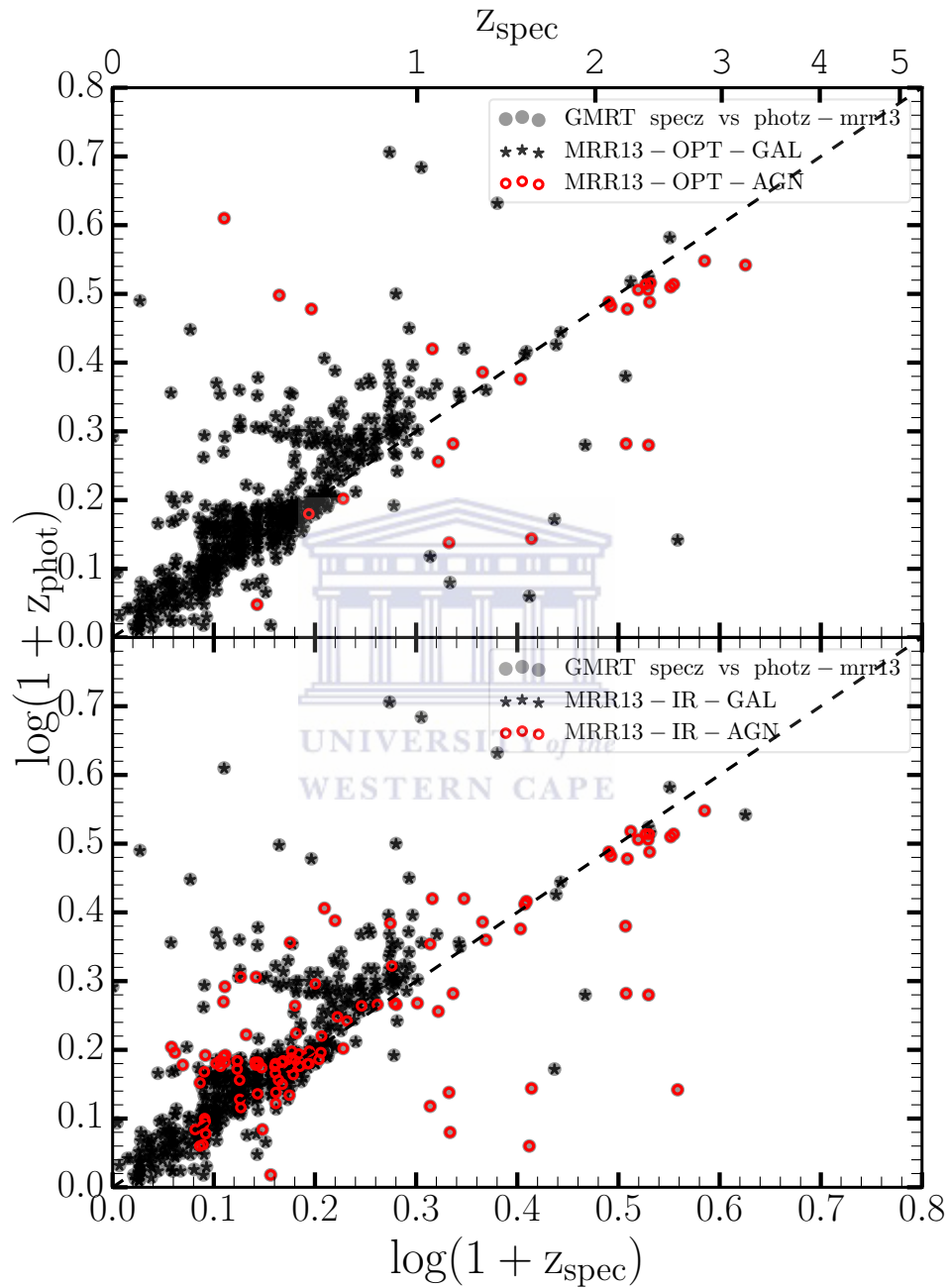


FIGURE A.1: Comparison between photometric and spectroscopic redshifts for the GMRT sources using [Rowan-Robinson *et al.* \(2013\)](#) optical (top panel) and infrared (bottom panel) SED templates for SFGs and AGNs.

Appendix B

AGN Diagnostic Techniques

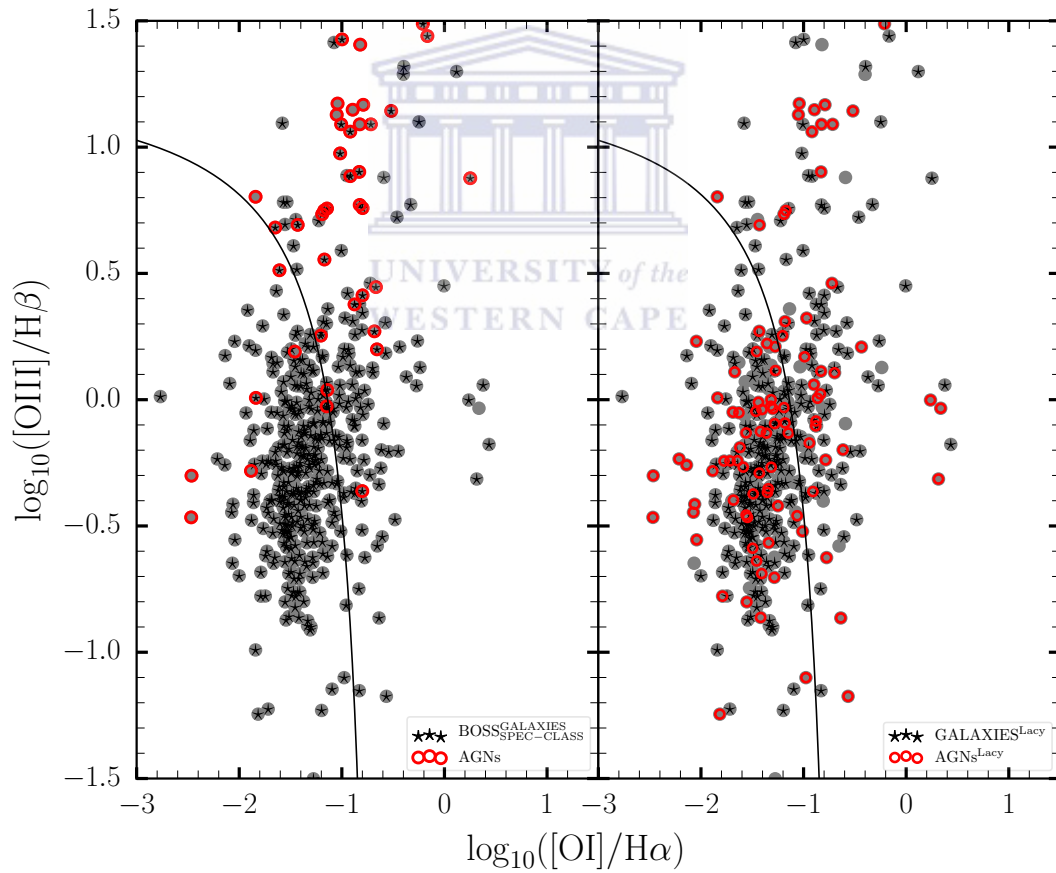


FIGURE B.1: BPT diagram for the GMRT sources that have $[\text{OIII}]$, $\text{H}\beta$, $[\text{OI}]$, $\text{H}\alpha$ detections. The Lacy wedge selected AGNs (open red circles) and SFGs (black stars) classification described in Section 3.7.1 are over-plotted on the BPT-O1.

Figure B.1 presents the comparison between the BPT-OI diagram for the GMRT sources with detections in the four emission lines (represented by grey circles), the AGN (open red circles) and SFG (black stars) classification outlined in Section 3.7.1.

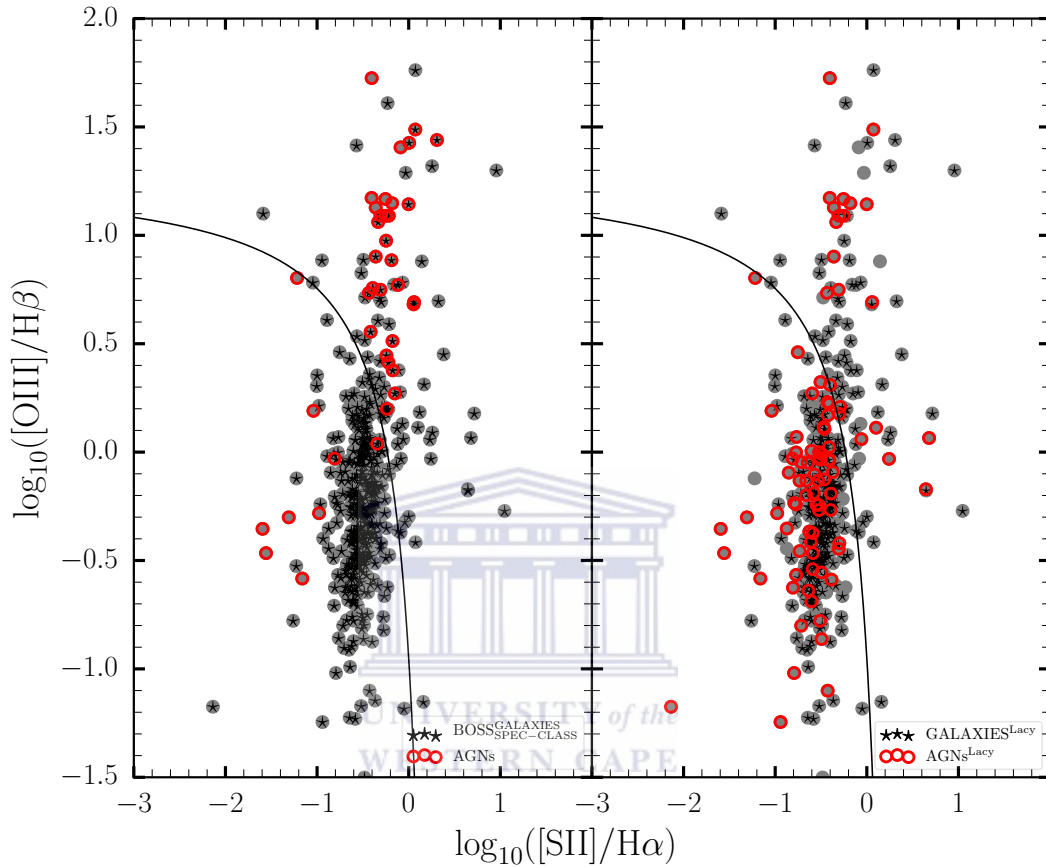


FIGURE B.2: BPT diagram for the GMRT sources that have $[OIII]$, $H\beta$, $[SII]$, $H\alpha$ detections. The Lacy wedge selected AGNs (open red circles) and SFGs (black stars) classification described in Section 3.7.1 are over-plotted on the BPT-SII.

Figure B.2 presents the comparison between the BPT-OI diagram for the GMRT sources with detections in the four emission lines (represented by grey circles), the AGN (open red circles) and SFG (black stars) classification outlined in Section 3.7.1.

B.0.1 Signal to noise cuts

Figure B.3 presents the BPT diagram for the GMRT sources that have $[OIII]$, $H\beta$, $[NII]$, $H\alpha$ detections where the black stars represents the BPT-SF classification, blue clubsuits represents BPT-Comp (dominated by seyferts/star-forming galaxies.) upon using the Kauffmann *et al.* (2003) and the Kewley *et al.* (2001) divisions. The top left, top right and bottom plots indicates an SNR cut of 3, 5 and 10 respectively.

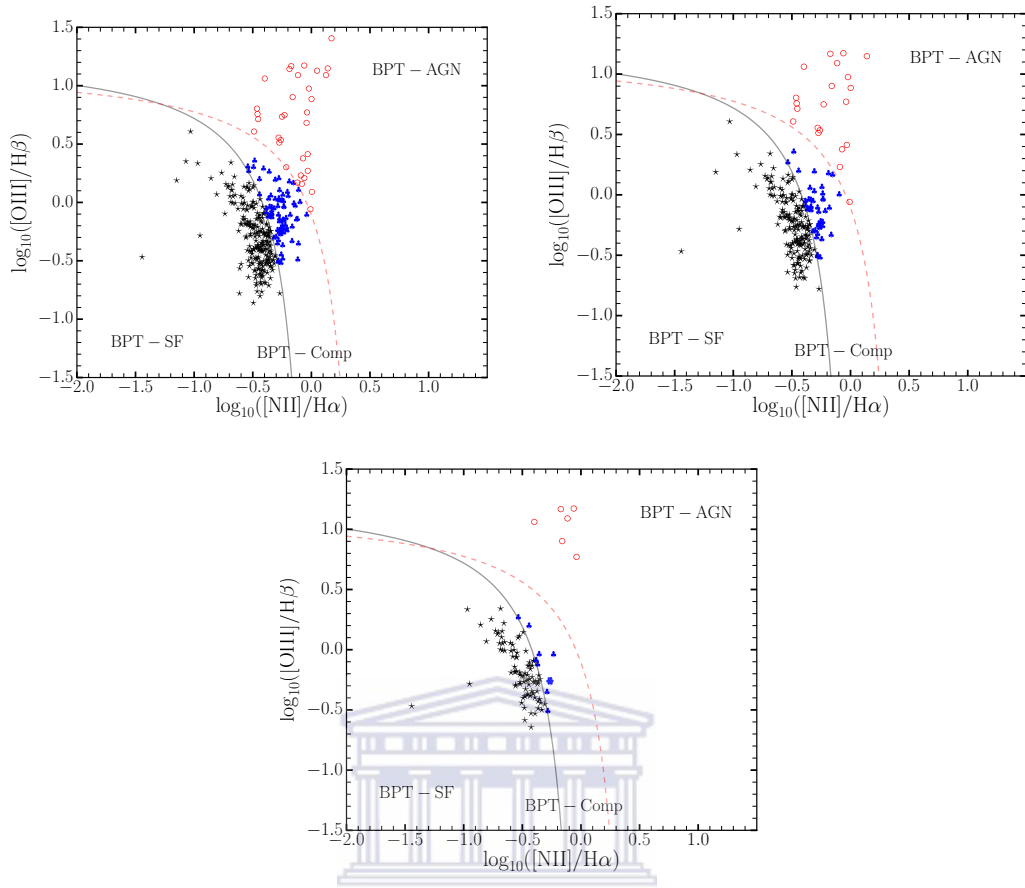


FIGURE B.3: BPT-NII diagram (GMRT sources with [OIII], $H\beta$, [NII], $H\alpha$ detections). The black stars represents the BPT-SF classification, blue clubsuits represents BPT-Comp (dominated by seyferts/starforming galaxies.) and the red open circles represents the BPT-AGN classifications. The [Kauffmann *et al.* \(2003\)](#) empirical and [Kewley *et al.* \(2001\)](#) theoretical divisions are plotted to separate the sources. The top left, top right and bottom plots indicates an SNR cut of 3, 5 and 10 respectively.

Figure B.4 presents an illustration of this whereby the equivalent width (EW) of the [N II] emission line is plotted against the ratio $[N II]/H\alpha$ for galaxies in our GMRT sample with these line detections shown as grey circles. The dash vertical red line indicates $\log_{10}([N II]/H\alpha) \geq -0.2$, where sources beyond this line (to the right of the line) are classified as AGNs according to this two line diagnostic ($\log_{10}([N II]/H\alpha)$). The BPT-SF (black stars), BPT-AGN (open red circles) and the BPT-Comp (blue clubsuit) are over-plotted for comparison. The top left, top right and bottom plots in this Figure B.4 indicates an SNR cut of 3, 5 and 10 respectively.

Figure B.5 presents the ratio of $[O III]/H\beta$ plotted against the equivalent width of the [O III] emission line for galaxies in our GMRT sample with these line detections (grey circles). The dash horizontal red line indicates $\log_{10}([O III]/H\beta) \geq 0.8$, where sources above this line are classified as AGNs according to this two line diagnostic ($\log_{10}([O III]/H\beta)$). The BPT-SF (black stars), BPT-AGN (open red circles) and the

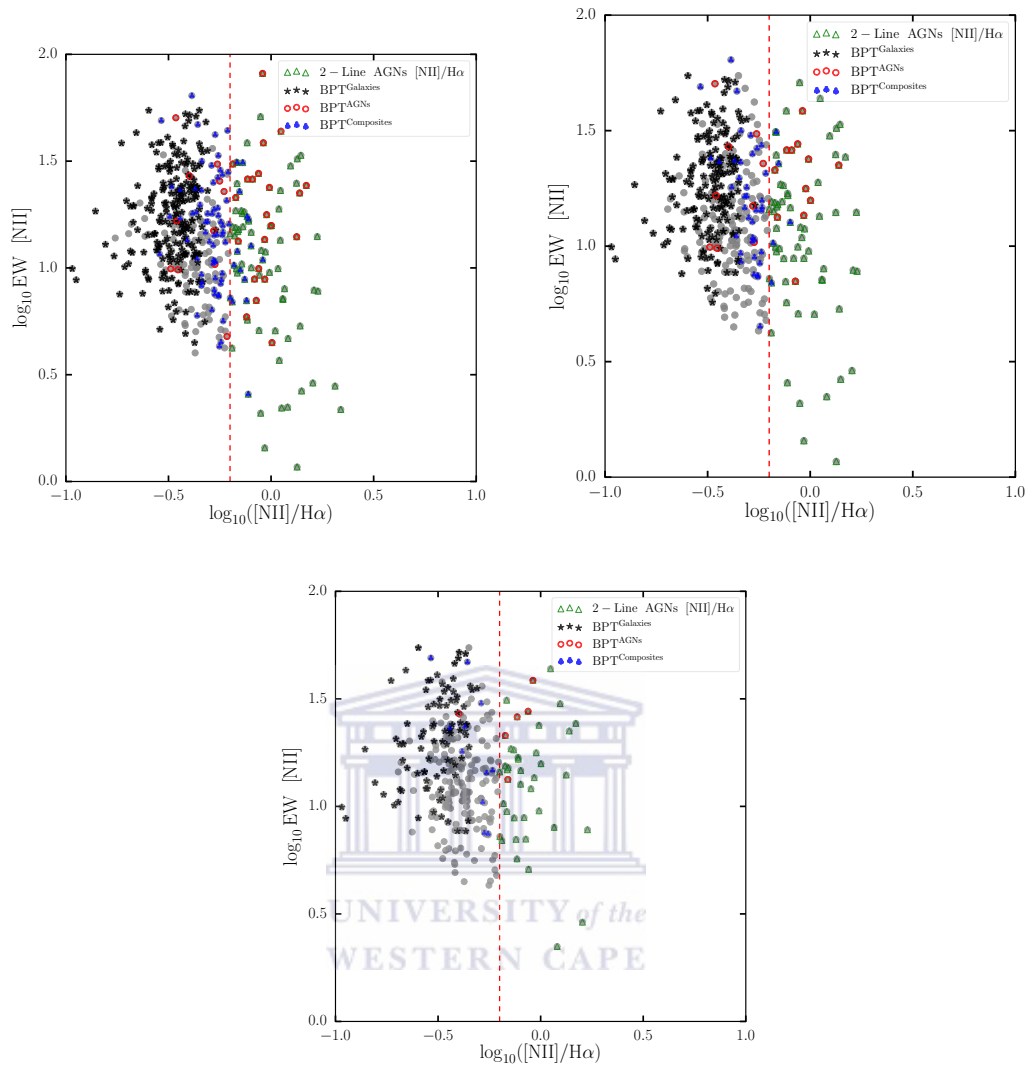


FIGURE B.4: Same as Figure 3.28. The top left, top right and bottom plots indicates an SNR cut of 3, 5 and 10 respectively.

BPT-Comp (blue clubsuit) are also over-plotted for comparison. The top left, top right and bottom plots in this Figure B.5 indicates an SNR cut of 3, 5 and 10 respectively.

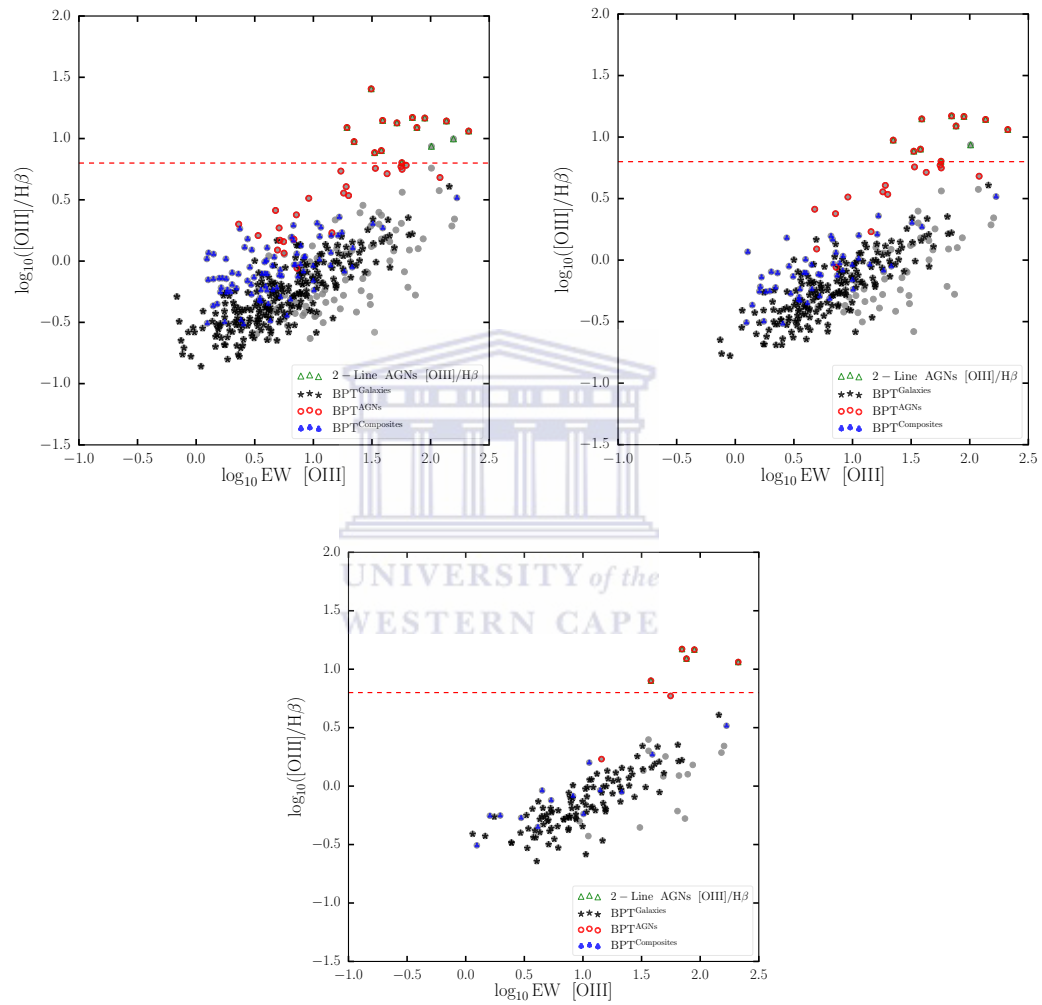


FIGURE B.5: Same as Figure 3.29. The top left, top right and bottom plots indicates an SNR cut of 3, 5 and 10 respectively.

Appendix C

Nature of the faint radio sources

C.0.2 Binning in radio luminosity

The right panel of Figure C.1 shows q_{IR} versus redshift for our selected star-forming galaxies, split into four log-spaced bins of $L_{1.4\text{GHz}}$ with the median values of q_{IR} in each panel shown. Figure C.1 considers all sources classified as AGNs and SFGs according to our combined multi-wavelength classification except that the MIR criterion satisfies the Lacy Wedge. The grey regions in the left panel of Figure C.1 shows the various binning ranges both in the vertical and horizontal axes whereas the number of SFGs residing in each range is printed at the bottom.

The right panel of Figure C.2 shows q_{IR} versus redshift for our selected star-forming galaxies, split into four log-spaced bins of $L_{1.4\text{GHz}}$ with the median values of q_{IR} in each panel shown. Figure C.2 considers all sources classified as AGNs and SFGs according to our combined multi-wavelength classification except that the MIR criterion satisfies the Stern Wedge. The grey regions in the left panel of Figure C.2 shows the various binning ranges both in the vertical and horizontal axes whereas the number of SFGs residing in each range is printed at the bottom.

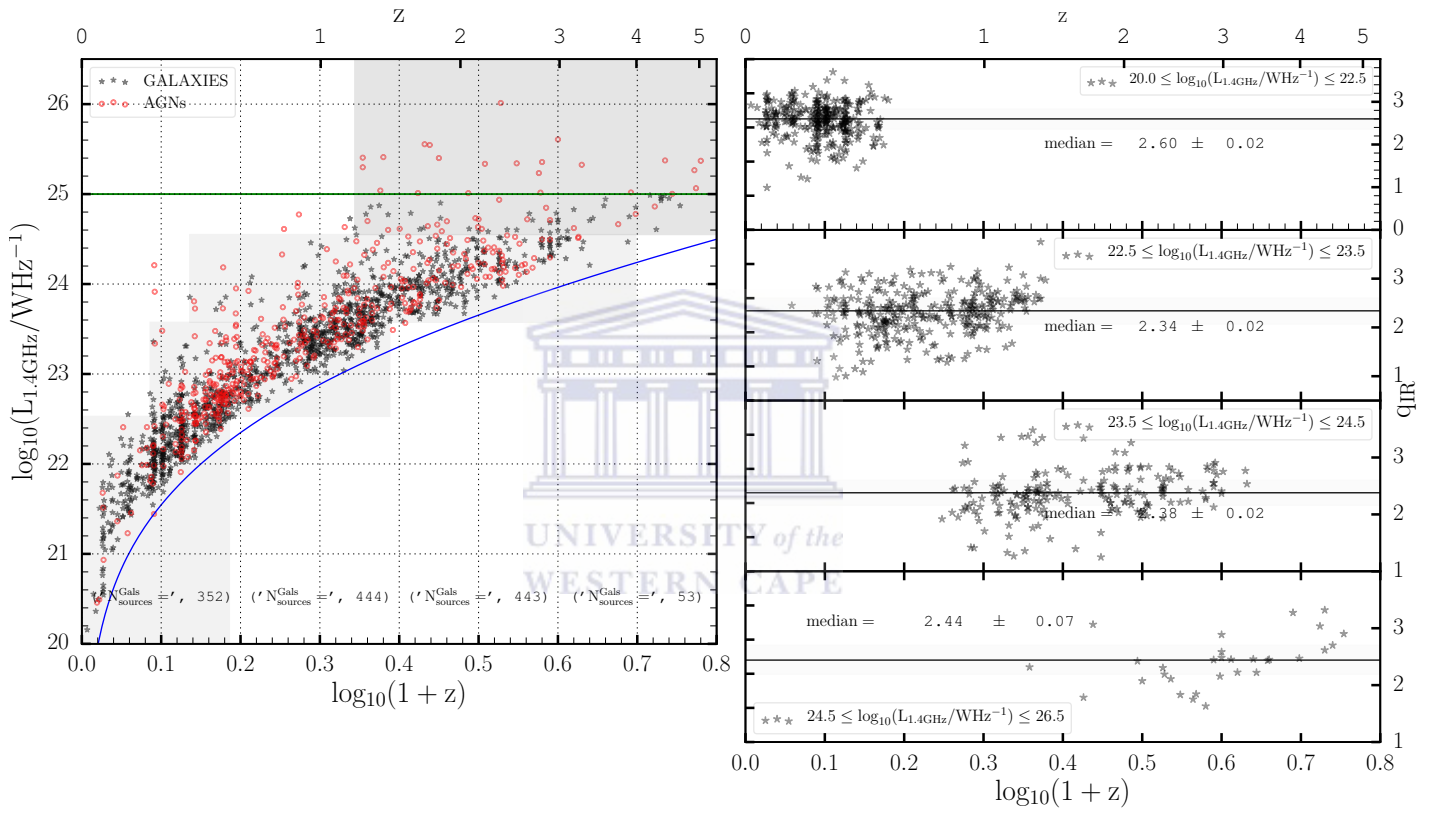


FIGURE C.1: Same as Figure 4.6. Considering all sources classified as AGNs and SFGs according to our combined multi-wavelength classification satisfying the Lacy Wedge with respect to the MIR.

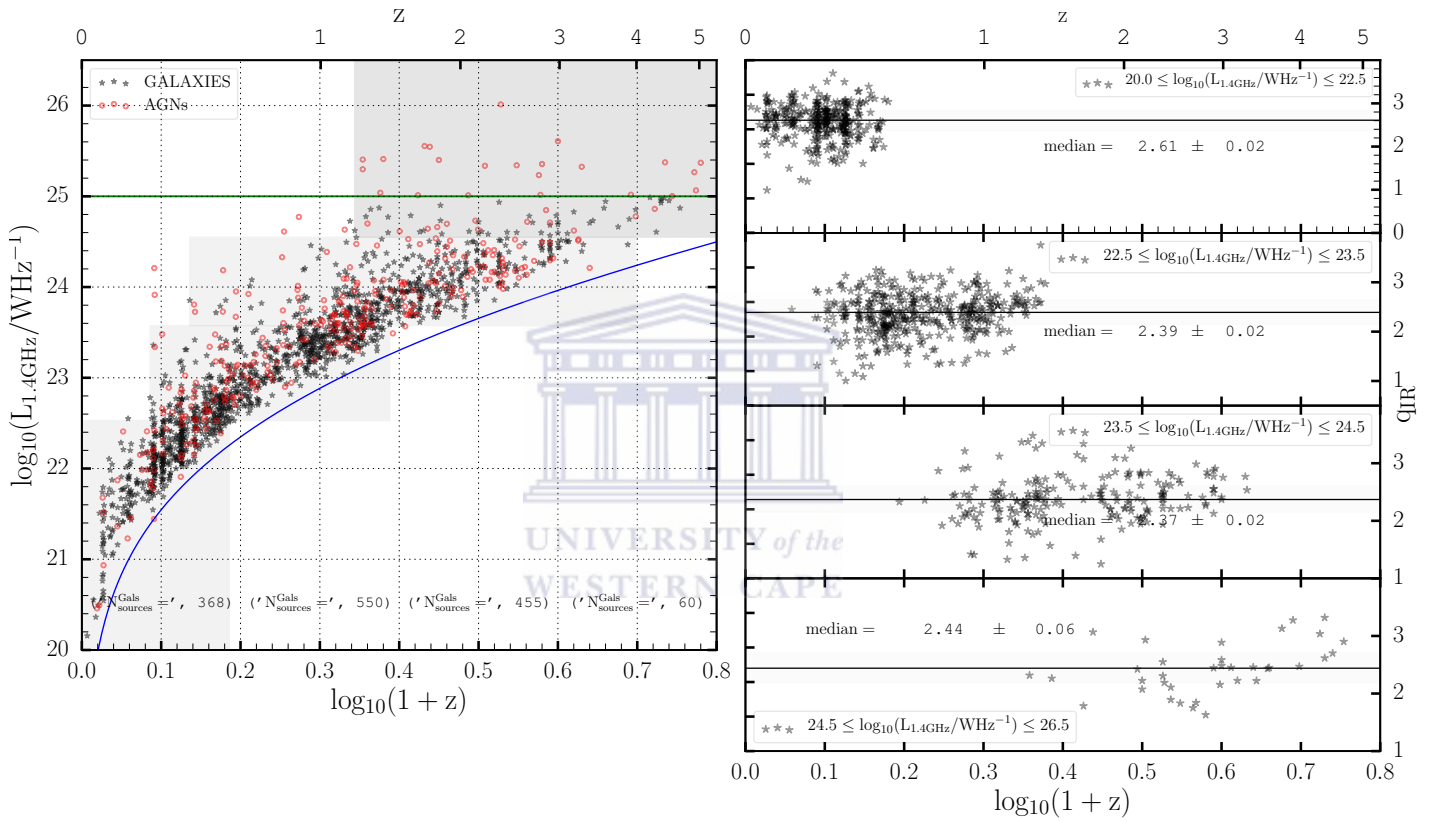


FIGURE C.2: Same as Figure 4.6. Considering all sources classified as AGNs and SFGs according to our combined multi-wavelength classification satisfying the Stern Wedge with respect to the MIR.

C.0.3 Binning in infrared luminosity

Figure C.3 shows the q_{IR} parameter as a function of redshift, also split into into four log-spaced bins of far-infrared luminosity. Similarly, the grey regions in the left panel of Figure C.3 shows the various binning ranges both in the vertical and horizontal axes whereas the number of SFGs residing in each range is printed at the bottom. Figure C.3 considers all sources classified as AGNs and SFGs according to our combined multi-wavelength classification except that the MIR criterion satisfies the Lacy Wedge.

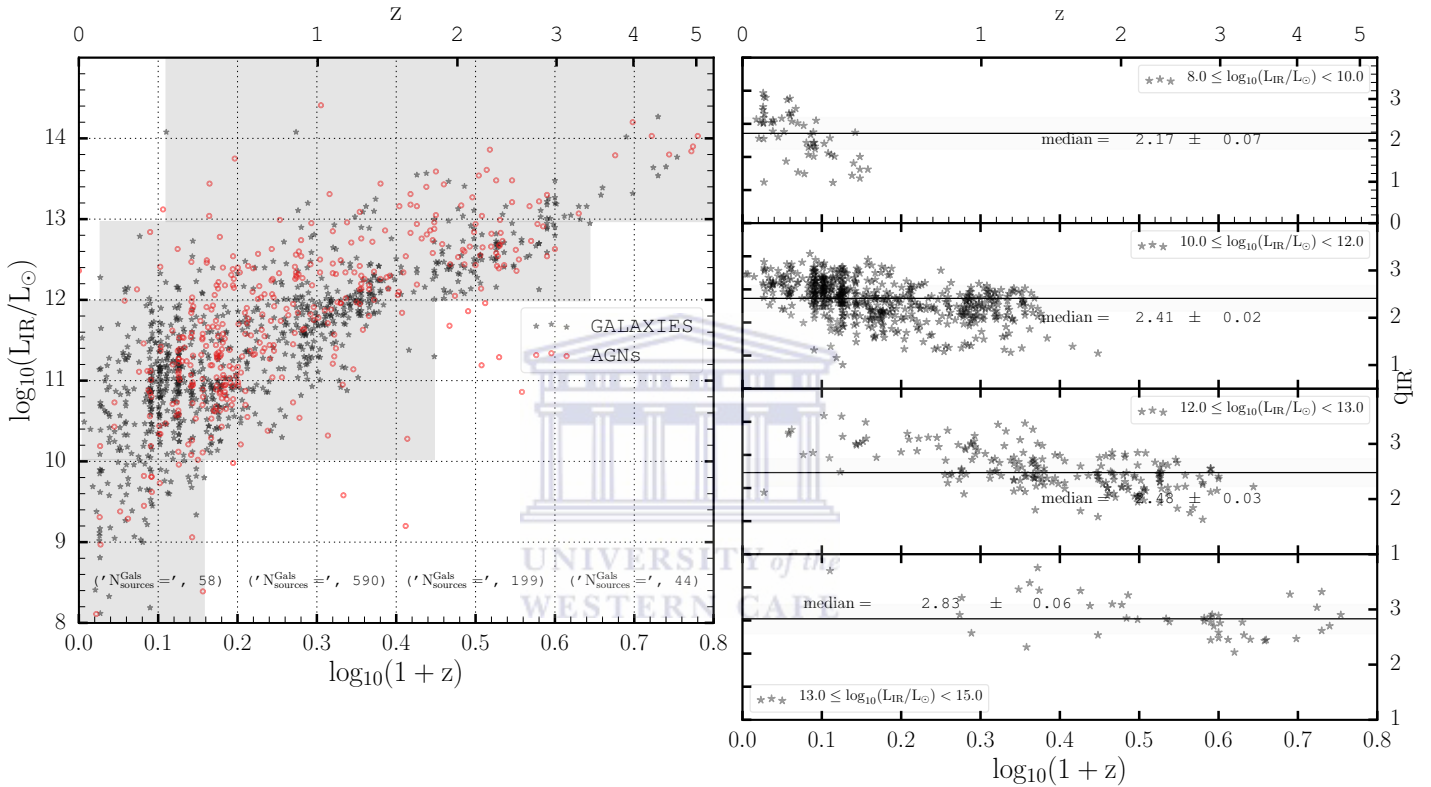


FIGURE C.3: Same as Figure 4.7. Considering all sources classified as AGNs and SFGs according to our combined multi-wavelength classification satisfying the Lacy Wedge with respect to the MIR

Figure C.4 shows the q_{IR} parameter as a function of redshift, also split into into four log-spaced bins of far-infrared luminosity. Similarly, the grey regions in the left panel of Figure C.4 shows the various binning ranges both in the vertical and horizontal axes whereas the number of SFGs residing in each range is printed at the bottom. Figure C.4 considers all sources classified as AGNs and SFGs according to our combined multi-wavelength classification except that the MIR criterion satisfies the Stern Wedge.

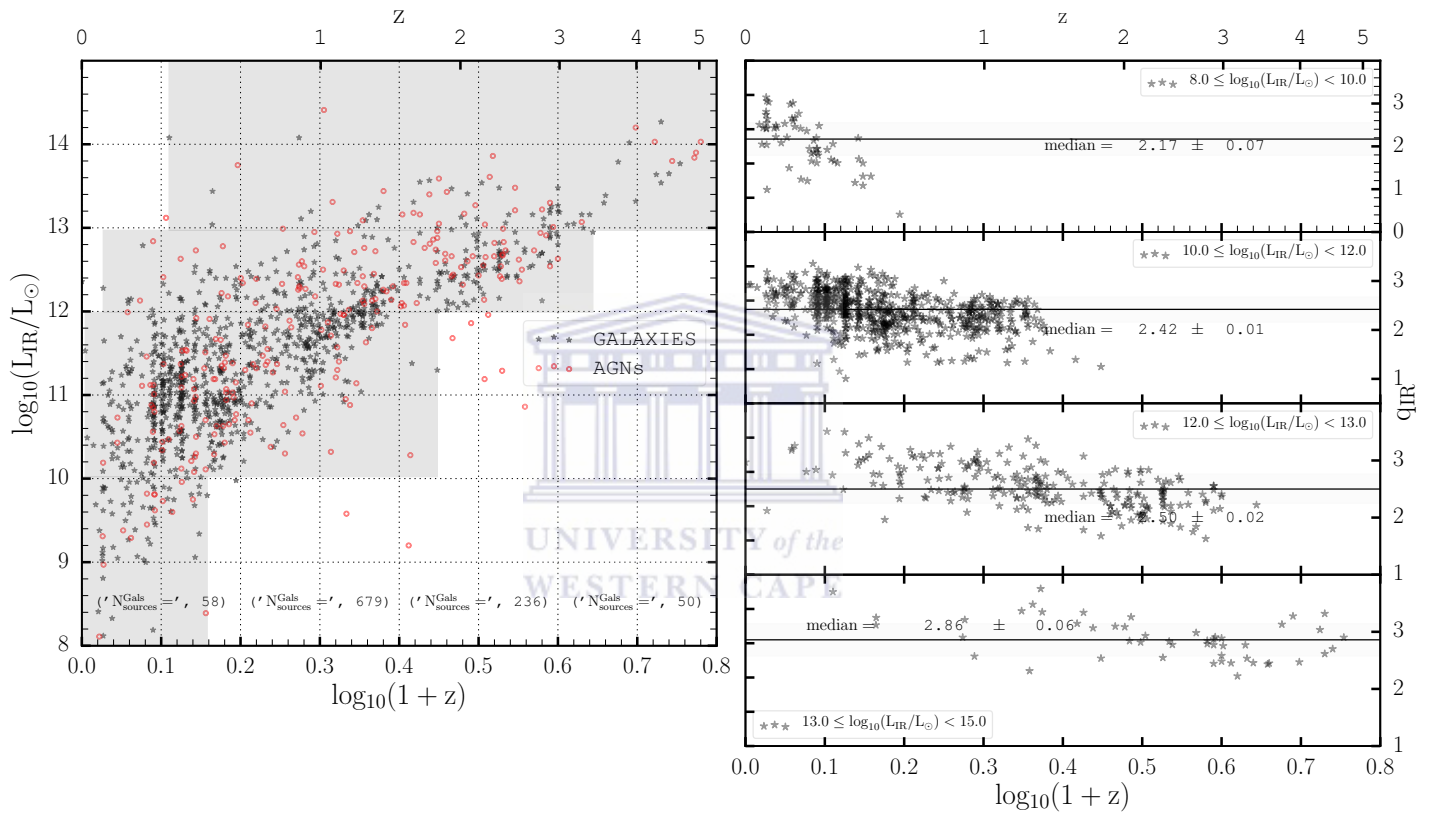


FIGURE C.4: Same as Figure 4.7. Considering all sources classified as AGNs and SFGs according to our combined multi-wavelength classification satisfying the Stern Wedge with respect to the MIR.

Bibliography

- Alam, S., Albareti, F. D., Allende Prieto, C., Anders, F., Anderson, S. F., Anderton, T., Andrews, B. H., Armengaud, E., Aubourg, É., Bailey, S., and et al. (2015). The Eleventh and Twelfth Data Releases of the Sloan Digital Sky Survey: Final Data from SDSS-III. *ApJS*, **219**, 12.
- Alexander, D. M., Bauer, F. E., Brandt, W. N., Garmire, G. P., Hornschemeier, A. E., Schneider, D. P., and Vignali, C. (2003). Resolving the source populations that contribute to the X-ray background: The 2 Ms Chandra Deep Field-North Survey. *Astronomische Nachrichten*, **324**, 8–11.
- Antonucci, R. (1993). Unified models for active galactic nuclei and quasars. *ARA&A*, **31**, 473–521.
- Appleton, P. N., Fadda, D. T., Marleau, F. R., Frayer, D. T., Helou, G., Condon, J. J., Choi, P. I., Yan, L., Lacy, M., Wilson, G., Armus, L., Chapman, S. C., Fang, F., Heinrichson, I., Im, M., Jannuzi, B. T., Storrie-Lombardi, L. J., Shupe, D., Soifer, B. T., Squires, G., and Teplitz, H. I. (2004). The Far- and Mid-Infrared/Radio Correlations in the Spitzer Extragalactic First Look Survey. *ApJS*, **154**, 147–150.
- Baldry, I. K., Balogh, M. L., Bower, R., Glazebrook, K., and Nichol, R. C. (2004). Color bimodality: Implications for galaxy evolution. In R. E. Allen, D. V. Nanopoulos, and C. N. Pope, editors, *The New Cosmology: Conference on Strings and Cosmology*, volume 743 of *American Institute of Physics Conference Series*, pages 106–119.
- Baldwin, J. A., Phillips, M. M., and Terlevich, R. (1981). Classification parameters for the emission-line spectra of extragalactic objects. *PASP*, **93**, 5–19.
- Baran, A., Fiege, J., Taylor, A. R., Foster, T., and Landecker, T. L. (2010). Measuring the Diffuse Polarized Foreground of the ELAIS-N1 Deep Field. In R. Kothes, T. L. Landecker, and A. G. Willis, editors, *Astronomical Society of the Pacific Conference Series*, volume 438 of *Astronomical Society of the Pacific Conference Series*, page 303.
- Bell, E. F. (2003). Estimating Star Formation Rates from Infrared and Radio Luminosities: The Origin of the Radio-Infrared Correlation. *ApJ*, **586**, 794–813.

- Bolton, A. S., Schlegel, D. J., Aubourg, É., Bailey, S., Bhardwaj, V., Brownstein, J. R., Burles, S., Chen, Y.-M., Dawson, K., Eisenstein, D. J., Gunn, J. E., Knapp, G. R., Loomis, C. P., Lupton, R. H., Maraston, C., Muna, D., Myers, A. D., Olmstead, M. D., Padmanabhan, N., Pâris, I., Percival, W. J., Petitjean, P., Rockosi, C. M., Ross, N. P., Schneider, D. P., Shu, Y., Strauss, M. A., Thomas, D., Tremonti, C. A., Wake, D. A., Weaver, B. A., and Wood-Vasey, W. M. (2012). Spectral Classification and Redshift Measurement for the SDSS-III Baryon Oscillation Spectroscopic Survey. *AJ*, **144**, 144.
- Bonzini, M., Padovani, P., Mainieri, V., Kellermann, K. I., Miller, N., Rosati, P., Tozzi, P., and Vattakunnel, S. (2013). The sub-mJy radio sky in the Extended Chandra Deep Field-South: source population. *MNRAS*, **436**, 3759–3771.
- Bourne, N., Dunne, L., Ivison, R. J., Maddox, S. J., Dickinson, M., and Frayer, D. T. (2011). Evolution of the far-infrared-radio correlation and infrared spectral energy distributions of massive galaxies over $z=0-2$. *MNRAS*, **410**, 1155–1173.
- Boyle, B. J., Cornwell, T. J., Middelberg, E., Norris, R. P., Appleton, P. N., and Smail, I. (2007). Extending the infrared radio correlation. *MNRAS*, **376**, 1182–1188.
- Brusa, M., Comastri, A., Gilli, R., Hasinger, G., Iwasawa, K., Mainieri, V., Mignoli, M., Salvato, M., Zamorani, G., Bongiorno, A., Cappelluti, N., Civano, F., Fiore, F., Merloni, A., Silverman, J., Trump, J., Vignali, C., Capak, P., Elvis, M., Ilbert, O., Impey, C., and Lilly, S. (2009). High-Redshift Quasars in the COSMOS Survey: The Space Density of $z \geq 3$ X-Ray Selected QSOs. *ApJ*, **693**, 8–22.
- Calzetti, D., Wu, S.-Y., Hong, S., Kennicutt, R. C., Lee, J. C., Dale, D. A., Engelbracht, C. W., van Zee, L., Draine, B. T., Hao, C.-N., Gordon, K. D., Moustakas, J., Murphy, E. J., Regan, M., Begum, A., Block, M., Dalcanton, J., Funes, J., Gil de Paz, A., Johnson, B., Sakai, S., Skillman, E., Walter, F., Weisz, D., Williams, B., and Wu, Y. (2010). The Calibration of Monochromatic Far-Infrared Star Formation Rate Indicators. *ApJ*, **714**, 1256–1279.
- Cesarsky, C. J., Abergel, A., Agnese, P., Altieri, B., Augeres, J. L., Aussel, H., Biviano, A., Blommaert, J., Bonnal, J. F., Bortoletto, F., Boulade, O., Boulanger, F., Cazes, S., Cesarsky, D. A., Chedin, A., Claret, A., Combes, M., Cretolle, J., Davies, J. K., Desert, F. X., Elbaz, D., Engelmann, J. J., Epstein, G., Franceschini, A., Gallais, P., Gastaud, R., Gorisse, M., Guest, S., Hawarden, T., Imbault, D., Kleczewski, M., Lacombe, F., Landriu, D., Lapegue, J., Lena, P., Longair, M. S., Mandolesi, R., Metcalfe, L., Mosquet, N., Nordh, L., Okumura, K., Ott, S., Perault, M., Perrier, F., Persi, P., Puget, P., Purkins, T., Rio, Y., Robert, T., Rouan, D., Roy, A., Saint-Pe, O., Sam Lone, J., Sargent, A., Sauvage, M., Sibille, F., Siebenmorgen, R., Sirou, F.,

- Soufflot, A., Starck, J. L., Tiphene, D., Tran, D., Ventura, G., Vigroux, L., Vivares, F., and Wade, R. (1996). ISOCAM in flight. *A&A*, **315**, L32–L37.
- Chapman, S., Blain, A., Ivison, R., and Smail, I. (2005). Mid-IR spectroscopy of suspected very hot dusty, high- z galaxies. Spitzer Proposal.
- Chapman, S. C., Barger, A. J., Cowie, L. L., Scott, D., Borys, C., Capak, P., Fomalont, E. B., Lewis, G. F., Richards, E. A., Steffen, A. T., Wilson, G., and Yun, M. (2003). The Properties of Microjansky Radio Sources in the Hubble Deep Field-North, SSA 13, and SSA 22 Fields. *ApJ*, **585**, 57–66.
- Ciliegi, P., McMahon, R. G., Miley, G., Gruppioni, C., Rowan-Robinson, M., Cesarsky, C., Danese, L., Franceschini, A., Genzel, R., Lawrence, A., Lemke, D., Oliver, S., Puget, J.-L., and Rocca-Volmerange, B. (1999). A deep VLA survey at 20 CM of the ISO ELAIS survey regions. *MNRAS*, **302**, 222–244.
- Cole, S., Percival, W. J., Peacock, J. A., Norberg, P., Baugh, C. M., Frenk, C. S., Baldry, I., Bland-Hawthorn, J., Bridges, T., Cannon, R., Colless, M., Collins, C., Couch, W., Cross, N. J. G., Dalton, G., Eke, V. R., De Propris, R., Driver, S. P., Efstathiou, G., Ellis, R. S., Glazebrook, K., Jackson, C., Jenkins, A., Lahav, O., Lewis, I., Lumsden, S., Maddox, S., Madgwick, D., Peterson, B. A., Sutherland, W., and Taylor, K. (2005). The 2dF Galaxy Redshift Survey: power-spectrum analysis of the final data set and cosmological implications. *MNRAS*, **362**, 505–534.
- Condon, J. J. (1984). Cosmological evolution of radio sources. *ApJ*, **287**, 461–474.
- Condon, J. J. (1992a). Far-Infrared and Radio Signatures of Starbursts and Monster. In S. S. Holt, S. G. Neff, and C. M. Urry, editors, *American Institute of Physics Conference Series*, volume 254 of *American Institute of Physics Conference Series*, pages 629–639.
- Condon, J. J. (1992b). Radio emission from normal galaxies. *ARA&A*, **30**, 575–611.
- Dadina, M. (2008). Seyfert galaxies in the local Universe ($z \leq 0.1$): the average X-ray spectrum as seen by BeppoSAX. *A&A*, **485**, 417–424.
- Dawson, K. S., Schlegel, D. J., Ahn, C. P., Anderson, S. F., Aubourg, É., Bailey, S., Barkhouser, R. H., Bautista, J. E., Beifiori, A., Berlind, A. A., *et al.* (2013). The baryon oscillation spectroscopic survey of sdss-iii. *The Astronomical Journal*, **145**(1), 10.
- Di Matteo, T., Springel, V., and Hernquist, L. (2005). Energy input from quasars regulates the growth and activity of black holes and their host galaxies. *Nature*, **433**, 604–607.

- Donley, J. L., Rieke, G. H., Pérez-González, P. G., Rigby, J. R., and Alonso-Herrero, A. (2007). Detecting Obscured AGN in the Distant Universe with Spitzer. In J. Afonso, H. C. Ferguson, B. Mobasher, and R. Norris, editors, *Deepest Astronomical Surveys*, volume 380 of *Astronomical Society of the Pacific Conference Series*, page 119.
- Donley, J. L., Rieke, G. H., Alexander, D. M., Egami, E., and Pérez-González, P. G. (2010). The AGN, Star-forming, and Morphological Properties of Luminous IR-bright/optically-faint Galaxies. *ApJ*, **719**, 1393–1407.
- Donley, J. L., Koekemoer, A. M., Brusa, M., Capak, P., Cardamone, C. N., Civano, F., Ilbert, O., Impey, C. D., Kartaltepe, J. S., Miyaji, T., Salvato, M., Sanders, D. B., Trump, J. R., and Zamorani, G. (2012). Identifying Luminous Active Galactic Nuclei in Deep Surveys: Revised IRAC Selection Criteria. *ApJ*, **748**, 142.
- Dopita, M. A., Kewley, L. J., Heisler, C. A., and Sutherland, R. S. (2000). A Theoretical Recalibration of the Extragalactic H II Region Sequence. *ApJ*, **542**, 224–234.
- Eisenstein, D. J., Zehavi, I., Hogg, D. W., Scoccimarro, R., Blanton, M. R., Nichol, R. C., Scranton, R., Seo, H.-J., Tegmark, M., Zheng, Z., Anderson, S. F., Annis, J., Bahcall, N., Brinkmann, J., Burles, S., Castander, F. J., Connolly, A., Csabai, I., Doi, M., Fukugita, M., Frieman, J. A., Glazebrook, K., Gunn, J. E., Hendry, J. S., Hennessy, G., Ivezić, Z., Kent, S., Knapp, G. R., Lin, H., Loh, Y.-S., Lupton, R. H., Margon, B., McKay, T. A., Meiksin, A., Munn, J. A., Pope, A., Richmond, M. W., Schlegel, D., Schneider, D. P., Shimasaku, K., Stoughton, C., Strauss, M. A., SubbaRao, M., Szalay, A. S., Szapudi, I., Tucker, D. L., Yanny, B., and York, D. G. (2005). Detection of the Baryon Acoustic Peak in the Large-Scale Correlation Function of SDSS Luminous Red Galaxies. *ApJ*, **633**, 560–574.
- Eisenstein, D. J., Weinberg, D. H., Agol, E., Aihara, H., Allende Prieto, C., Anderson, S. F., Arns, J. A., Aubourg, É., Bailey, S., Balbinot, E., and et al. (2011). SDSS-III: Massive Spectroscopic Surveys of the Distant Universe, the Milky Way, and Extra-Solar Planetary Systems. *AJ*, **142**, 72.
- Evans, D. A., Worrall, D. M., Hardcastle, M. J., Kraft, R. P., and Birkinshaw, M. (2006). Chandra and XMM-Newton Observations of a Sample of Low-Redshift FR I and FR II Radio Galaxy Nuclei. *ApJ*, **642**, 96–112.
- Fabbiano, G. (1989). X-Ray Emission and Extranuclear Activity in Galaxies. In E. J. A. Meurs and R. A. E. Fosbury, editors, *European Southern Observatory Conference and Workshop Proceedings*, volume 32 of *European Southern Observatory Conference and Workshop Proceedings*, page 325.

- Fazio, G., Huang, J., Im, M., and Lacy, M. (2004). IRAC Imaging of a Cluster of Galaxies at $z=2.39$ and Extremely Red Objects. Spitzer Proposal.
- Ferrarese, L. and Merritt, D. (2000). A Fundamental Relation between Supermassive Black Holes and Their Host Galaxies. *ApJ*, **539**, L9–L12.
- Fomalont, E. B., Kellermann, K. I., Wall, J. V., and Weistrop, D. (1984). A deep 6-centimeter radio source survey. *Science*, **225**, 23–28.
- Förster Schreiber, N. M. (2000). Moderate-Resolution Near-Infrared Spectroscopy of Cool Stars: A New K-Band Library. *AJ*, **120**, 2089–2100.
- Garn, T. and Alexander, P. (2008). Deep 610-MHz Giant Metrewave Radio Telescope observations of the Spitzer extragalactic First Look Survey field - III. The radio properties of infrared-faint radio sources. *MNRAS*, **391**, 1000–1008.
- Garn, T. and Alexander, P. (2009). Radio source stacking and the infrared/radio correlation at μJy flux densities. *MNRAS*, **394**, 105–116.
- Gebhardt, K., Bender, R., Bower, G., Dressler, A., Faber, S. M., Filippenko, A. V., Green, R., Grillmair, C., Ho, L. C., Kormendy, J., Lauer, T. R., Magorrian, J., Pinkney, J., Richstone, D., and Tremaine, S. (2000). A Relationship between Nuclear Black Hole Mass and Galaxy Velocity Dispersion. *ApJ*, **539**, L13–L16.
- Genzel, R., Newman, S., Jones, T., Förster Schreiber, N. M., Shapiro, K., Genel, S., Lilly, S. J., Renzini, A., Tacconi, L. J., Bouché, N., Burkert, A., Cresci, G., Buschkamp, P., Carollo, C. M., Ceverino, D., Davies, R., Dekel, A., Eisenhauer, F., Hicks, E., Kurk, J., Lutz, D., Mancini, C., Naab, T., Peng, Y., Sternberg, A., Vergani, D., and Zamorani, G. (2011). The Sins Survey of $z \sim 2$ Galaxy Kinematics: Properties of the Giant Star-forming Clumps. *ApJ*, **733**, 101.
- Georgakakis, A., Nandra, K., Laird, E. S., Aird, J., and Trichas, M. (2008). A new method for determining the sensitivity of X-ray imaging observations and the X-ray number counts. *MNRAS*, **388**, 1205–1213.
- Giacconi, R., Zirm, A., Wang, J., Rosati, P., Nonino, M., Tozzi, P., Gilli, R., Mainieri, V., Hasinger, G., Kewley, L., Bergeron, J., Borgani, S., Gilmozzi, R., Grogin, N., Koekemoer, A., Schreier, E., Zheng, W., and Norman, C. (2002). Chandra Deep Field South: The 1 Ms Catalog. *ApJS*, **139**, 369–410.
- Giroletti, M. and Panessa, F. (2009). The Faintest Seyfert Radio Cores Revealed by VLBI. *ApJ*, **706**, L260–L264.

- Gonzalez-Solares, E. A., Oliver, S., Gruppioni, C., Pozzi, F., Lari, C., Rowan-Robinson, M., Serjeant, S., La Franca, F., and Vaccari, M. (2004). Large-scale structure in the ELAIS S1 Survey. *MNRAS*, **352**, 44–48.
- González-Solares, E. A., Irwin, M., McMahon, R. G., Hodgkin, S., Lewis, J. R., Walton, N. A., Jarvis, M., Marchetti, L., Oliver, S., Pérez-Fournon, I., Siana, B., Surace, J., and Vaccari, M. (2011). Wide-field optical imaging on ELAIS N1, ELAIS N2, First Look Survey and Lockman Hole: observations and source catalogues. *MNRAS*, **416**, 927–940.
- Hardcastle, M. J., Kraft, R. P., Worrall, D. M., Croston, J. H., Evans, D. A., Birkinshaw, M., and Murray, S. S. (2007). The Interaction between Radio Lobes and Hot Gas in the Nearby Radio Galaxies 3C 285 and 3C 442A. *ApJ*, **662**, 166–181.
- Hasinger, G. (2004). The X-ray background and AGNs. *Nuclear Physics B Proceedings Supplements*, **132**, 86–96.
- Helou, G., Soifer, B. T., and Rowan-Robinson, M. (1985). Thermal infrared and non-thermal radio - Remarkable correlation in disks of galaxies. *ApJ*, **298**, L7–L11.
- Hogg, D. W., Blanton, M. R., and Eisenstein, D. J. (2002). The overdensities of galaxy environments as a function of luminosity and color. In *American Astronomical Society Meeting Abstracts*, volume 35 of *Bulletin of the American Astronomical Society*, page 148.04.
- Hopkins, A. M., McClure-Griffiths, N. M., and Gaensler, B. M. (2008). Linked Evolution of Gas and Star Formation in Galaxies Over Cosmic History. *ApJ*, **682**, L13–L16.
- Huynh, M. T., Jackson, C. A., Norris, R. P., and Fernandez-Soto, A. (2008). Radio Observations of the Hubble Deep Field-South Region. Iv. Optical Properties of the Faint Radio Population. *AJ*, **135**, 2470–2495.
- Hwang, H. S., Elbaz, D., Magdis, G., Daddi, E., Symeonidis, M., Altieri, B., Amblard, A., Andreani, P., Arumugam, V., Auld, R., Aussel, H., Babbedge, T., Berta, S., Blain, A., Bock, J., Bongiovanni, A., Boselli, A., Buat, V., Burgarella, D., Castro-Rodríguez, N., Cava, A., Cepa, J., Chanical, P., Chapin, E., Chary, R.-R., Cimatti, A., Clements, D. L., Conley, A., Conversi, L., Cooray, A., Dannerbauer, H., Dickinson, M., Dominguez, H., Dowell, C. D., Dunlop, J. S., Dwek, E., Eales, S., Farrah, D., Schreiber, N. F., Fox, M., Franceschini, A., Gear, W., Genzel, R., Glenn, J., Griffin, M., Gruppioni, C., Halpern, M., Hatziminaoglou, E., Ibar, E., Isaak, K., Ivison, R. J., Jeong, W.-S., Lagache, G., Le Borgne, D., Le Floc'h, E., Lee, H. M., Lee, J. C., Lee, M. G., Levenson, L., Lu, N., Lutz, D., Madden, S., Maffei, B., Magnelli, B., Mainetti, G., Maiolino, R., Marchetti, L., Mortier, A. M. J., Nguyen, H. T., Nordon,

- R., O'Halloran, B., Okumura, K., Oliver, S. J., Omont, A., Page, M. J., Panuzzo, P., Papageorgiou, A., Pearson, C. P., Pérez-Fournon, I., García, A. M. P., Poglitsch, A., Pohlen, M., Popesso, P., Pozzi, F., Rawlings, J. I., Rigopoulou, D., Riguccini, L., Rizzo, D., Rodighiero, G., Roseboom, I. G., Rowan-Robinson, M., Saintonge, A., Portal, M. S., Santini, P., Sauvage, M., Schulz, B., Scott, D., Seymour, N., Shao, L., Shupe, D. L., Smith, A. J., Stevens, J. A., Sturm, E., Tacconi, L., Trichas, M., Tugwell, K. E., Vaccari, M., Valtchanov, I., Vieira, J. D., Vigroux, L., Wang, L., Ward, R., Wright, G., Xu, C. K., and Zemcov, M. (2010). Evolution of dust temperature of galaxies through cosmic time as seen by Herschel. *MNRAS*, **409**, 75–82.
- Ibar, E., Ivison, R. J., Biggs, A. D., Lal, D. V., Best, P. N., and Green, D. A. (2009). Deep multi-frequency radio imaging in the Lockman Hole using the GMRT and VLA - I. The nature of the sub-mJy radio population. *MNRAS*, **397**, 281–298.
- Ibar, E., Ivison, R. J., Best, P. N., Coppin, K., Pope, A., Smail, I., and Dunlop, J. S. (2010). Deep multi-frequency radio imaging in the Lockman Hole - II. The spectral index of submillimetre galaxies. *MNRAS*, **401**, L53–L57.
- Ilbert, O., Salvato, M., Le Floch, E., Aussel, H., Capak, P., McCracken, H. J., Mobasher, B., Kartaltepe, J., Scoville, N., and Sanders, D. B. (2010). Galaxy stellar mass assembly between $0.2 < z < 2$ from the S-COSMOS survey. In S. Boissier, M. Heydari-Malayeri, R. Samadi, and D. Valls-Gabaud, editors, *SF2A-2010: Proceedings of the Annual meeting of the French Society of Astronomy and Astrophysics*, page 355.
- Ilbert, O., McCracken, H. J., Le Fèvre, O., Capak, P., Dunlop, J., Karim, A., Renzini, M. A., Caputi, K., Boissier, S., Arnouts, S., Aussel, H., Comparat, J., Guo, Q., Hudelot, P., Kartaltepe, J., Kneib, J. P., Krogager, J. K., Le Floch, E., Lilly, S., Mellier, Y., Milvang-Jensen, B., Moutard, T., Onodera, M., Richard, J., Salvato, M., Sanders, D. B., Scoville, N., Silverman, J. D., Taniguchi, Y., Tasca, L., Thomas, R., Toft, S., Tresse, L., Vergani, D., Wolk, M., and Zirm, A. (2013). Mass assembly in quiescent and star-forming galaxies since $z \sim 4$ from UltraVISTA. *A&A*, **556**, A55.
- Ivison, R. J., Alexander, D. M., Biggs, A. D., Brandt, W. N., Chapin, E. L., Coppin, K. E. K., Devlin, M. J., Dickinson, M., Dunlop, J., Dye, S., Eales, S. A., Frayer, D. T., Halpern, M., Hughes, D. H., Ibar, E., Kovács, A., Marsden, G., Moncelsi, L., Netterfield, C. B., Pascale, E., Patanchon, G., Rafferty, D. A., Rex, M., Schinnerer, E., Scott, D., Semisch, C., Smail, I., Swinbank, A. M., Truch, M. D. P., Tucker, G. S., Viero, M. P., Walter, F., Weiß, A., Wiebe, D. V., and Xue, Y. Q. (2010a). BLAST: the far-infrared/radio correlation in distant galaxies. *MNRAS*, **402**, 245–258.

- Iverson, R. J., Magnelli, B., Ibar, E., Andreani, P., Elbaz, D., Altieri, B., Amblard, A., Arumugam, V., Auld, R., Aussel, H., Babbedge, T., Berta, S., Blain, A., Bock, J., Bongiovanni, A., Boselli, A., Buat, V., Burgarella, D., Castro-Rodríguez, N., Cava, A., Cepa, J., Chanial, P., Cimatti, A., Cirasuolo, M., Clements, D. L., Conley, A., Conversi, L., Cooray, A., Daddi, E., Dominguez, H., Dowell, C. D., Dwek, E., Eales, S., Farrah, D., Förster Schreiber, N., Fox, M., Franceschini, A., Gear, W., Genzel, R., Glenn, J., Griffin, M., Gruppioni, C., Halpern, M., Hatziminaoglou, E., Isaak, K., Lagache, G., Levenson, L., Lu, N., Lutz, D., Madden, S., Maffei, B., Magdis, G., Mainetti, G., Maiolino, R., Marchetti, L., Morrison, G. E., Mortier, A. M. J., Nguyen, H. T., Nordon, R., O'Halloran, B., Oliver, S. J., Omont, A., Owen, F. N., Page, M. J., Panuzzo, P., Papageorgiou, A., Pearson, C. P., Pérez-Fournon, I., Pérez García, A. M., Poglitsch, A., Pohlen, M., Popesso, P., Pozzi, F., Rawlings, J. I., Raymond, G., Rigopoulou, D., Riguccini, L., Rizzo, D., Rodighiero, G., Roseboom, I. G., Rowan-Robinson, M., Saintonge, A., Sanchez Portal, M., Santini, P., Schulz, B., Scott, D., Seymour, N., Shao, L., Shupe, D. L., Smith, A. J., Stevens, J. A., Sturm, E., Symeonidis, M., Tacconi, L., Trichas, M., Tugwell, K. E., Vaccari, M., Valtchanov, I., Vieira, J., Vigroux, L., Wang, L., Ward, R., Wright, G., Xu, C. K., and Zemcov, M. (2010b). The far-infrared/radio correlation as probed by Herschel. *A&A*, **518**, L31.
- Jarvis, M. J. (2012). Multi-wavelength Extragalactic Surveys and the Role of MeerKAT and SALT. *African Skies*, **16**, 44.
- Jarvis, M. J., Smith, D. J. B., Bonfield, D. G., Hardcastle, M. J., Falder, J. T., Stevens, J. A., Iverson, R. J., Auld, R., Baes, M., Baldry, I. K., Bamford, S. P., Bourne, N., Buttiglione, S., Cava, A., Cooray, A., Dariush, A., de Zotti, G., Dunlop, J. S., Dunne, L., Dye, S., Eales, S., Fritz, J., Hill, D. T., Hopwood, R., Hughes, D. H., Ibar, E., Jones, D. H., Kelvin, L., Lawrence, A., Leeuw, L., Loveday, J., Maddox, S. J., Michałowski, M. J., Negrello, M., Norberg, P., Pohlen, M., Prescott, M., Rigby, E. E., Robotham, A., Rodighiero, G., Scott, D., Sharp, R., Temi, P., Thompson, M. A., van der Werf, P., van Kampen, E., Vlahakis, C., and White, G. (2010). Herschel-ATLAS: the far-infrared-radio correlation at $z < 0.5$. *MNRAS*, **409**, 92–101.
- Jiang, L., Fan, X., Ivezić, Ž., Richards, G. T., Schneider, D. P., Strauss, M. A., and Kelly, B. C. (2007). The Radio-Loud Fraction of Quasars is a Strong Function of Redshift and Optical Luminosity. *ApJ*, **656**, 680–690.
- Kartaltepe, J. (2010). Investigating the Starburst-AGN Connection at the Peak of Galaxy Assembly Using Luminous IR galaxies Identified by Herschel. Keck Observatory Archive NIRSPEC N097NS.

- Kauffmann, G., Heckman, T. M., Tremonti, C., Brinchmann, J., Charlot, S., White, S. D. M., Ridgway, S. E., Brinkmann, J., Fukugita, M., Hall, P. B., Ivezić, Ž., Richards, G. T., and Schneider, D. P. (2003). The host galaxies of active galactic nuclei. *MNRAS*, **346**, 1055–1077.
- Kewley, L. J., Dopita, M. A., Sutherland, R. S., Heisler, C. A., and Trevena, J. (2001). Theoretical Modeling of Starburst Galaxies. *ApJ*, **556**, 121–140.
- Kewley, L. J., Groves, B., Kauffmann, G., and Heckman, T. (2006). The host galaxies and classification of active galactic nuclei. *MNRAS*, **372**, 961–976.
- Kimball, A. E., Kellermann, K. I., Condon, J. J., Ivezić, Ž., and Perley, R. A. (2011). The Two-component Radio Luminosity Function of Quasi-stellar Objects: Star Formation and Active Galactic Nucleus. *ApJ*, **739**, L29.
- Koopmans, L. V. E., de Bruyn, A. G., Xanthopoulos, E., and Fassnacht, C. D. (2000). A time-delay determination from VLA light curves of the CLASS gravitational lens B1600+434. *A&A*, **356**, 391–402.
- Kormendy, J. and Ho, L. C. (2013). Coevolution (Or Not) of Supermassive Black Holes and Host Galaxies. *ARA&A*, **51**, 511–653.
- Kormendy, J., Bender, R., Evans, A. S., and Richstone, D. (1998). The Mass Distribution in the Elliptical Galaxy NGC 3377: Evidence for a $2 \times 10^8 M_{\odot}$ Black Hole. *AJ*, **115**, 1823–1839.
- Lacki, B. C. and Thompson, T. A. (2010). The Physics of the Far-infrared-Radio Correlation. II. Synchrotron Emission as a Star Formation Tracer in High-redshift Galaxies. *ApJ*, **717**, 196–208.
- Lacki, B. C., Thompson, T. A., and Quataert, E. (2010). The Physics of the Far-infrared-Radio Correlation. I. Calorimetry, Conspiracy, and Implications. *ApJ*, **717**, 1–28.
- Lacy, M., Storrie-Lombardi, L. J., Sajina, A., Appleton, P. N., Armus, L., Chapman, S. C., Choi, P. I., Fadda, D., Fang, F., Frayer, D. T., Heinrichsen, I., Helou, G., Im, M., Marleau, F. R., Masci, F., Shupe, D. L., Soifer, B. T., Surace, J., Teplitz, H. I., Wilson, G., and Yan, L. (2004). Obscured and Unobscured Active Galactic Nuclei in the Spitzer Space Telescope First Look Survey. *ApJS*, **154**, 166–169.
- Lacy, M., Sajina, A., and Canalizo, G. (2006). Mid-infrared selection of dusty AGN. In L. Armus and W. T. Reach, editors, *Astronomical Society of the Pacific Conference Series*, volume 357 of *Astronomical Society of the Pacific Conference Series*, page 255.

- Lacy, M., Sajina, A., Petric, A. O., Seymour, N., Canalizo, G., Ridgway, S. E., Armus, L., and Storrie-Lombardi, L. J. (2007). Large Amounts of Optically Obscured Star Formation in the Host Galaxies of Some Type 2 Quasars. *ApJ*, **669**, L61–L64.
- Lacy, M., Ridgway, S. E., Gates, E. L., Nielsen, D. M., Petric, A. O., Sajina, A., Urrutia, T., Cox Drews, S., Harrison, C., Seymour, N., and Storrie-Lombardi, L. J. (2013). The Spitzer Mid-infrared Active Galactic Nucleus Survey. I. Optical and Near-infrared Spectroscopy of Obscured Candidates and Normal Active Galactic Nuclei Selected in the Mid-infrared. *ApJS*, **208**, 24.
- Laird, E. S., Nandra, K., Georgakakis, A., Aird, J. A., Barmby, P., Conselice, C. J., Coil, A. L., Davis, M., Faber, S. M., Fazio, G. G., Guhathakurta, P., Koo, D. C., Sarajedini, V., and Willmer, C. N. A. (2009). AEGIS-X: Chandra deep survey (Laird+, 2009). *VizieR Online Data Catalog*, **218**, 102.
- Lamareille, F. (2010). Spectral classification of emission-line galaxies from the Sloan Digital Sky Survey. I. An improved classification for high-redshift galaxies. *A&A*, **509**, A53.
- Lamareille, F., Mouhcine, M., Contini, T., Lewis, I., and Maddox, S. (2004). The luminosity-metallicity relation in the local Universe from the 2dF Galaxy Redshift Survey. *MNRAS*, **350**, 396–406.
- Laurent, O., Mirabel, I. F., Charmandaris, V., Le Floch, E., Lutz, D., and Genzel, R. (2000). Searching for AGN signatures in Mid-IR Spectra: The case of NGC1068. The case of the prototypical Seyfert 2 galaxy NGC 1068. In A. Salama, M. F. Kessler, K. Leech, and B. Schulz, editors, *ISO Beyond the Peaks: The 2nd ISO Workshop on Analytical Spectroscopy*, volume 456 of *ESA Special Publication*, page 249.
- Lawrence, A., Warren, S. J., Almaini, O., Edge, A. C., Hambly, N. C., Jameson, R. F., Lucas, P., Casali, M., Adamson, A., Dye, S., Emerson, J. P., Foucaud, S., Hewett, P., Hirst, P., Hodgkin, S. T., Irwin, M. J., Lodieu, N., McMahon, R. G., Simpson, C., Smail, I., Mortlock, D., and Folger, M. (2007). The UKIRT Infrared Deep Sky Survey (UKIDSS). *MNRAS*, **379**, 1599–1617.
- Lemke, D. (1996). First results from the ISOPHOT instrument. In *American Astronomical Society Meeting Abstracts #188*, volume 28 of *Bulletin of the American Astronomical Society*, page 901.
- Lonsdale, C. J. (2005). SWIRE and SIRTf Surveys. In M. Colless, L. Staveley-Smith, and R. A. Stathakis, editors, *Maps of the Cosmos*, volume 216 of *IAU Symposium*, page 337.

- Lonsdale, C. J., Smith, H. E., Rowan-Robinson, M., Surace, J., Shupe, D., Xu, C., Oliver, S., Padgett, D., Fang, F., Conrow, T., Franceschini, A., Gautier, N., Griffin, M., Hacking, P., Masci, F., Morrison, G., O’Linger, J., Owen, F., Pérez-Fournon, I., Pierre, M., Puetter, R., Stacey, G., Castro, S., Del Carmen Polletta, M., Farrah, D., Jarrett, T., Frayer, D., Siana, B., Babbedge, T., Dye, S., Fox, M., Gonzalez-Solares, E., Salaman, M., Berta, S., Condon, J. J., Dole, H., and Serjeant, S. (2003). SWIRE: The SIRTf Wide-Area Infrared Extragalactic Survey. *Publications of the Astronomical Society of the Pacific*, **115**, 897–927.
- Magnelli, B., Lutz, D., Berta, S., Altieri, B., Andreani, P., Aussel, H., Castañeda, H., Cava, A., Cepa, J., Cimatti, A., Daddi, E., Dannerbauer, H., Dominguez, H., Elbaz, D., Förster Schreiber, N., Genzel, R., Grazian, A., Gruppioni, C., Magdis, G., Maiolino, R., Nordon, R., Pérez Fournon, I., Pérez García, I., Poglitsch, A., Popesso, P., Pozzi, F., Riguccini, L., Rodighiero, G., Saintonge, A., Santini, P., Sanchez-Portal, M., Shao, L., Sturm, E., Tacconi, L., Valtchanov, I., Wieprecht, E., and Wierorrek, E. (2010). Far-infrared properties of submillimeter and optically faint radio galaxies. *A&A*, **518**, L28.
- Mainieri, V., Hasinger, G., Cappelluti, N., Brusa, M., Brunner, H., Civano, F., Comastri, A., Elvis, M., Finoguenov, A., Fiore, F., Gilli, R., Lehmann, I., Silverman, J., Tasca, L., Vignali, C., Zamorani, G., Schinnerer, E., Impey, C., Trump, J., Lilly, S., Maier, C., Griffiths, R. E., Miyaji, T., Capak, P., Koekemoer, A., Scoville, N., Shopbell, P., and Taniguchi, Y. (2007). The XMM-Newton Wide-Field Survey in the COSMOS Field. IV. X-Ray Spectral Properties of Active Galactic Nuclei. *ApJS*, **172**, 368–382.
- Manners, J. C., Johnson, O., Almaini, O., Willott, C. J., Gonzalez-Solares, E., Lawrence, A., Mann, R. G., Perez-Fournon, I., Dunlop, J. S., McMahan, R. G., Oliver, S. J., Rowan-Robinson, M., and Serjeant, S. (2003). The ELAIS deep X-ray survey - I. Chandra source catalogue and first results. *MNRAS*, **343**, 293–305.
- Martinez-Manso, J., Gonzalez, A. H., Ashby, M., Stanford, S. A., Brodwin, M., and Holder, G. P. (2014). The Spitzer-South Pole Telescope Survey: Linking galaxies and haloes at $z=1.5$. In *American Astronomical Society Meeting Abstracts #223*, volume 223 of *American Astronomical Society Meeting Abstracts*, page 231.05.
- Massardi, M., Bonaldi, A., Negrello, M., Ricciardi, S., Raccanelli, A., and de Zotti, G. (2010). A model for the cosmological evolution of low-frequency radio sources. *MNRAS*, **404**, 532–544.
- Mauch, T. and Sadler, E. M. (2007). Radio sources in the 6dFGS: local luminosity functions at 1.4GHz for star-forming galaxies and radio-loud AGN. *MNRAS*, **375**, 931–950.

- Mauduit, J.-C., Lacy, M., Farrah, D., Surace, J. A., Jarvis, M., Oliver, S., Maraston, C., Vaccari, M., Marchetti, L., Zeimann, G., Gonzáles-Solares, E. A., Pforr, J., Petric, A. O., Henriques, B., Thomas, P. A., Afonso, J., Rettura, A., Wilson, G., Falder, J. T., Geach, J. E., Huynh, M., Norris, R. P., Seymour, N., Richards, G. T., Stanford, S. A., Alexander, D. M., Becker, R. H., Best, P. N., Bizzocchi, L., Bonfield, D., Castro, N., Cava, A., Chapman, S., Christopher, N., Clements, D. L., Covone, G., Dubois, N., Dunlop, J. S., Dyke, E., Edge, A., Ferguson, H. C., Foucaud, S., Franceschini, A., Gal, R. R., Grant, J. K., Grossi, M., Hatziminaoglou, E., Hickey, S., Hodge, J. A., Huang, J.-S., Ivison, R. J., Kim, M., LeFevre, O., Lehnert, M., Lonsdale, C. J., Lubin, L. M., McLure, R. J., Messias, H., Martínez-Sansigre, A., Mortier, A. M. J., Nielsen, D. M., Ouchi, M., Parish, G., Perez-Fournon, I., Pierre, M., Rawlings, S., Readhead, A., Ridgway, S. E., Rigopoulou, D., Romer, A. K., Rosebloom, I. G., Rottgering, H. J. A., Rowan-Robinson, M., Sajina, A., Simpson, C. J., Smail, I., Squires, G. K., Stevens, J. A., Taylor, R., Trichas, M., Urrutia, T., van Kampen, E., Verma, A., and Xu, C. K. (2012). The Spitzer Extragalactic Representative Volume Survey (SERVS): Survey Definition and Goals. *PASP*, **124**, 714–736.
- McLure, R. J. and Dunlop, J. S. (2002). On the black hole-bulge mass relation in active and inactive galaxies. *MNRAS*, **331**, 795–804.
- Miller, C. J., Nichol, R. C., Gómez, P. L., Hopkins, A. M., and Bernardi, M. (2003). The Environment of Active Galactic Nuclei in the Sloan Digital Sky Survey. *ApJ*, **597**, 142–156.
- Moran, E. C., Halpern, J. P., and Helfand, D. J. (1996). Classification of IRAS-selected X-Ray Galaxies in the ROSAT All-Sky Survey. *ApJS*, **106**, 341.
- Mushotzky, R. (2004). How are AGN Found? In A. J. Barger, editor, *Supermassive Black Holes in the Distant Universe*, volume 308 of *Astrophysics and Space Science Library*, page 53.
- Muzzin, A., Wilson, G., Demarco, R., Lidman, C., Nantais, J., Hoekstra, H., Yee, H. K. C., and Rettura, A. (2013). Discovery of a Rich Cluster at $z = 1.63$ Using the Rest-frame $1.6 \mu\text{m}$ "Stellar Bump Sequence" Method. *ApJ*, **767**, 39.
- Netzer, H. (2015). Revisiting the Unified Model of Active Galactic Nuclei. *ArXiv e-prints*.
- Norris, R. P. (2011). Evolutionary Map of the Universe: Tracing Clusters to High Red-shift. *Journal of Astrophysics and Astronomy*, **32**, 599–607.
- Oh, S. P. (2010). AGN Feedback Heating in Clusters. In *Galaxy Clusters: Observations, Physics and Cosmology*, page 42.

- Oke, J. B. and Gunn, J. E. (1983). Secondary standard stars for absolute spectrophotometry. *ApJ*, **266**, 713–717.
- Oliver, S. J., Bock, J., Altieri, B., Amblard, A., Arumugam, V., Aussel, H., Babbedge, T., Beelen, A., Béthermin, M., Blain, A., Boselli, A., Bridge, C., Brisbin, D., Buat, V., Burgarella, D., Castro-Rodríguez, N., Cava, A., Chanial, P., Cirasuolo, M., Clements, D. L., Conley, A., Conversi, L., Cooray, A., Dowell, C. D., Dubois, E. N., Dwek, E., Dye, S., Eales, S., Elbaz, D., Farrah, D., Feltre, A., Ferrero, P., Fiolet, N., Fox, M., Franceschini, A., Gear, W., Giovannoli, E., Glenn, J., Gong, Y., González Solares, E. A., Griffin, M., Halpern, M., Harwit, M., Hatziminaoglou, E., Heinis, S., Hurley, P., Hwang, H. S., Hyde, A., Ibar, E., Ilbert, O., Isaak, K., Ivison, R. J., Lagache, G., Le Floc’h, E., Levenson, L., Faro, B. L., Lu, N., Madden, S., Maffei, B., Magdis, G., Mainetti, G., Marchetti, L., Marsden, G., Marshall, J., Mortier, A. M. J., Nguyen, H. T., O’Halloran, B., Omont, A., Page, M. J., Panuzzo, P., Papageorgiou, A., Patel, H., Pearson, C. P., Pérez-Fournon, I., Pohlen, M., Rawlings, J. I., Raymond, G., Rigopoulou, D., Riguccini, L., Rizzo, D., Rodighiero, G., Roseboom, I. G., Rowan-Robinson, M., Sánchez Portal, M., Schulz, B., Scott, D., Seymour, N., Shupe, D. L., Smith, A. J., Stevens, J. A., Symeonidis, M., Trichas, M., Tugwell, K. E., Vaccari, M., Valtchanov, I., Vieira, J. D., Viero, M., Vigroux, L., Wang, L., Ward, R., Wardlow, J., Wright, G., Xu, C. K., and Zemcov, M. (2012). The Herschel Multi-tiered Extragalactic Survey: HerMES. *MNRAS*, **424**, 1614–1635.
- Padmanabhan, N., Xu, X., Eisenstein, D. J., Scalzo, R., Cuesta, A. J., Mehta, K. T., and Kazin, E. (2012). A 2 per cent distance to $z = 0.35$ by reconstructing baryon acoustic oscillations - I. Methods and application to the Sloan Digital Sky Survey. *MNRAS*, **427**, 2132–2145.
- Padovani, P., Mainieri, V., Tozzi, P., Kellermann, K. I., Fomalont, E. B., Miller, N., Rosati, P., and Shaver, P. (2009). The Very Large Array Survey of the Chandra Deep Field South. IV. Source Population. *ApJ*, **694**, 235–246.
- Park, S. Q., Barmby, P., Willner, S. P., Ashby, M. L. N., Fazio, G. G., Georgakakis, A., Ivison, R. J., Konidaris, N. P., Miyazaki, S., Nandra, K., and Rosario, D. J. (2010). AEGIS: A Multiwavelength Study of Spitzer Power-law Galaxies. *ApJ*, **717**, 1181–1201.
- Patel, H., Clements, D. L., Vaccari, M., Mortlock, D. J., Rowan-Robinson, M., Pérez-Fournon, I., and Afonso-Luis, A. (2013). Evolution of the far-infrared luminosity functions in the Spitzer Wide-area Infrared Extragalactic Legacy Survey. *MNRAS*, **428**, 291–306.

- Perez-Fournon, I., Afonso-Luis, A., Babbedge, T., Clements, D., Farrah, D., Gonzalez-Solares, E. A., Gruppioni, C., Hatziminaoglou, E., Hernan-Caballero, A., La Franca, F., Lari, C., Montenegro Montes, F. M., Oliver, S., Pozzi, F., Rigopoulou, D., Rowan-Robinson, M., Serjeant, S., Vaccari, M., Valtchanov, I., and Vila-Vilaro, B. (2004). IRS observations of ultraluminous ELAIS galaxies. Spitzer Proposal.
- Peterson, B. (2006). Host Galaxies of Reverberation Mapped AGNs. HST Proposal.
- Prandoni, I., Gregorini, L., Parma, P., de Ruiter, H. R., Vettolani, G., Wieringa, M. H., and Ekers, R. D. (2001). The ATESP radio survey. III. Source counts. *A&A*, **365**, 392–399.
- Rawlings, J. I., Page, M. J., Symeonidis, M., Bock, J., Cooray, A., Farrah, D., Guo, K., Hatziminaoglou, E., Ibar, E., Oliver, S. J., Roseboom, I. G., Scott, D., Seymour, N., Vaccari, M., and Wardlow, J. L. (2015). HerMES: disentangling active galactic nuclei and star formation in the radio source population. *MNRAS*, **452**, 4111–4127.
- Rawlings, S. and Jarvis, M. J. (2004). Evidence that powerful radio jets have a profound influence on the evolution of galaxies. *MNRAS*, **355**, L9–L12.
- Richards, G., Anderson, S., Bauer, F., Deo, R., Fan, X., Gallagher, S., Myers, A., Strauss, M., and Zakamska, N. (2009). Leveraging Spitzer’s Legacy: Quasars and Feedback at High Redshift. Spitzer Proposal.
- Richstone, D. (1998). Supermassive black holes then and now. In W. M. Folkner, editor, *Laser Interferometer Space Antenna, Second International LISA Symposium on the Detection and Observation of Gravitational Waves in Space*, volume 456 of *American Institute of Physics Conference Series*, pages 41–44.
- Rieke, G. H., Young, E. T., Engelbracht, C. W., Kelly, D. M., Low, F. J., Haller, E. E., Beeman, J. W., Gordon, K. D., Stansberry, J. A., Misselt, K. A., Cadien, J., Morrison, J. E., Rivlis, G., Latter, W. B., Noriega-Crespo, A., Padgett, D. L., Stapelfeldt, K. R., Hines, D. C., Egami, E., Muzerolle, J., Alonso-Herrero, A., Blaylock, M., Dole, H., Hinz, J. L., Le Floch, E., Papovich, C., Pérez-González, P. G., Smith, P. S., Su, K. Y. L., Bennett, L., Frayer, D. T., Henderson, D., Lu, N., Masci, F., Pesenson, M., Rebull, L., Rho, J., Keene, J., Stolovy, S., Wachter, S., Wheaton, W., Werner, M. W., and Richards, P. L. (2004). The Multiband Imaging Photometer for Spitzer (MIPS). *ApJS*, **154**, 25–29.
- Rola, C. S., Terlevich, E., and Terlevich, R. J. (1997). New diagnostic methods for emission-line galaxies in deep surveys. *MNRAS*, **289**, 419–427.
- Rowan-Robinson, M. (2003). Quantifying dust and the ultraviolet radiation density in the local Universe. *MNRAS*, **344**, 13–21.

- Rowan-Robinson, M., Lari, C., Perez-Fournon, I., Gonzalez-Solares, E. A., La Franca, F., Vaccari, M., Oliver, S., Gruppioni, C., Ciliegi, P., Heraudeau, P., Serjeant, S., Efstathiou, A., Babbedge, T., Matute, I., Pozzi, F., Franceschini, A., Vaisanen, P., Afonso-Luis, A., Alexander, D. M., Almaini, O., Baker, A. C., Basilakos, S., Barden, M., del Burgo, C., Bellas-Velidis, I., Cabrera-Guerra, F., Carballo, R., Cesarsky, C. J., Clements, D. L., Crockett, H., Danese, L., Dapergolas, A., Drolias, B., Eaton, N., Egami, E., Elbaz, D., Fadda, D., Fox, M., Genzel, R., Goldschmidt, P., Gonzalez-Serrano, J. I., Graham, M., Granato, G. L., Hatziminaoglou, E., Herbstmeier, U., Joshi, M., Kontizas, E., Kontizas, M., Kotilainen, J. K., Kunze, D., Lawrence, A., Lemke, D., Linden-Vornle, M. J. D., Mann, R. G., Marquez, I., Masegosa, J., McMahon, R. G., Miley, G., Missoulis, V., Mobasher, B., Morel, T., Norgaard-Nielsen, H., Omont, A., Papadopoulos, P., Puget, J.-L., Rigopoulou, D., Rocca-Volmerange, B., Sedgwick, N., Silva, L., Sumner, T., Surace, C., Vila-Vilaro, B., van Der Werf, P., Verma, A., Vigroux, L., Villar-Martin, M., Willott, C. J., Carraminana, A., and Mujica, R. (2004). VizieR Online Data Catalog: ELAIS: final band-merged catalogue (Rowan-Robinson+, 2004). *VizieR Online Data Catalog*, **735**, 11290.
- Rowan-Robinson, M., Babbedge, T., Oliver, S., Trichas, M., Berta, S., Lonsdale, C., Smith, G., Shupe, D., Surace, J., Arnouts, S., Ilbert, O., Le Fèvre, O., Afonso-Luis, A., Perez-Fournon, I., Hatziminaoglou, E., Polletta, M., Farrah, D., and Vaccari, M. (2008). Photometric redshifts in the SWIRE Survey. *MNRAS*, **386**, 697–714.
- Rowan-Robinson, M., Gonzalez-Solares, E., Vaccari, M., and Marchetti, L. (2013). Revised SWIRE photometric redshifts (Rowan-Robinson+, 2013). *VizieR Online Data Catalog*, **2326**, 0.
- Sajina, A., Lacy, M., and Scott, D. (2005). Simulating the Spitzer Mid-Infrared Color-Color Diagrams. *ApJ*, **621**, 256–268.
- Sajina, A., Yan, L., Lacy, M., and Huynh, M. (2007). Discovery of Radio Jets in $z \sim 2$ Ultraluminous Infrared Galaxies with Deep $9.7 \mu\text{m}$ Silicate Absorption. *ApJ*, **667**, L17–L20.
- Sajina, A., Yan, L., Lutz, D., Steffen, A., Helou, G., Huynh, M., Frayer, D., Choi, P., Tacconi, L., and Dasyra, K. (2008). Spitzer Mid-Infrared Spectroscopy of Infrared Luminous Galaxies at $z \sim 2$. III. Far-IR to Radio Properties and Optical Spectral Diagnostics. *ApJ*, **683**, 659–682.
- Sargent, M. T., Schinnerer, E., Murphy, E., Carilli, C. L., Helou, G., Aussel, H., Le Floc'h, E., Frayer, D. T., Ilbert, O., Oesch, P., Salvato, M., Smolčić, V., Kartaltepe, J., and Sanders, D. B. (2010). No Evolution in the IR-Radio Relation for IR-luminous Galaxies at $z < 2$ in the COSMOS Field. *ApJ*, **714**, L190–L195.

- Schawinski, K., Urry, C. M., Virani, S., Coppi, P., Bamford, S. P., Treister, E., Lintott, C. J., Sarzi, M., Keel, W. C., Kaviraj, S., Cardamone, C. N., Masters, K. L., Ross, N. P., and Ross (2010). Black Hole Growth and Host Galaxy Morphology. In B. M. Peterson, R. S. Somerville, and T. Storchi-Bergmann, editors, *IAU Symposium*, volume 267 of *IAU Symposium*, pages 438–441.
- Schawinski, K., Urry, C. M., Simmons, B. D., Fortson, L., Kaviraj, S., Keel, W. C., Lintott, C. J., Masters, K. L., Nichol, R. C., Sarzi, M., Skibba, R., Treister, E., Willett, K. W., Wong, O. I., and Yi, S. K. (2014). The green valley is a red herring: Galaxy Zoo reveals two evolutionary pathways towards quenching of star formation in early- and late-type galaxies. *MNRAS*, **440**, 889–907.
- Serjeant, S., Carramiñana, A., González-Solares, E., Héraudeau, P., Mújica, R., Perez-Fournon, I., Sedgwick, N., Rowan-Robinson, M., Franceschini, A., Babbedge, T., del Burgo, C., Ciliegi, P., Efstathiou, A., La Franca, F., Gruppioni, C., Hughes, D., Lari, C., Oliver, S., Pozzi, F., Stickel, M., and Vaccari, M. (2004). The European Large Area ISO Survey - IX. The 90- μm luminosity function from the Final Analysis sample. *MNRAS*, **355**, 813–818.
- Seymour, N., Dwelly, T., Moss, D., Mhardy, I., Zoghbi, A., Rieke, G., Page, M., and Hopkins, A. (2008a). The Contribution of Radio Selected Star Forming Galaxies to the IR Energy Density Budget. In T. Kodama, T. Yamada, and K. Aoki, editors, *Panoramic Views of Galaxy Formation and Evolution*, volume 399 of *Astronomical Society of the Pacific Conference Series*, page 197.
- Seymour, N., Dwelly, T., Moss, D., McHardy, I., Zoghbi, A., Rieke, G., Page, M., Hopkins, A., and Loaring, N. (2008b). The star formation history of the Universe as revealed by deep radio observations. *MNRAS*, **386**, 1695–1708.
- Smith, D. J. B., Jarvis, M. J., Hardcastle, M. J., Vaccari, M., Bourne, N., Dunne, L., Ibar, E., Maddox, N., Prescott, M., Vlahakis, C., Eales, S., Maddox, S. J., Smith, M. W. L., Valiante, E., and de Zotti, G. (2014). The temperature dependence of the far-infrared-radio correlation in the Herschel-ATLAS. *MNRAS*, **445**, 2232–2243.
- Smolčić, V. (2009). The Radio AGN Population Dichotomy: Green Valley Seyferts Versus Red Sequence Low-Excitation Active Galactic Nuclei. *ApJ*, **699**, L43–L47.
- Smolčić, V., Schinnerer, E., Scodreggio, M., Franzetti, P., Aussel, H., Bondi, M., Brusa, M., Carilli, C. L., Capak, P., Charlot, S., Ciliegi, P., Ilbert, O., Ivezić, Ž., Jahnke, K., McCracken, H. J., Obrić, M., Salvato, M., Sanders, D. B., Scoville, N., Trump, J. R., Tremonti, C., Tasca, L., Walcher, C. J., and Zamorani, G. (2008). A New Method to Separate Star-forming from AGN Galaxies at Intermediate Redshift: The Submillijansky Radio Population in the VLA-COSMOS Survey. *ApJS*, **177**, 14–38.

- Spinoglio, L. and Malkan, M. A. (1989). A 12 μM Flux Limited Sample of Galaxies: Preliminary Results on the IR Luminosity Function. In D. E. Osterbrock and J. S. Miller, editors, *Active Galactic Nuclei*, volume 134 of *IAU Symposium*, page 55.
- Springel, V., Di Matteo, T., and Hernquist, L. (2005). Modelling feedback from stars and black holes in galaxy mergers. *MNRAS*, **361**, 776–794.
- Stern, D., Eisenhardt, P., Gorjian, V., Kochanek, C. S., Caldwell, N., Eisenstein, D., Brodwin, M., Brown, M. J. I., Cool, R., Dey, A., Green, P., Jannuzi, B. T., Murray, S. S., Pahre, M. A., and Willner, S. P. (2005). Mid-Infrared Selection of Active Galaxies. *ApJ*, **631**, 163–168.
- Strateva, I., Ivezić, Ž., Knapp, G. R., Narayanan, V. K., Strauss, M. A., Gunn, J. E., Lupton, R. H., Schlegel, D., Bahcall, N. A., Brinkmann, J., Brunner, R. J., Budavári, T., Csabai, I., Castander, F. J., Doi, M., Fukugita, M., Györy, Z., Hamabe, M., Hennessy, G., Ichikawa, T., Kunszt, P. Z., Lamb, D. Q., McKay, T. A., Okamura, S., Racusin, J., Sekiguchi, M., Schneider, D. P., Shimasaku, K., and York, D. (2001). Color Separation of Galaxy Types in the Sloan Digital Sky Survey Imaging Data. *AJ*, **122**, 1861–1874.
- Surace, J. A., Shupe, D. L., Fang, F., Evans, T., Alexov, A., Frayer, D., Lonsdale, C. J., and SWIRE Team (2005). Data Processing and Validation of the SWIRE Survey. In *American Astronomical Society Meeting Abstracts*, volume 37 of *Bulletin of the American Astronomical Society*, page 1246.
- Szokoly, G. P., Bergeron, J., Hasinger, G., Lehmann, I., Kewley, L., Mainieri, V., Nonino, M., Rosati, P., Giacconi, R., Gilli, R., Gilmozzi, R., Norman, C., Romaniello, M., Schreier, E., Tozzi, P., Wang, J. X., Zheng, W., and Zirm, A. (2004). The Chandra Deep Field-South: Optical Spectroscopy. I. *ApJS*, **155**, 271–349.
- Taylor, A. R., Bhatnagar, S., Condon, J., Green, D. A., Stil, J. M., Jagannathan, P., Kantharia, N., Kothes, R., Perley, R., Wall, J., and Willis, T. (2014). The Deep Full-Stokes Radio Sky. *ArXiv e-prints*.
- Thomson, A. P., Ivison, R. J., Simpson, J. M., Swinbank, A. M., Smail, I., Arumugam, V., Alexander, D. M., Beelen, A., Brandt, W. N., Chandra, I., Dannerbauer, H., Greve, T. R., Hodge, J. A., Ibar, E., Karim, A., Murphy, E. J., Schinnerer, E., Sirothia, S., Walter, F., Wardlow, J. L., and van der Werf, P. (2014). An ALMA survey of submillimetre galaxies in the Extended Chandra Deep Field South: radio properties and the far-infrared/radio correlation. *MNRAS*, **442**, 577–588.
- Tremaine, S., Gebhardt, K., Bender, R., Bower, G., Dressler, A., Faber, S. M., Filippenko, A. V., Green, R., Grillmair, C., Ho, L. C., Kormendy, J., Lauer, T. R.,

- Magorrian, J., Pinkney, J., and Richstone, D. (2002). The Slope of the Black Hole Mass versus Velocity Dispersion Correlation. *ApJ*, **574**, 740–753.
- Tresse, L., Rola, C., Hammer, F., Stasińska, G., Le Fevre, O., Lilly, S. J., and Crampton, D. (1996). The Canada-France Redshift Survey - XII. Nature of emission-line field galaxy population up to $z=0.3$. *MNRAS*, **281**, 847–870.
- Trichas, M., Green, P. J., Silverman, J. D., Aldcroft, T., Barkhouse, W., Cameron, R. A., Constantin, A., Ellison, S. L., Foltz, C., Haggard, D., Jannuzi, B. T., Kim, D.-W., Marshall, H. L., Mossman, A., Pérez, L. M., Romero-Colmenero, E., Ruiz, A., Smith, M. G., Smith, P. S., Torres, G., Wik, D. R., Wilkes, B. J., and Wolfgang, A. (2012). The Chandra Multi-wavelength Project: Optical Spectroscopy and the Broadband Spectral Energy Distributions of X-Ray-selected AGNs. *ApJS*, **200**, 17.
- Trouille, L., Barger, A. J., and Tremonti, C. (2011). The OPTX Project V: Identifying Distant AGNs. *ArXiv e-prints*.
- Urry, C. M. and Padovani, P. (1995). Unified Schemes for Radio-Loud Active Galactic Nuclei. *PASP*, **107**, 803.
- Veilleux, S. and Osterbrock, D. E. (1987). Spectral classification of emission-line galaxies. In C. J. Lonsdale Persson, editor, *NASA Conference Publication*, volume 2466 of *NASA Conference Publication*, pages 737–740.
- Voelk, H. J. (1989). The correlation between radio and far-infrared emission for disk galaxies - A calorimeter theory. *A&A*, **218**, 67–70.
- Werner, M. W., Roellig, T. L., Low, F. J., Rieke, G. H., Rieke, M., Hoffmann, W. F., Young, E., Houck, J. R., Brandl, B., Fazio, G. G., Hora, J. L., Gehrz, R. D., Helou, G., Soifer, B. T., Stauffer, J., Keene, J., Eisenhardt, P., Gallagher, D., Gautier, T. N., Irace, W., Lawrence, C. R., Simmons, L., Van Cleve, J. E., Jura, M., Wright, E. L., and Cruikshank, D. P. (2004). The Spitzer Space Telescope Mission. *ApJS*, **154**, 1–9.
- White, S. D. M. and Frenk, C. S. (1991). Galaxy formation through hierarchical clustering. *ApJ*, **379**, 52–79.
- Windhorst, R. A. (1984). *Faint radio galaxy populations*. Ph.D. thesis, Ph. D. thesis, University of Leiden (1984).
- York, D. G., Adelman, J., Anderson, Jr., J. E., Anderson, S. F., Annis, J., Bahcall, N. A., Bakken, J. A., Barkhouser, R., Bastian, S., Berman, E., Boroski, W. N., Bracker, S., Briegel, C., Briggs, J. W., Brinkmann, J., Brunner, R., Burles, S., Carey, L., Carr, M. A., Castander, F. J., Chen, B., Colestock, P. L., Connolly, A. J., Crocker, J. H., Csabai, I., Czarapata, P. C., Davis, J. E., Doi, M., Dombeck, T., Eisenstein,

- D., Ellman, N., Elms, B. R., Evans, M. L., Fan, X., Federwitz, G. R., Fiscelli, L., Friedman, S., Frieman, J. A., Fukugita, M., Gillespie, B., Gunn, J. E., Gurbani, V. K., de Haas, E., Haldeman, M., Harris, F. H., Hayes, J., Heckman, T. M., Hennessy, G. S., Hindsley, R. B., Holm, S., Holmgren, D. J., Huang, C.-h., Hull, C., Husby, D., Ichikawa, S.-I., Ichikawa, T., Ivezić, Ž., Kent, S., Kim, R. S. J., Kinney, E., Klaene, M., Kleinman, A. N., Kleinman, S., Knapp, G. R., Korienek, J., Kron, R. G., Kunszt, P. Z., Lamb, D. Q., Lee, B., Leger, R. F., Limmongkol, S., Lindenmeyer, C., Long, D. C., Loomis, C., Loveday, J., Lucinio, R., Lupton, R. H., MacKinnon, B., Mannery, E. J., Mantsch, P. M., Margon, B., McGehee, P., McKay, T. A., Meiksin, A., Merelli, A., Monet, D. G., Munn, J. A., Narayanan, V. K., Nash, T., Neilsen, E., Neswold, R., Newberg, H. J., Nichol, R. C., Nicinski, T., Nonino, M., Okada, N., Okamura, S., Ostriker, J. P., Owen, R., Pauls, A. G., Peoples, J., Peterson, R. L., Petravick, D., Pier, J. R., Pope, A., Pordes, R., Prosapio, A., Rechenmacher, R., Quinn, T. R., Richards, G. T., Richmond, M. W., Rivetta, C. H., Rockosi, C. M., Ruthmansdorfer, K., Sandford, D., Schlegel, D. J., Schneider, D. P., Sekiguchi, M., Sergey, G., Shimasaku, K., Siegmund, W. A., Smee, S., Smith, J. A., Snedden, S., Stone, R., Stoughton, C., Strauss, M. A., Stubbs, C., SubbaRao, M., Szalay, A. S., Szapudi, I., Szokoly, G. P., Thakar, A. R., Tremonti, C., Tucker, D. L., Uomoto, A., Vanden Berk, D., Vogeley, M. S., Waddell, P., Wang, S.-i., Watanabe, M., Weinberg, D. H., Yanny, B., Yasuda, N., and SDSS Collaboration (2000). The Sloan Digital Sky Survey: Technical Summary. *AJ*, **120**, 1579–1587.
- Yun, M. S., Reddy, N. A., and Condon, J. J. (2001). Radio Properties of Infrared-selected Galaxies in the IRAS 2 Jy Sample. *ApJ*, **554**, 803–822.
- Yun, M. S., Aretxaga, I., Ashby, M. L. N., Austermann, J., Fazio, G. G., Giavalisco, M., Huang, J.-S., Hughes, D. H., Kim, S., Lowenthal, J. D., Perera, T., Scott, K., Wilson, G., and Younger, J. D. (2008). Spitzer IRAC infrared colours of submillimetre-bright galaxies. *MNRAS*, **389**, 333–340.